Title
Emergent Phenomena at Complex Oxide Interfaces

Author
Yu, Pu

Publication Date
2011

Peer reviewed|Thesis/dissertation

Emergent Phenomena at Complex Oxide Interfaces

by

Pu Yu

A dissertation submitted in partial satisfaction of the

requirements for the degree of

Doctor of Philosophy

in

Physics

in the

Graduate Division

of the

University of California, Berkeley

Committee in charge:

Professor Ramamoorthy Ramesh, Chair

Professor Feng Wang

Professor Junqiao Wu

Professor Oscar D. Dubon

Spring 2011

Emergent Phenomena at Complex Oxide Interfaces

Abstract

Emergent Phenomena at Complex Oxide Interfaces

by

Pu Yu

Doctor of Philosophy in Physics

University of California, Berkeley

Professor Ramamoorthy Ramesh, Chair

Novel phenomena and functionalities at epitaxial complex oxide heterostructures have been attracting huge scientific attention because of the intriguing fundamental physics as well as potential for technological applications that they embody. Essentially, charge and spin reconstruction at the interface can lead to exotic properties, which are completely different from those inherent to the individual materials, for example, a conductive interface between two insulating materials and interface ferromagnetism in the proximity of an antiferromagnet. The interplay between charge and spin degrees of freedom can be particularly intriguing, leading to a fascinating realm, called multiferroic. In this dissertation, a systematic study is performed on the electronic (charge) and magnetic (spin) interaction/reconstruction across the interface of an all-oxide model heterostructure system consisting of the ferromagnet (FM) $La_{0.7}Sr_{0.3}MnO_3$ (LSMO) and the multiferroic (ferroelectric and antiferromagnetic) $BiFeO_3$ (BFO). The study demonstrates two pathways of using these exotic interfacial properties to control bulk properties, both the ferroelectricity in BFO and ferromagnetism in LSMO.

The journey starts with the growth of high-quality BFO/LSMO heterostructures with unit-cell precision control using reflection high-energy electron diffraction combined with pulsed-laser deposition, providing an important platform for the investigation of electronic and magnetic coupling phenomena across the interface. First, we have observed a novel consequence of the interface electronic interaction due to the so-called "polar discontinuity", namely, a built-in electrostatic potential accumulates across the heterointerface, and provides deterministic control of ferroelectric polarization states in thin films. This observation suggests a strong, delocalized effect with important implications for future electronics based on such materials. Secondly, we have revealed a strong magnetic coupling at this interface, manifested in the form of an enhanced coercive field as well as a significant exchange-bias coupling. Based on our x-ray magnetic circular dichroism studies, the origin of the exchange-bias coupling is attributed to a novel ferromagnetic state formed in the antiferromagnetic BFO sublattice at the interface with LSMO. Thirdly, using a field effect geometry, we have proposed a pathway to use an electric field to control the magnetism in

LSMO in which the ground state of the interfacial ferromagnetic state is strongly correlated with the ferroelectric polarization. Magnetotransport measurements clearly demonstrate a reversible switch/control between two distinct exchange-bias states by isothermally switching the ferroelectric polarization of BFO. This is an important step towards controlling magnetization with the electric field, which may enable a new class of electrically controllable spintronic devices and provide a new basis for producing electrically controllable spin-polarized currents. Finally, combining experimental results with first-principle and phenomenological model calculations, a microscopic model has been proposed to understand the underlying physics of the magnetoelectric coupling, providing further insights on achieving the electric-field control of magnetism.

In summary, our studies on the interfacial electronic and magnetic properties at BFO/LSMO heterointerfaces have revealed a strong interplay between the charge, spin, orbital and lattice degrees of freedom at the interface, which will have important implications for a new pathway to use the interface properties to control bulk functionalities (ferroelectric polarization and ferromagnetic magnetization in this study). Such couplings at the interface may be extended to other oxides and will bring into play remarkable physical concepts to this developing field of complex oxide heterointerfaces.

To my parents,my wife and my son

for their loves.

Contents

List of Figures

List of Tables

Acknowledgments

I want to thank a lot of people for their support on the journey toward my PhD.

First of all, I would like to thank my advisor, Professor Ramamoorthy Ramesh for providing me the opportunity to work on such interesting and exciting topics. I would like to thank him for giving me the freedom to explore new projects, while at the same time providing suggestions and helps along my way whenever needed.

I would like to thank Professor Feng Wang, Professor Oscar Dubon, Professor Ashvin Vishwanath and Professor Junqiao Wu for being on my qualifying exam and dissertation committee and providing important suggestions and comments on my research. I would also like to thank Professor Sayeef Salahuddin for very useful discussions on various interesting research topics.

I have been very lucky to work with a large group of talented and friendly colleagues in the CONCEPT lab. I would like to thank especially the following previous and present members of the group for their help and friendship: Dr. Ying-Hao Chu for mentoring me in my early years and daily discussions about oxide electronics which still continues till today; Dr. Lane Martin for the great impact he has left to the lab and for telling us the importance of focus; Qing He for sharing the same memories of PhD studies and collaborations on numerous projects; Dr. Chan-Ho Yang and Dr. Martin Gajek for teaching me strong correlation physics; Dr. Micky Barry Holcomb for help with beamline measurements; Dr. Mark Huijben for teaching me about Laser MBE growth; Dr. Seung-Yeul Yang for sharing with me his secrets on sample growth; Dr. Jinxing Zhang, Dr. Nina Balke, Dr. Padraic Shafer, Dr. Jan Seidel and Dr. Maria de la Paz Cruz for help with PFM measurements; Dr. Guneeta Singh Bhalla for discussion about interface electronics; Dr. Steven Crane, John Heron, Jayakanth Ravichandran, Dr. Wolter Siemons, Dr. Morgan Trassin, Dr. Balasubramaniam Kavaipatti for taking care of the lab at various stages and providing us a great experimental environment; Dr. Susanne Kehr for teaching me about superlense; Robert Zeches and Dr. Matthew Scullin for assisting with SEM measurements; Asif Islam Khan for discussion and collaboration on ferroelectrics; Michelle Lee, Tianliang Qu and Dr. Lili Wang for assisting with both measurement and growth; Pim Rossen, Di Yi and James Clarkson for bringing fresh blood and energy into the lab.

I would like to acknowledge the efforts of the following individuals and groups for the close and productive collaborations for both works present in this dissertation and beyond (in alphabetical order): Dr. Albina Borisevich, Dr. Hye Jung Chang and Professor Stephen Pennycook at the STEM group of Oak Ridge National Laboratory for collaboration of TEM studies; Professor Seigei Kalinin at CNMS of ORNL for close collaborations, discussions and suggestions; Hsin-Hua Lee and Professor Yi-Chun Chen at National Cheng Kung University for macroscopic switching on ferroelectric thin films; Dr. Jun-Sik Lee, Dr. Arena Dario and Professor Chi-Chang Kao at Brookhaven National Laboratory for help with x-ray circular dichroism measure-

ment; Dr. Weidong Luo and Professor Sokrates Pantelides at Vanderbilt University and ORNL for valuable discussions and providing endless modelings and physics insights; Dr. Petro Maksymovych at CNMS of ORNL for close collaborations with ferroelectrics; Dr. Satoshi Okamoto at ORNL for valuable discussion about strong correlated physics as well as providing theoretical support for our work; Dr. Marta Rossell, Dr. Quentin Ramasse and Dr. Erni Rolf at NCEM group of LBNL for help with STEM measurements; Stephen Wu, Dr. Shane Cybart and Professor Robert Dynes at University of California at Berkeley and San Diego for magnetotransport measurements.

Most especially to my family. I am deeply grateful to my parents for their understanding and support from when I was still a small kid till today. Thanks to my little Brian who has brought to me tons of happiness and laughs during the last few years. Finally, I am unable to fully express my gratitude to my wife Shuyun for her love, trust, support, encouragement and understanding over the long way.

Chapter 1

Introduction

This chapter provides a brief introduction to the background and key concepts of two fascinating research realms closely related with this dissertation: emergent phenomena at complex oxide interfaces and multiferroics (or magnetoelectric coupling). First, the physics background of transition metal oxide materials is provided at the beginning to serve as prerequisite knowledge for subsequent discussions. Following is a quick survey of the charge and spin reconstruction at heterointerfaces. Then, different strategies of the electric-field control of magnetism (main focus of this dissertation), are discussed in terms of the coupling/interplay of different degrees of freedom across the interface. Finally, a brief summary of the organization of this dissertation is given at the end.

1.1 Emergent phenomena at complex oxide interfaces

The Nobel Prize laureate Herbert Kroemer stated at the beginning of his Nobel lecture, "*Often, it may be said that the interface is the device*". [1] Controlling the interface of materials with atomic precision to obtain novel properties and functionalities has been at the forefront of both modern condensed matter physics and materials science, since they can give rise to a wide range of remarkable novel properties. It has long been known that in complex oxide materials, charge, spin, orbital and lattice degrees of freedom co-exist and couplings between these degrees of freedom can generate a rich spectrum of physical responses, including high temperature superconducting [2], metal-insulator transition [3], colossal magnetoresistance [4, 5], etc. Over the past decade, research on the interactions between such degrees of freedom across complex oxide interfaces has revealed fascinating emergent phenomena and novel states of matter in the complex oxide heterostructure [6–10], suggesting that the complex oxide might be a promising substitution for the traditional silicon in electronics applications. [11–14]

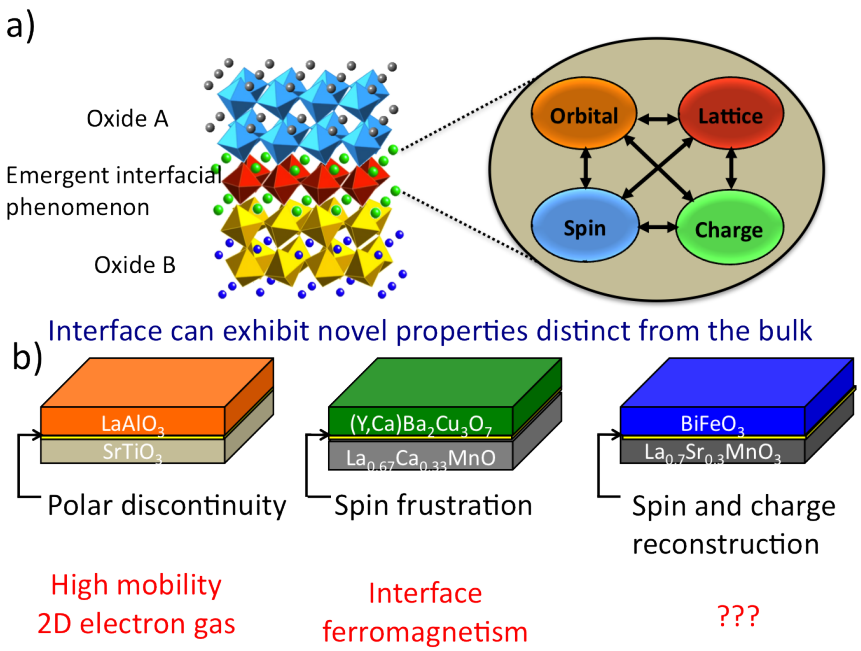

Figure 1.1: The interplay between heterointerfacial degrees of freedom. (a) A schematic showing the interplay between the different degrees of freedom at play (charge, spin, orbital and lattice) at heteroepitaxially grown interfaces between different oxide materials. (b) Some canonical examples of interfacial reconstruction and the new emergent interfacial phenomenon that occur in these systems.

The ability to create atomically perfect, lattice matched heterostructures of complex perovskite oxides using state-of-the-art deposition tools has recently expanded the imagination of solid state scientists worldwide. From the observation of a high mobility two dimensional electron gas at the interface between two insulators [6,7] to the observation of novel magnetism across interfaces [15, 16], such artificially engineered interfaces are emerging as a new horizon in materials science these days. Figure 1.1 shows a schematic of the heterointerface between two complex oxide materials. The ability to control and manipulate the coupling and interplay of charge, spin and orbital degrees of freedom through heterointerfaces, has enabled researchers to design and engineer novel functionalities of materials. In the past decade, a significant amount of research is focused on the electronic reconstruction at the interface between $LaAlO_3$ and $SrTiO_3$, in which an interface conducting state (high mobility two dimensional electron gas) is formed although both of the constitute compounds are insulating. [7] Similar, the spin reconstruction across interface will also lead to interesting interfacial properties. For example, the work of Chakhalian *et al.* demonstrated the emergence of a novel magnetic state in a $(Y,Ca)Ba_2Cu_3O_7$ (high temperature superconductor) layer at the interface with the doped manganite $La_{0.67}Ca_{0.33}MnO_3$. [16] Electric-field control of such an interface ferromagnetic state would be a significant step towards

magnetoelectric devices [17,18], which is one of the main focuses of the current dissertation. The model system, which I have chosen, is the heterostructure consisting of the ferromagnet $La_0.7Sr_0.3MnO_3$ and the multiferroic (ferroelectric and antiferromagnetic) $BiFeO_3$, in which, the interplay/coupling between charge and spin degrees of freedom leads to the magnetoelectric coupling. Thus, to better understand the magnetoelectric coupling (interplay between charge and spin degrees of freedom) through the heterointerface, one must first investigate the interfacial electronic and magnetic reconstructions respectively.

1.1.1 Complex perovskite oxide

Perovskite oxides and structurally related materials have attracted intense research interest during past decades in both materials science research and condensed matter physics. They comprise of a broad spectrum of interesting functionalities, such as high temperature superconducting, colossal magnetoresistance, (anti-) ferromagnetic, (anti-) ferroelectric, piezoelectric and more recently multiferroic properties, just to name a few. The wide range of material properties and rich physics involved have led to extensive studies to understand the fundamental nature of existing systems, so as to better control/design novel materials for applications. The rest of this section will give a quick introduction to the basic concepts of the perovskite complex oxide in terms of charge, spin, orbital and lattice degrees of freedom.

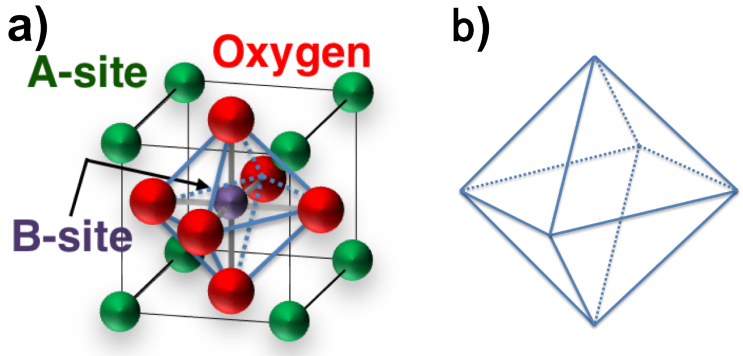

Figure 1.2: Schematic of a perovskite structure ABO_3. (a) Unit cell of cubic ABO_3 perovskite structure. (b) Octahedral structure formed with six oxygen atoms at the corner.

Figure 1.2a shows a sketch of the cubic perovskite unit cell with the chemical formula of ABO_3, where A cation is an (alkaline) rare earth element, located at the corner of the cubic structure, B cation is a transition metal, rare earth, or group III metal element located at the center of the cubic structure, and O presents a oxygen anion positioned at the face center of the cubic structure. From the geography point of view, the transition metal atom is surrounded by six oxygen atoms, which forms

an octahedral structure as shown in Fig. 1.2b. We note that both A and B cations could be chosen from a broad range of elements in the periodic table with variable valence states and ionic radii. The rule of thumb is that the totally charge in the ABO_3 structure should remain neutral. Thus, the A and B cations can take on the values of $A^{4+}B^{2+}$, $A^{3+}B^{3+}$, $A^{2+}B^{4+}$ or $A^{1+}B^{5+}$. We note that the slightly charge imbalance can also be compensated with either valence change of cations or oxygen vacancies.

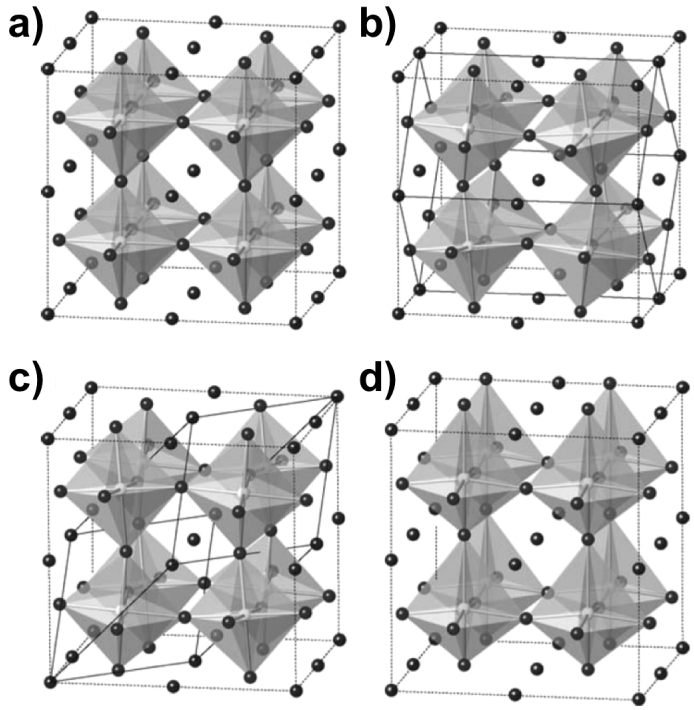

Figure 1.3: Four types perovskite structures as $2 \times 2 \times 2$ pseudocubic cells. (a) $Pm\bar{3}m$ (cubic: e.g., $SrTiO_3$). (b) $Pbnm$ (orthorhombic: e.g., $SrRuO_3$). (c) $R\bar{3}c$ (rhombohedral: e.g., $La_{0.7}Sr_{0.3}MnO_3$). (d) $P4mm$ (tetragonal: e.g., $PbTiO_3$). The orthorhombic and rhombohedral unit cells are shown in (b) and (c). Adapted from Ref. [19].

Most perovskite oxide structures are not perfect cubics due to the size mismatch between A and B cations. Indeed, cation displacements within octahedra and tilting of octahedra are common distortions in perovskite lattice structures, which result in an equilibrium structure with lower group symmetry compared with that of perfect cubic structure. To describe the structure distortion in perovskite structures, the tolerance factor is introduced and defined as the size mismatch between A- and B-site cations as follows:

$$\Gamma = \frac{r_A + r_O}{\sqrt{2}(r_B + r_O)}, \tag{1.1}$$

where r_A, r_B and r_O are the ionic radii of the A, B, and O ions, respectively. In this definition, the perfect cubic structure has a tolerance factor close to 1 (Fig. 1.3a). As the size of A cation decreases, octahedra tilting is induced to minimize the A-site coordination volume, thus, the B-O-B bond angle deviates from 180°, which leads to rhombohedral (Fig. 1.3b) and eventually orthorhombic (Fig. 1.3c) structures. On the other hand, as the size of A cation grows, instead of the octahedral tilt, the cation displacement is introduced as a distortion to minimize the total energy, which usually leads to a tetragonal structure (Fig. 1.3d). We note that the highly versatile electronic properties of complex oxides are usually associated with structure transitions. For example, in the rare-earth nickelate $RNiO_3$ series of compounds, the B-O-B bond angle distortion can decrease the one electron bandwidth due to the decrease of the d-electron transfer amplitude between B site cations, and as a consequence which might lead to a metal-insulator transition associated with the structure transition. [20]

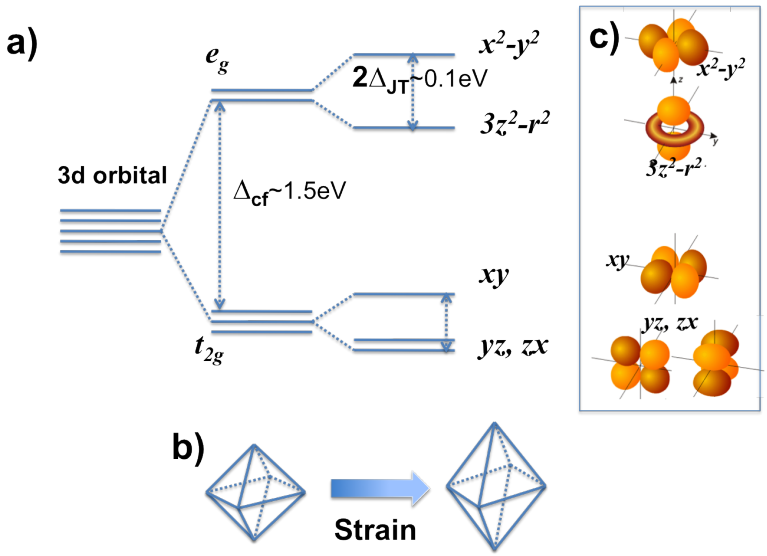

Figure 1.4: Crystal field splitting in a perovskite structure. (a) The oxygen octahedral crystal field breaks the degeneracies between the triplet t_{2g} (d_{xy}, d_{yz} and d_{xz}) and doublet e_g ($d_{x^2-y^2}$ and $d_{3z^2-r^2}$) orbitals with the crystal field of ~1.5 eV. The application of an external perturbation such as epitaxial strain (b) will further lift the degeneracies of e_g and t_{2g} with the final energy occupation of the orbitals as shown in (c).

In the ABO_3 structure, the B site cation is usually chosen from transition metal oxides (e.g. Ti, V, Cr, Mn, Fe, Co, Ni, Cu and so forth), which is responsible for numerous interesting phenomena as a consequence of strong electron interactions between the partially filled d-orbitals in the B site cations. Regardless of the detailed structure variants in the perovskite structure, the B site cation is always surrounded with the six nearest-neighbor oxygen anions. As one would expect, due to

the Coulomb repulsion between the d orbital electrons and the surrounding charges from oxygen, the energy of the d-orbital increases as the oxygen anions approach the B site cations. Thus, the crystal environment of such oxygen octahedra breaks the five-fold degenerated d orbitals into two high energy e_g orbitals($d_{x^2-y^2}$ and $d_{3z^2-r^2}$) and three low energy t_{2g} orbitals (d_{xy}, d_{yz} and d_{xz}), as shown in Figure 1.4a. The deformation of the octahedral structures due to internal (Jahn-teller distortion) or external (e.g. epitaxial strain) perturbations (Fig. 1.4b) can lift the degeneracies between the e_g and t_{2g} orbitals further to reach an energy occupation configuration as shown in Figure 1.4c.

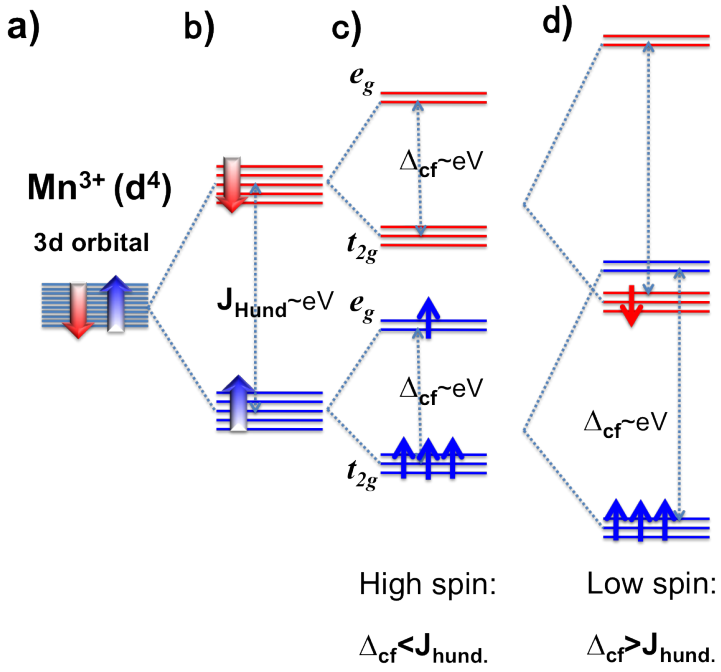

Figure 1.5: Possible spin configurations as a result of competition between crystal field and Hund coupling. The Hund coupling (J_{Hund}) lifts the degeneracies between the spin up and spin down states (b). The competition between Hund coupling and crystal field splitting determines the spin states, with $\Delta_{cf} < J_{Hund}$ and $\Delta_{cf} > J_{Hund}$ corresponding to high-spin (c) and low-spin (d) states respectively.

Similarly, the Hund's coupling between the spins on the same site lifts the degeneracies between the spin-up and spin-down states (Fig. 1.5b). The competition between the Hund's coupling and the crystal field spitting determines the spin occupation states in the transition metal elements. In the cases of the Hund coupling is larger than the crystal field, electrons will occupy the high-spin configuration. For example, in the high spin configuration, the Mn^{3+} cation has a total spin of $|S| = 2$. On the other hand, if the Hund coupling is smaller than the crystal field, the electrons will occupy the energy levels with the low-spin configuration, resulting in a total spin

of $|S| = 1$ for Mn^{3+} cation. An interesting model system is $LaCoO_3$, which shows a low-spin to high-spin transition at 100 K for Co^{3+} ions. [21, 22]

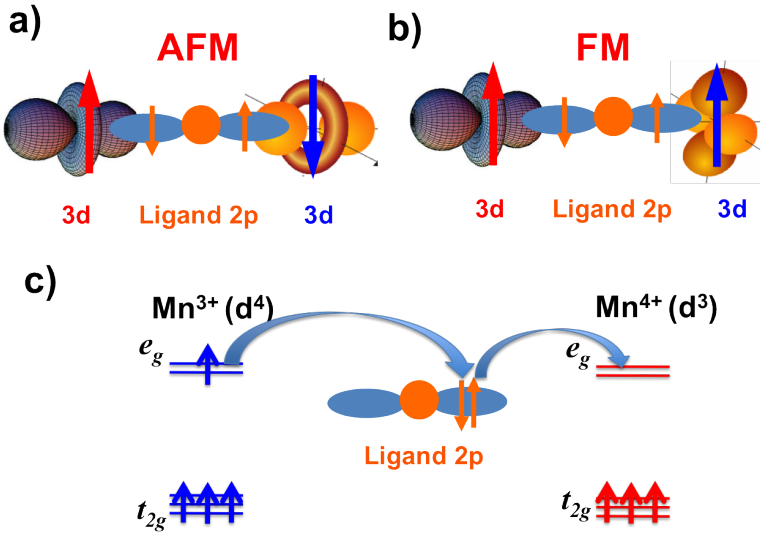

Figure 1.6: Schematic illustrations of magnetic couplings between transition metal ions. (a) The antiferromagnetic superexchange coupling between half-filled and half-filled orbitals. (b) The ferromagnetic superexchange coupling between half-filled to full (or vacant) orbitals. (c) Double exchange coupling between Mn ions.

Up to now, we have introduced the basic concepts about the spin configuration of magnetic cations in perovskites. The next question would be how the spins located at different magnetic cations couple with each other. For simple transition metals (e.g. Fe, Co and Ni), the direct coupling between the nearest neighbor atoms is the driving force for the magnetism. However, in transition oxide materials, e.g. MnO, despite having a non-magnetic oxygen anion sitting in-between, the two next-to-nearest neighbor magnetic Mn cations manage to interact strongly with each other, resulting in antiferromagnetic ground state. To understand this magnetic coupling, superexchange was first proposed by Hendrik Kramers in 1934 [23], which was later formally developed by Phillip Anderson in 1950 [24]. In 1950's, a set of semi-empirical rules were further set up with the seminal works of both John B. Goodenough and Junjiro Kanamori [25–27], which is now referred to as the Goodenough-Kanamori rule, or more accurately Goodenough-Kanamori-Anderson (GKA) rule. In the GKA rule, the magnetic coupling between magnetic cations is determined by orbital occupation states as well as the B-O-B bond angle. For simplicity's sake, here we only deal with the case with the bond angle equal to 180°. Figures 1.6a and 1.6b show a schematic illustration of two possible magnetic interactions between two magnetic cations. In the superexchange coupling, a virtual electron hopping (exchange) process between oxygen anions and magnetic cations was proposed. By Hund's rule, the spin orientation of a virtual hopping electron must be the same as the rest of electrons in magnetic

ions with empty orbitals; while it changes to antiparallel for half-filled orbitals. Thus, the magnetic coupling between two half-filled (or empty) orbitals is antiferromagnetic (Fig. 1.6a), while the coupling changes to ferromagnetic between an half-filled and full (or vacant) orbitals (Fig.1.6a). Although for most cases, the GKA rule can be taken as the rule of thumb to predict the magnetic coupling between transition metal ions, a detailed analysis is still required for complicated cases, e.g. deformation of the bond angle, competition between direct coupling and superexchange and strong spin-orbital coupling.

We would like to emphasize that in the superexchange coupling, the electrons do not hop between different atomic sites, thus it is only suitable to explain the magnetic coupling without charge transfer. Instead, a coupling mechanism called double exchange interaction was proposed by Clarence Zener, or called Zener coupling to account for the magnetic coupling in doped manganites with mixed valence states, which is usually metallic and the electron can hop from one site to another through the mediating oxygen anions. [28] Because the O^{2-} ion has full p-orbitals, the movement from one ion through O^{2-} to another ion involves two steps, in which one of the electrons hops back and forth between the two Mn ions across the oxygen, as shown in Fig. 1.6c. The electron is thus delocalized over the entire structure, and the material is conducting. Following Hund's rule, the hopping electron has the same spin orientation as both the ions, since the spin-flips are not allowed during the hopping process. Therefore, a ferromagnetic coupling configuration between different ions is achieved.

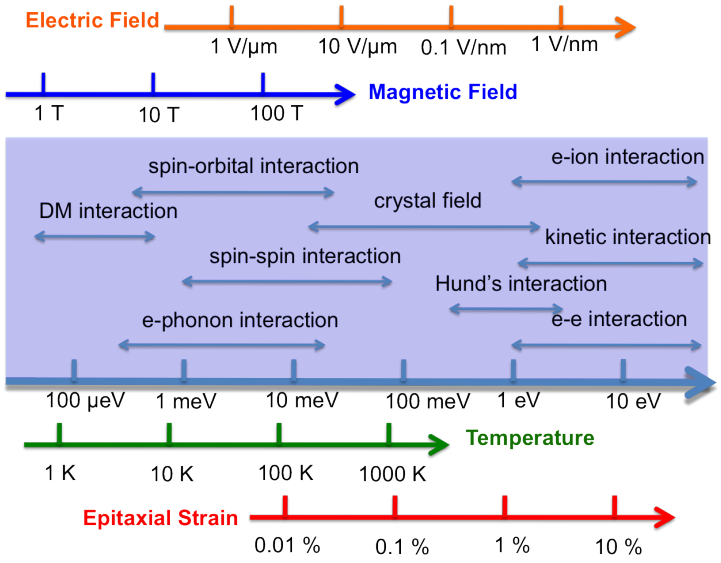

Figure 1.7: Schematic illustration of relevant energy scales for various interactions in complex oxide materials and commonly-used external perturbations.

Finally, we note that the essence of complex oxide systems lies at the subtle inter-

play between electron, spin, orbital and lattice degrees of freedom. These interactions lead to the emergence of intriguing novel ground states and phase transitions. Figure 1.7 illustrates the energy scales for various interaction mechanisms in complex oxide materials. Of all the interactions, the Coulomb interaction is one of the strongest ones, which is usually the driving force of the other coupling mechanisms and corresponding physical properties. On the other hand, although the small energy interactions, including spin-orbital interaction, electron-phonon interaction, and Dzyaloshinskii-Moriya interaction [29–31], are typically several orders of magnitude smaller than Coulomb interaction, they are responsible for many exotic properties in the materials, such as topological insulator [32], high temperature superconductivity [33] and multiferroic [34], respectively.

To summarize, a quick tour of the physics concepts in perovskite complex oxides is given in this section as the prerequisite knowledge for this study. In the rest of this chapter, we will continue to introduce how these physics concepts can lead to interesting coupling phenomena across heterointerfaces.

1.1.2 Charge reconstruction

As noted in Fig. 1.7, the strongest coupling in complex oxides is probably the Coulomb (or charge) interaction. Thus, we first give a brief review on how the charge reconstruction can happen at heterointerfaces and lead to interesting functionalities.

The condition of charge neutrality requires a perfect match between the valence states of all the ions in oxide materials. Taking the ABO_3 structure as an example, if we assign the valence state of the oxygen anion to be O^{-2}, the A and B cations can be chosen from the following pairs: $A^{4+}B^{2+}$, $A^{3+}B^{3+}$, $A^{2+}B^{4+}$ or $A^{1+}B^{5+}$. The rule of thumb is that the summary of valence states of all the ions in the chemical formula must be equal to zero. The slight charge imbalance can also be compensated with either valence change of the cations or oxygen vacancies, which most of the time will lead to lattice distortions and likely totally difference structure phases. The growth of heterostructure with valence mismatched materials could in principle lead to nontrivial local atomic and electronic structures, and usually is associated with the presence of defect states and dangling bonds at the interface. [36] Surprisingly the study of heterointerfaces built with perovskite oxides $SrTiO_3$ (STO) and $LaAlO_3$ (LAO), reveals another possible interface electronic reconstruction, i.e. a high-mobility electron gas at the interface, although both STO and LAO are very insulating. [7] The mechanism of this interesting phenomenon lies in the so-called "polar discontinuities" or "polar catastrophe". [35] Figures1.8a and 1.8b show a structural illustration of two possible atomic stacking sequences of LAO and STO heterostructures. We note that both LAO and STO have typical perovskite ABO_3 structure, which is composed of alternating AO and BO_2 layers along [001] direction. Thus, the growth of LAO/STO heterostructure can lead to two types of interfaces: LaO/TiO_2 and AlO_2/SrO, as shown in Figure 1.8. In STO, both $Sr^{2+}O^{2-}$ and $Ti^{4+}{O_2}^{4-}$ layers are charge neu-

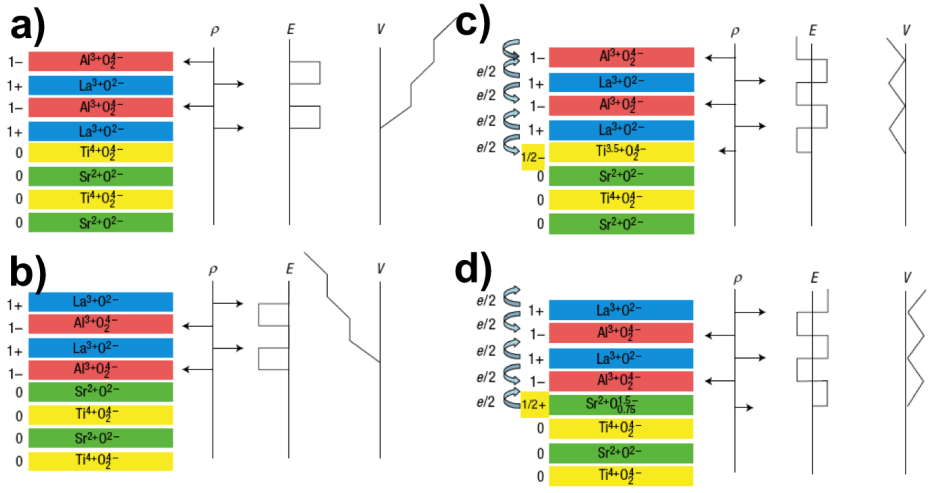

Figure 1.8: Illustration of polar catastrophe for $LaAlO_3$ and $SrTiO_3$ heterostructures with different interface terminations. (a) Unreconstructed LaO/TiO_2 interface has a non-negative electric field, leading to the divergence of the electric potential with thickness. (b) Similar but opposite potential profile occurs in the AlO_2/SrO interface. The divergence catastrophe at the interface can be avoided by either adding (c) or removing (d) half an electron from the interface for LaO/TiO_2 and AlO_2/SrO interfaces, respectively. Adapted from Ref. [35]

tral, while charge states in the LAO are positive for $La^{3+}O^{2-}$ layer, and negative for $Al^{3+}{O_2}^{4-}$ layer. As a consequence of the valence (or charge) mismatch, a polarity discontinuity arises at the interface, leading to divergent electrostatic potential, which is called "polar catastrophe". To avoid the associated large energy cost, a net charge transfer across the interface is energetically favorable, which results in electron doping at the LaO/TiO_2 interface and hole doping at the AlO_2/SrO interface, as shown in Figures1.8c and 1.8d.

Figure 1.9a shows typical electrical transport measurements across LAO/STO interfaces, with interfacial configurations of both LaO/TiO_2 and AlO_2/SrO. In the case of LaO/TiO_2 interface, a metallic state is formed across the interface, and Hall measurements prove the carrier type to be electron. On the other hand, the AlO_2/SrO interface is found to be insulating, although a hole-doped interface is expected. This effect might be due to a lack of available mixing valence states of Ti ion at the interface to accommodate the extra holes. Instead, a structural reconstruction with oxygen vacancies forming and compositional roughening at the interface is induced. [38] Moreover, it is worth noting that the sheet resistance of the LaO/TiO_2 interface is highly sensitive to growth conditions and the associated oxygen vacancy concentration, as shown in Figure 1.9b. For samples grown in an ultra-high vacuum condition, oxygen vacancies are induced at the STO substrate, which provides a conducting path for

the electrical transport. [39] For samples grown with higher oxygen partial pressure, the oxygen vacancy concentration is much reduced. Depending on the concentration, a rich spectrum of electronic states, including magnetism [40] and superconductivity [41] can be achieved, as shown in Figure 1.9c.

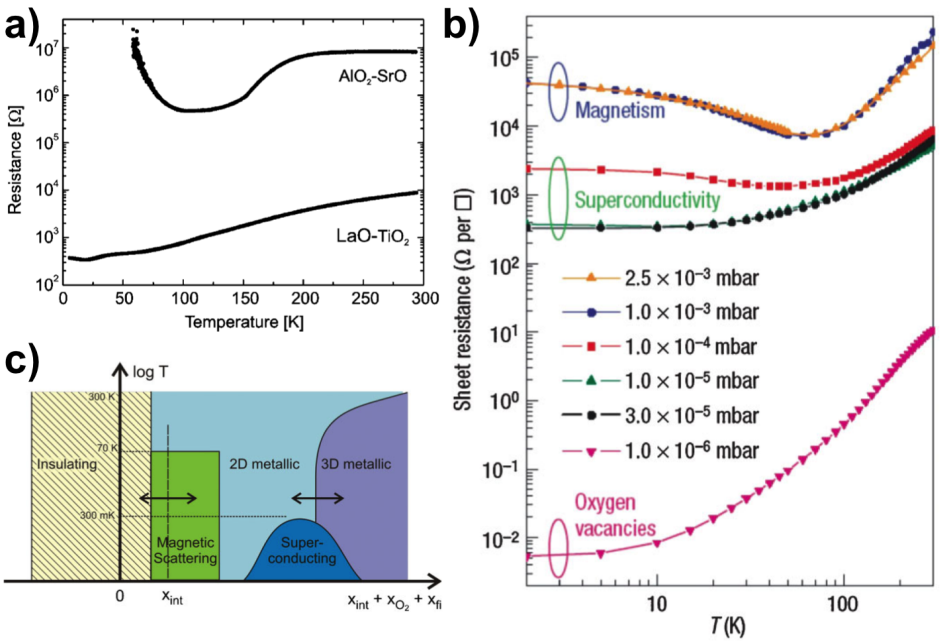

Figure 1.9: Electrical transport measurements across the LAO/STO interfaces. (a) Temperature dependence of sheet resistance of LaO/TiO_2 and AlO_2/SrO interfaces. (b) Temperature dependence of the sheet resistance for LaO/TiO_2 interfaces grown with different oxygen pressure. (c) Phase diagram of LaO/TiO_2 interface as a function of doping. (a) and (c) are adapted from ref. [37]. (b) is adapted from ref. [38].

Although both LAO and STO are nonmagnetic, magnetotransport experiments have revealed (Figure 1.10a) a large negative magnetoresistance and magnetic hysteresis at low temperature. [40] Despite the unusual shape of the hysteresis with peaks in the hysteresis occurring on the opposite side of zero, the fact that it exists suggests the switching of certain magnetic order at the interface. [42] The mechanism of this interesting spin coupling is still not clear. Growth of the samples in a slightly reduced pressure can control the oxygen vacancies in a manner so as to achieve a completely novel state of matter, superconducting state confined at the interface. [41] Although the transition temperature of 200 mK is very close to T_c of doped STO [43], the LAO thickness dependence [41] as well as the electric-field tunable superconductor-insulator phase transition [44], strongly suggests that this is truly an interfacial effect.

This section gives a quick review of the electronic reconstruction at the interface of insulating LAO and STO. Previous studies have revealed a nontrivial and potentially

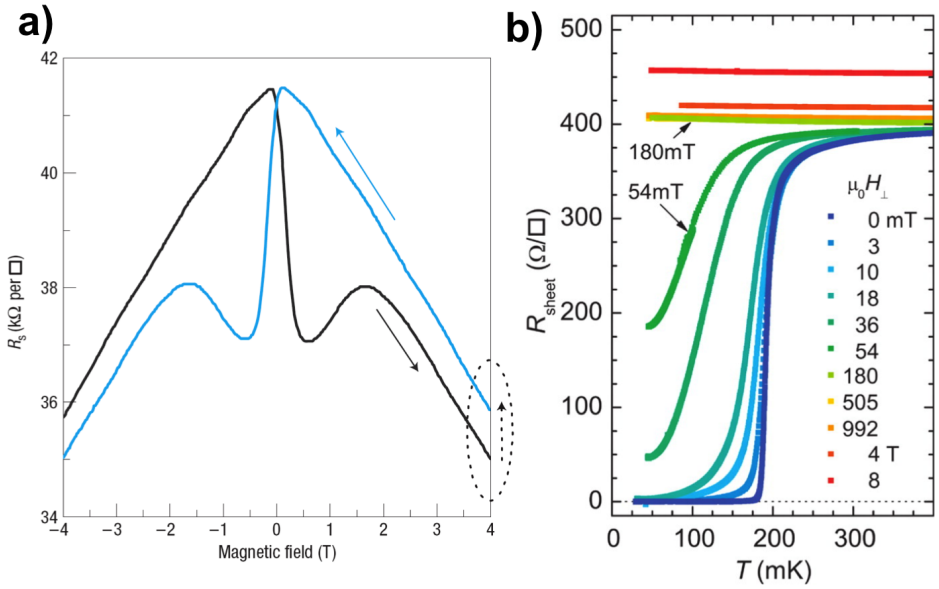

Figure 1.10: Emergent states of matter at the LAO/STO interface. (a) Magnetotransport of LAO/STO interface. Adapted from ref. [40] (b) Temperature dependence of sheet resistance of an eight unit-cell sample with magnetic field applied perpendicular to the interface. Adapted from ref. [41]

useful high-mobility two-dimensional electron gas at the interface, which also exhibits magnetic, and even superconducting properties due to the so-called "polar discontinuity" (valence mismatch) across the interface. This has triggered a wide range of research on exploring and understanding the novel interfacial phenomena [37,45], so as using the intriguing interface electronic state to achieve novel functionalities [46–48]. In chapter 3 of this dissertation, we will discuss a macroscopic impact of this interfacial effect.

1.1.3 Spin reconstruction

In addition to electronic reconstruction discussed in the previous section, spin reconstruction can also occur at the interface. In this section, we will review two types of spin reconstruction: artificial design of magnetic coupling and interfacial spin frustration.

In transition metal oxides, the magnetic coupling between different magnetic ions are determined by both d electron occupation number and associated orbital structure though the GKA rule as discussed before. Taking $LaFeO_3$ (LFO) as an example, the Fe ion has valence state of 3+, with five d electrons. Following the GKA rule, the magnetic coupling between the nearest neighbor Fe ions is antiferromagnetic. Thus LFO is a G-type antiferromagnetic, meaning ferromagnetic coupling in the (111) plane,

while antiferromagnetic coupling between the nearby planes. $LaCrO_3$ (LCO) is another simple model, in which the Cr^{3+} has d^3 configuration, and the nearest neighbor Cr ions is coupled antiferromagnetically as well. Interestingly, from the GKA rules, the coupling between Fe^{3+} (half filled) and Cr^{3+} (empty) is expected to be ferromagnetic. Thus, it would be interesting if one could fabricate the heterostructure along the [111] axis, as shown in Figure 1.11. Especially, when the thicknesses of both LCO and LFO are chosen to be one unit-cell, the ground state of such designed structure is expected to be ferromagnetic. In the study of Ueda *et al.* [15], a magnetization value of $3\mu_B$ per site was reported, which is close to theoretical expectation value of 4 μ_B per site. However, we note that the actual value of magnetization at such heterostructure is still under debate. [49, 50]. Nevertheless, this work has triggered great interest to study the magnetic properties of artificial designed double perovskite structures. More interesting, a recent first-principle calculation has predicted a multiferroic ground state for $BiFeO_3/BiCrO_3$ double perovskite structure [51], which has been confirmed with subsequent experiments [52], although the exact coupling between the ferromagnetic and the ferroelectric ordering is still unexplored.

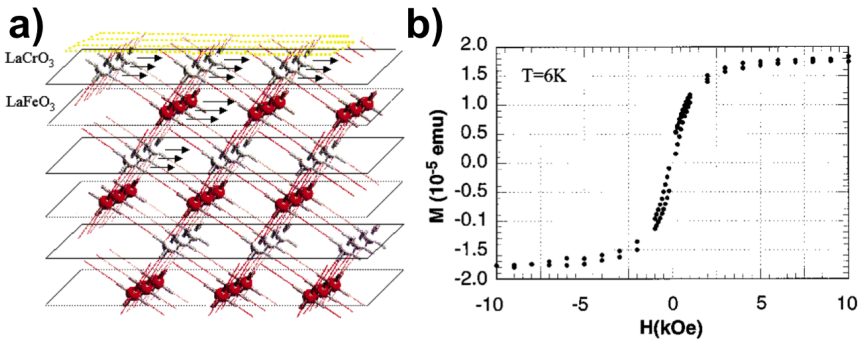

Figure 1.11: Artificial design of the magnetic coupling at the $LaFeO_3/LaCrO_3$ superlattice. (a) Schematic diagram for the construction of the $LaFeO_3/LaCrO_3$ superlattice along [111] direction. (b) Hysteresis curve of the LFO/LCO superlattice measured parallel to the film plane at 6 K. Adapted from Ref. [15]

Another type of interesting interfacial spin coupling is spin frustration, which happens when two materials with different spin structures are fabricated together within atomically precise control. As an example, figure 1.12 shows a heterostructure built with high temperature superconductor $YBa_2Cu_3O_7$ (YBCO) and ferromagnet $La_{2/3}Ca_{1/3}MnO_3$ (LCMO). [16] In the (001) plane, the Mn ions are coupled ferromagnetically; while the Cu ions are coupled together antiferromagnetically. Thus no matter what is the coupling mechanism involved between the Mn and Cu ions across the interface, such a spin configuration is not energetically favorable, and spin frustration is expected to be induced. This interfacial spin reconstruction is confirmed by x-ray circular dichroism (XMCD) measurements, which reveal an interfacial fer-

romagnetism on the Cu ions coupled antiferromagnetically with the Mn ions. Such a magnetic coupling configuration can further provide us the information about the interface orbital structure. [16,53] Furthermore, the spin frustration can also apply to the systems with ferromagnet/antiferromagnet [54], antiferromagnet/antiferromagnet with different spin structures [55], antiferromagnet/nonmagnetic [56] materials at the interface.

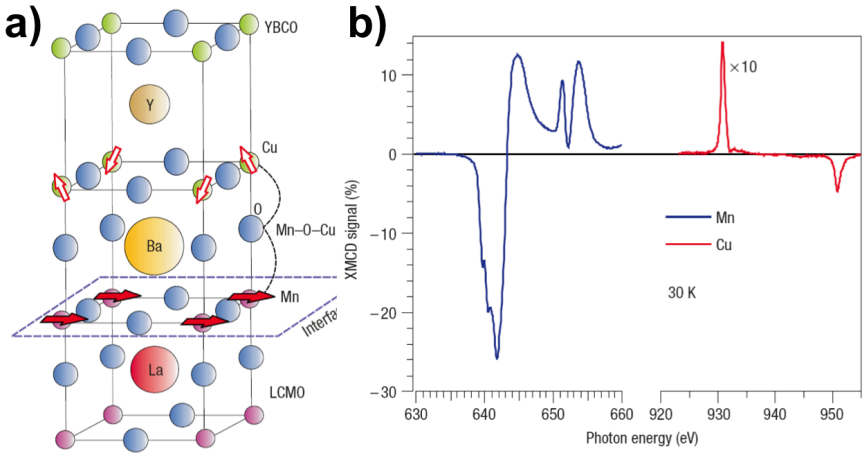

Figure 1.12: Spin reconstruction at the $YBa_2Cu_3O_7$ and $La_{2/3}Ca_{1/3}MnO_3$ interface due to spin frustration. (a) Atomic stacking sequence at the YBCO/LCMO interface. (b) X-ray magnetic circular dichroism obtained from Cu and Mn core-level absorption spectra, demonstrating the spin configurations across the interface. An interfacial ferromagnetism is induced at the superconducting YBCO layer due to the spin frustration, which is antiferromagnetically coupled with the Mn spins. Adapted from Ref. [16]

This section introduces the basic concepts of the interfacial spin reconstruction. In this dissertation, using the model system of multiferroic BFO and ferromagnet LSMO, we studied the interface spin structure in detail. Moreover, the electric-field control of this interface spin structure is also achieved, which has great implications on the study of magnetoelectric couplings.

1.2 Multiferroics and Magnetoelectric Coupling

This section introduces key concepts of multiferroics and magnetoelectric coupling. A few strategies to achieve the electric-field control of magnetism in the form of heterostructures will also be discussed.

1.2.1 Multiferroics

Multiferroics, by definition, are materials exhibiting simultaneously more than one primary ferroic order parameters, namely, ferroelectricity, ferromagnetism, ferroelasticity and ferrotoroidicity. [17, 57–65] Of all possibilities, materials, which have both ferroelectricity and ferromagnetism, are particularly intriguing because of their great potential for applications(Figure 1.13a). Researchers are seeking a pathway to couple these two orders together to achieve the control of charge state by applied magnetic fields or spin state by applied electric voltages, and thus using this to build new generation of multi-functional devices. To design a good multiferroic which has both ferroelectricity and ferromagnetism in the same phase, one should first consider the basic properties or requirements for those. [66]

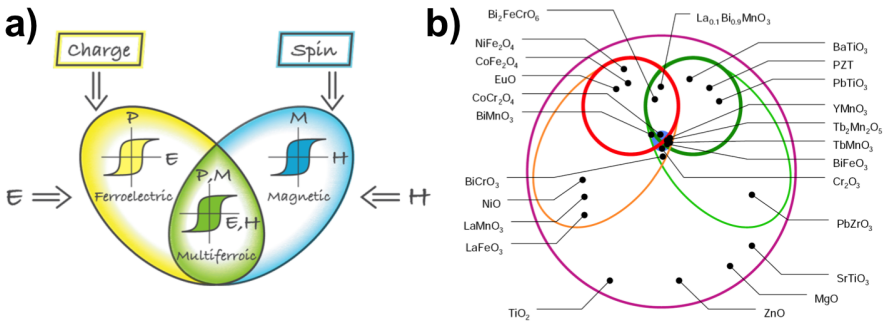

Figure 1.13: Introduction of multiferroics. (a) Magnetoelectric coupling in multiferroics. Multiferroics are materials which have simultaneously (anti-) ferromagnetic and ferroelectric orders. Ferroelectric are materials electrically polarizable and with finite remnant polarization, while ferromagnets are materials are magnetically polarizable with finite magnetization. The interplay between these two orders could induce an interesting coupling phenomenon, called magnetoelectric coupling, in which there is a magnetic response to an electric field, or, vice versa, namely the control of polarization by magnetic field. Adapted from ref. [63] (b) Classification of multiferroics. Multiferroics corresponding to the intersection between the categories of ferroelectricity (red) and ferromagnetism (green). The blue circle in the middle denotes systems exhibiting a magnetoelectric coupling, which however dose not perfectly coincides with multiferroics. Adapted from ref. [62].

A material is defined as ferroelectric when it has more than one possible electrically switchable spontaneous electric polarization states. In ferroelectric materials, due to the presence of remnant polarization, the spatial inversion symmetry is broken. Moreover, since ferroelectric materials are electric switchable, they must be good dielectrics, thus by definition good insulators. One good example of classical ferroelectric is $BaTiO_3$, in which the d^0 orbital of Ti^{4+} cation is believed to be essential for the origin of ferroelectric distortion, through a strong hybridization with surrounding oxygen $2p$ orbitals. In analogy, ferromagnetism is a property of certain

materials, which have spontaneous long-range spin-orderings, resulting in a remnant and magnetic field-switchable magnetization. In magnetic materials, the time reversal symmetry is broken, however, the spatial inversion symmetry is still invariant. One group of well-known ferromagnetic materials are transition metals Ni, Co, Fe and their alloys, in which the driving force for the ferromagnetism is the imbalance of the density of states between the spin-up and spin-down states below the Fermi surface. Another group of interesting ferromagnetic materials are doped manganites, in which the double exchange coupling between B site transition ions (Mn) aligns the spin orientation and results in a net magnetization. [28] Nevertheless, in both groups, the d orbitals are partially filled, thus these materials are expected to be metallic. In summary, ferroelectric and ferromagnetic materials have very different requirements in several aspects, including symmetry, chemistry and electronic properties. Firstly, in a multiferroic, both the time reversal and spatial inversion symmetries are broken. This requirement limits multiferroic to a small category with only 13 point groups over 122 total magnetic space groups. [61] Secondly, ferroelectrics, by definition, are insulators, while ferromagnets are usually metallic in nature. Finally, classical ferroelectrics have B site ions with a formal d^0 orbital configuration; while ferromagnets typically require unoccupied d orbitals to achieve strong ferromagnetic coupling between transition metal ions. Clearly, the exclusive requirements between the ferroelectricity and ferromagnetism results in the scarcity of multiferroics. Figure 1.13b provides a brief classification of multiferroics, which are still very rare although the requirement about electric properties is partly relieved by including antiferromagnetism and ferrimagnetism.

	Mechanism of inversion symmetry breaking	Materials
Proper	Covalent bonding between $3d^0$ transition metal (Ti) and oxygen	$BaTiO_3$.
	Polarization $6s^2$ lone pair of Bi or Pb	$BiMnO_3$, $BiFe_3$ and $Pb(Fe_{2/3}W_{1/3})O_3$
Improper	structural transition "Geometric ferroelectrics"	K_2SeO_4, Cs_2CdI_4, hexagonal $RMnO_3$
	Charge ordering "Electronic ferroelectrics"	$LuFe_2O_4$
	Magnetic ordering "Magnetic ferroelectrics"	Orthorhombic $RMnO_3$, RMn_2O_5, $CoCr_2O_4$

Table 1.1: Classification of ferroelectrics. Adapted from ref. [60]

To circumvent the fundamental contraindication discussed above, a few strategies have been explored as shown in table 1.1. The first one is to induce ferroelectricity with A site ions, in contrast to traditional B site d^0 ions. One example is the Bi based

compounds (such as $BiFeO_3$ and $BiMnO_3$), in which the origin of the ferroelectricity is the coupling between the two 6s electrons (called lone pair) in Bi cations and the surrounding oxygen anions. [67] In these materials, since the ferroelectric and magnetic orders are associated with different ions, thus it is possible to integrate them together in the same phase. $BiMnO_3$ is an interesting material, in which although both the magnetization and ferroelectric polarization are rather large, the coupling between these two orders, however, is still very weak. [62, 68–71] $BiFeO_3$, on the other hand, has strongly coupled ferroelectric and antiferromagnetic orderings [72,73], which make it fundamental intriguing for the study of the magnetoelectric effect, especially in the form of heterostructure with ferromagnetic materials. [17,61,74] Another strategy is to break the spatial inversion symmetry in an "improper" way, which includes structural transition [75–77], charge ordering [78–80] and magnetic ordering [81, 82]. Because of the strong correlation between the ferroelectric ordering and the magnetic structure in these materials, it has been demonstrated that the ferroelectric polarization could be reversibly controlled with the application of a magnetic field. However, it is worth pointing out that the associated ferroelectric polarization in these systems is much smaller than traditional ferroelectrics and the manipulation requires a huge magnetic field (several Tesla). Therefore, studies of these improper ferroelectrics are scientifically important, while less interesting from the application point of view. Finally, it is worth pointing out that recent first-principle calculations [83] predicted that the ground state of $EuTiO_3$ compound could be tunned from paraelectric and antiferromagnetic to ferroelectric and ferromagnetic by using epitaxial stain. This prediction has been experimentally demonstrated a subsequent experiment. [84] However, a direct demonstration of the interaction between ferroelectric and ferromagnetic orders is still demanded.

In summary, in the past decade, substantial research has been carried out towards the exploration and understanding of multiferroics and magnetoelectric couplings. However, we note that so far, researchers still have not found any material showing strongly coupled ferroelectricity and ferromagnetism in the same phase. Instead, people proposed to use heterostructures composed with two or more materials with different properties/functionalities to achieve the magnetoelectric coupling through interfacial couplings [17, 61], and a brief review of which is given in the following section.

1.2.2 Magnetoelectric coupling: electric-field control of magnetism

Although from the scientific point of view, both the electric-field control of magnetism and the modification of polarization by a magnetic field are equally important, the former one is the central question of the multiferroic study due to its great potentials for applications. Figure 1.14 presents a sketch of a possible memory element

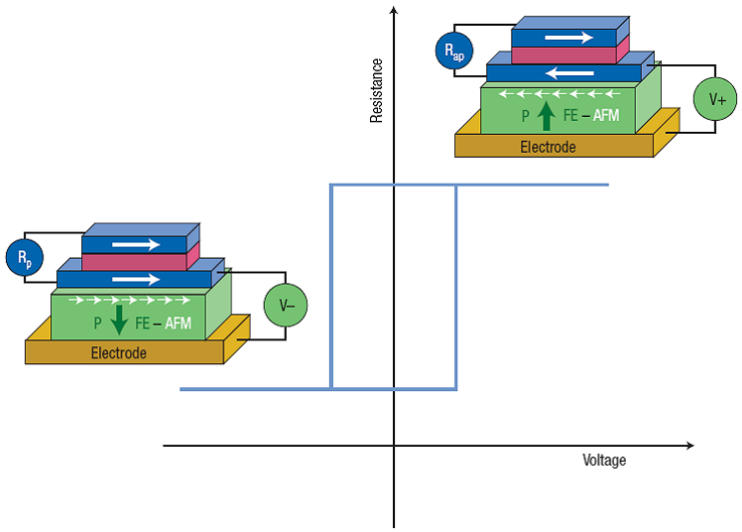

Figure 1.14: Sketch of a possible memory element based on magnetoelectric coupling. Binary information is stored by the magnetization direction of the bottom ferroelectric layer. The information is read out by the resistance of a magnetic trilayer, due to the dependence of the resistances on the spin alignment configuration between these two ferromagnetic layers. The writing process is achieved by using the ferroelectric polarization switch to control the spin orientation at ferromagnetic layer through the exchange-bias coupling. Adapted from ref. [85]

based on magnetoelectric coupling, in which the information is written with an electric field while read out by a typical giant magnetoresistance (GMR) configuration. Moreover, we note that to describe a ferromagnetic state, one needs at least three parameters, i.e. magnetization, magnetic anisotropy (or coercive field) and unidirectional anisotropy (or exchange-bias field). In this section, we will discuss several strategies to achieve the control of all these parameters in the form of heterostructures built with ferromagnet in intimate contact with other functional materials, such as ferroelectrics (e.g. $PbZr_{0.2}Ti_{0.8}O_3$, $BaTiO_3$), antiferromagnets (e.g. Cr_2O_3) and multiferroics (e.g. $YMnO_3$, $BiFeO_3$).

1) Control of the magnetization with ferroelectric polarization. The first order effect for the coupling between a ferromagnet and a ferroelectric would be the influence of ferroelectric polarization switch on the magnetic state, which has been realized recently in heterostructure forms containing ultrathin ferromagnetic manganites and ferroelectrics by both first-principle calculations [86, 87] and experimental measurements [88–90]. Molegraaf and co-workers have reported a remarkable control of magnetization via the ferroelectric polarization in a PZT (250 nm)/LSMO (4 nm) heterostructure. [88] Subsequently, Vaz *et al.* [89] used near edge x-ray absorption spectroscopy (XAS) to probe the valence state of Mn ions at the LSMO layer as a

function of external electric field, and found that the Mn valence state mimics the ferroelectric hysteresis and also the magnetization modulation loops. Thus, they have attributed the origin of this magnetoelectric coupling to the charge mediated tuning of magnetic ground states at the interface.

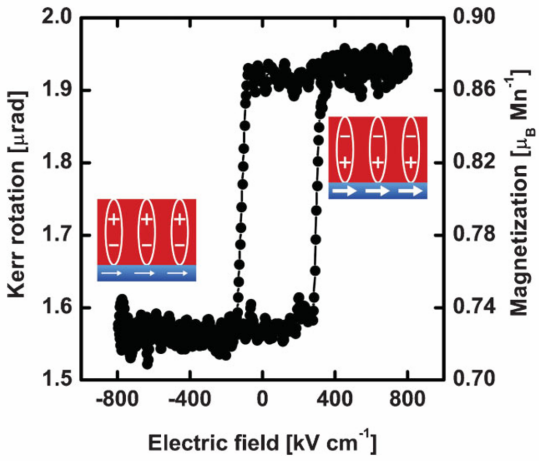

Figure 1.15: The electric-field control of magnetism with charge modulation in the ferroelectric/ferromagnet heterostructure. Magnetism as a function of the applied electric field in the $PbZr_{0.2}Ti_{0.8}O_3/La_{0.8}Sr_{0.2}MnO_3$ heterostructure measured at 100 K, with a MOKE magnetometer. Insets represent the magnetic and electric states in the thin LSMO layer (blue) and PZT layer (red). Adapted from ref. [88].

2) Manipulating the magnetization and magnetic anisotropy with the strain modulation. From the symmetry point of view, a ferroelectric material is also ferroelastic. Thus, the application of an external electric field will result in a structural distortion on the ferroelectric as well. Such a structural change will transmit to the magnetic layer through an interfacial strain coupling and alter its magnetization or magnetic anisotropy through the magnetostriction. Figure 1.16a shows that the magnetization of a LSMO layer could be tuned with the application of an electric field across ferroelectric (and also piezoelectric) $BaTiO_3$ substrates. [91] Such an interesting coupling could be related with the orbital degree of freedom at the LSMO layer, which guides the magnetic coupling mechanism involved. Another interesting experimental result is the recent finding in ferromagnetic metal alloy $Fe_{0.9}Ge_{0.1}$ grown in BSPT substrates, in which the ferroelastic switch leaves to two dramatically different magnetic states with almost zero coercive field in one case and finite coercive field in the other case, as shown in Figure 1.16b. [92, 93] The coercive field tracks the dependence of the piezoelectric switch under the application of an electric field. This coupling could be related with the changing of the magnetocrystalline anisotropy through strain effect. However, we would like to point out that despite a few phenomenological models have

been proposed to explain these interesting magnetoelectric couplings, the fundamental physics involved is still unclear.

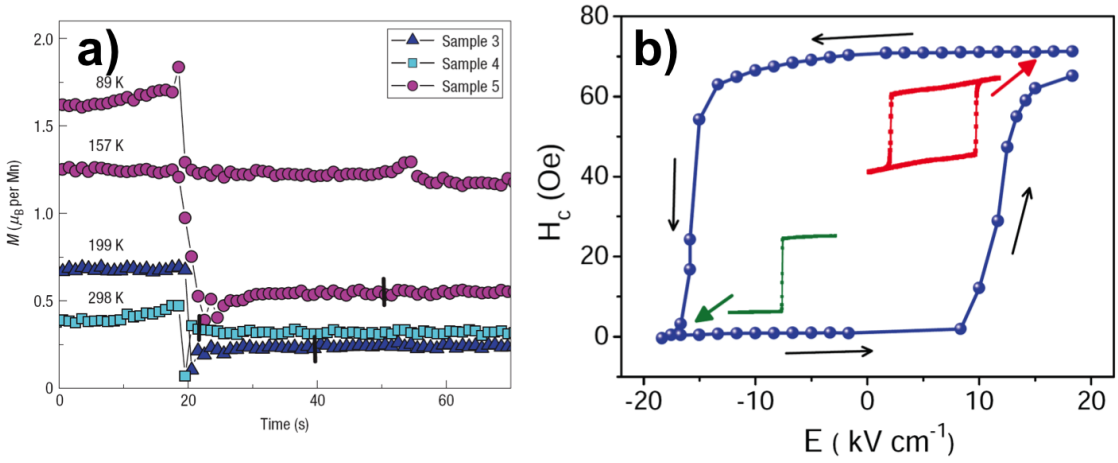

Figure 1.16: Electric-field control of magnetism with the strain modulation. (a) Control the magnetization of $La_{0.67}Sr_{0.33}MnO_3$ with the application of electric field across the ferroelectric $BaTiO_3$ substrates. The magnetization of the LSMO was monitored with a VSM as the function of time with and without the application of the electric field. For clarification, all electric field transition (turn on) are placed near 20 s. Transitions were recorded at 4 kV cm^{-1} (sample 3), 10 kV cm^{-1} (sample 4) and 6 kV cm^{-1} (sample 5 at both 89 K and 157 K). Adapted from ref. [91]. (b) Control the anisotropy energy (coercive field) of $Fe_{0.9}Ge_{0.1}$ film with the electric field applied across the morphotropic phase boundary $BiScO_3$-$PbTiO_3$ substrate. The insets show the representative Kerr hysteresis loops under two electric polarization states. Adapted from refs. [92] and [93].

3) Deterministic control of magnetic state with an exchange-bias effect. We note that to achieve the deterministic control of the magnetism, one needs to find a way to control the spin orientation by the application of an external electric field. One pathway is to use the magnetic unidirectional anisotropy (or exchange-bias coupling) of the ferromagnet layer. Exchange-bias coupling, resulting from the magnetic coupling between an antiferromagnet and a ferromagnetic layer, can lead to a shift of the magnetic hysteresis loop along the magnetic axis, thus pinning the orientation of the ferromagnetic layer. [96] Such a unidirectional anisotropy is mainly due to the presence of pinned uncompensated spins at the AFM layer, thus very sensitive to both the orientation of AFM spin axis and magnetic coupling strength across the interface. The concept of utilizing exchange-bias effect in magnetoelectric coupling is to use an electric field to control the orientation of the antiferromagnetic axis or magnetic coupling across the interface, so as to control the spin direction of the ferromagnet layer through exchange-bias coupling between antiferromagnetic and ferromagnetic layers. [17] Extensive studies have been carried out along this direction,

especially after the finding of multiferroics (e.g. $YMnO_3$ (YMO), BFO) with both ferroelectric and antiferromagnetic orderings. Researchers have demonstrated that the exchange-bias coupling between the multiferroic YMO and ferromagnet permalloy can be electrically tuned (as shown in Figure 1.17a). [94] By applying an external voltage across the YMO layer, the exchange-bias field decreases gradually and eventually disappears at 1.2 Volts, which however is irreversible. During this process, the electric field is likely employed to melt pinned spins at the AFM layer, instead of an actually control of the AFM axis. One parallel study is based on antiferromagnetic Cr_2O_3. Researchers have studied multilayer of $Cr_2O_3/(Co/Pt)_3$ and found that the exchange-bias field in this structure could be reversible control by using an electric field (Figure 1.17b). [95, 97] However, this control needs either a thermal cycling [95] or application of both electric and magnetic fields at the same time [97]. Thus, the key challenge regarding the magnetoelectric coupling by using exchange-bias effect still remains: how to achieve the deterministic (while reversible) control by using purely electric field?

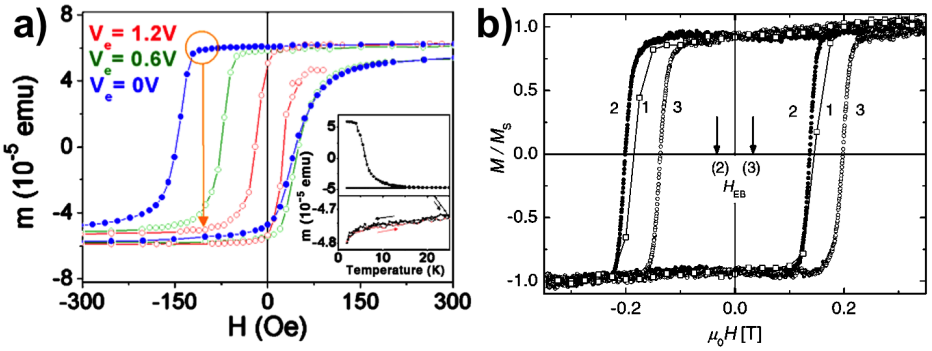

Figure 1.17: Electric-field control of magnetism through an exchange-bias effect. (a) Magnetization loops of $Py/YMnO_3/Pt$ measured at 2 K, after field cooling the sample from 300 K in 3 KOe field, under various biasing-voltage (V_e) value. Inset: temperature dependence of the magnetization at -100 Oe and zero electric field. Adapted from ref. [94]. (b) Normalized hysteresis loops of Cr_2O_3 (111)/ Pt 0.5 nm/[Co 0.3 nm/Pt 1.5 nm]$_3$/Pt 1.5 nm measured after the magnetoelectric field (combination of magnetic field and electric field) cooling. The magnetic field used was 0.6 T, while the electric field was chosen as 0 (1), -500 kV/m (2) and +500 kV/m (3), respectively. Adapted from ref. [95]

To summarize, this section reviews basic concepts of multiferroics and introduces several strategies to achieve electric-field control of magnetism in the heterostructure. Depending on coupling mechanisms involved, the magnetic states could be manipulated in three aspects, i.e. magnetization, magnetic anisotropy and unidirectional anisotropy. In this dissertation, using the model system of BFO/LSMO, we will demonstrate that all these aspects in the LSMO layer are strongly correlated with the ferroelectric polarization of BFO, thus the application of an electric field could control the magnetism of LSMO layer in a more comprehensive manner.

1.3 Organization of Dissertation

This dissertation is organized as follows. Chapter 1 provides a brief introduction to the background and key concepts of this dissertation. Chapter 2 focuses on the growth of BFO and LSMO heterostructures, as well as magnetic and ferroelectric characterizations. Chapter 3 discusses the fabrication of BFO/LSMO heterointerfaces and how the associated interfacial electronic structure could be used to control bulk ferroelectric polarization states. Chapter 4 introduces the exchange-bias coupling at the ferromagnetic and antiferromagnetic heterostructure and presents our experimental results in the case of BFO/LSMO heterostructure. Chapter 5 is dedicated to the study of spin configurations at the interface, which is strongly associated with the onset of the significant exchange-bias coupling observed. Chapter 6 presents the electric-field control of magnetic coupling across the interface with a ferroelectric field effect transistor device structure. Chapter 7 discusses the origin of the magnetoelectric coupling at the interface, which reveals the important role of the interplay between charge, spin, orbital and lattice degrees of freedom at the interface. Chapter 8 serves as a summary of the finding present in the dissertation as well as suggested future directions.

Chapter 2

Growth and characterization of $BiFeO_3/La_{0.7}Sr_{0.3}MnO_3$ heterostructures

2.1 Model system of $BiFeO_3/La_{0.7}Sr_{0.3}MnO_3$ heterostructures

2.1.1 Multiferroic $BiFeO_3$

$BiFeO_3$ (BFO) is the only room temperature multiferroic (antiferromagnetic and ferroelectric) so far, which has attracted great interest and extensive investigations in the past decade. [18] The perovskite BFO was first synthesized in a bulk polycrystalline form in the late 1950s [98], which by then was suspected to be both antiferromagnetic and ferroelectric. Detailed x-ray diffraction and neutron diffraction studies revealed that the BFO single crystal has a rhombohedral unit cell, built with two distorted perovskite cells connected along a pseudocubic [111] direction. [99,100] Moreover, the two oxygen octahedra in the unit cells are rotated clockwise and counterclockwise around the [111] direction by $\pm 13.8^\circ$, as shown in Figure 2.1a.

The understanding of magnetic structure of BFO is straightforward. Since Fe^{3+} cation has five d electrons, the nearest neighbor Fe cations are coupled antiferromagnetically between each other with the so-called superexchange coupling. Thus, BFO should have a robust G-type antiferromagnetic structure, as shown in Figure 2.1b. This finding was confirmed by neutron diffraction measurements in 1980s, which indicated that BFO was indeed G-type antiferromagnetic with Néel temperature of $\sim$673 K [100] and moreover possessed a cycloidal structure along [111] direction with the periodicity of $\sim$ 620 Å [101]. It is also worth pointing that the symmetry also permits a small canting of the antiferromagnetically aligned spins from the antiferromagnetic axis, resulting in a small magnetization due to the Dzyaloshinskii-Moriya

interactions. [29–31]

On the other hand, the ferroelectric nature of the materials remained under debate until 1970, when ferroelectric measurements revealed a ferroelectric polarization of 6.1 μC/cm^2 along the [111] direction of the crystal, [102] which is consistent with the rhombohedral group symmetry of the material. The chemical etching experiments on ferroelectric single domain samples later proved that the ferroelectric phase is stable from 4 to $\sim$ 1103 K (T_C 1103 K). [103] We note that different from traditional ferroelectrics, the origin of the ferroelectric nature in BFO is the two 6s electrons in Bi cation, which are hybridized with surrounding oxygen ions, leading to a large displacement of the Bi cation relative to the oxygen octahedra along the [111] direction. [67]

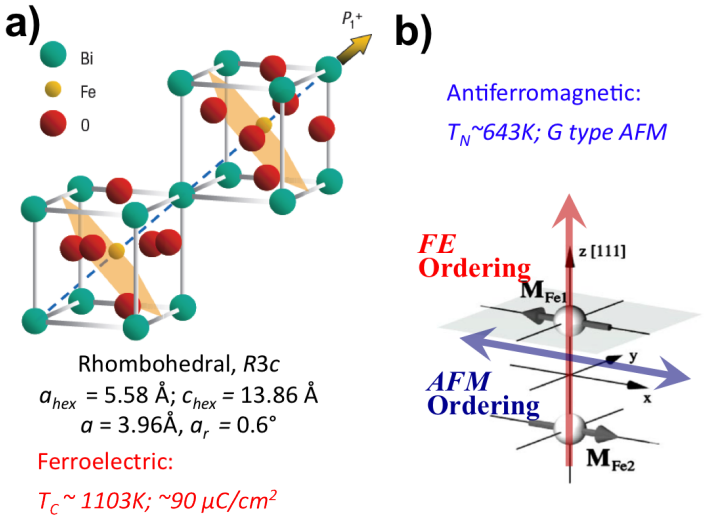

Figure 2.1: Schematic illustration of the ferroelectric and antiferromagnetic orderings in multiferroic $BiFeO_3$. (a) BFO has a rhombohedral structure with the ferroelectric polarization along the pseudocubic [111] direction. (b) G type antiferromagnetic ordering in BFO with a weak ferromagnetic moment in the (111) plane due to the spin canting.

After these initial findings, the study of BFO remained quiet for almost twenty years, mainly due to the small measurable ferroelectric polarization and the lack of a way to achieve significant magnetoelectric couplings in the bulk form. Things have been changed after 2003, when a study of high-quality BFO thin films reported an "enhancement" ferroelectric polarization of about 90 μC/cm^2 [104], which is almost the biggest ferroelectric polarization found by then. Subsequent study on high-quality BFO crystal revealed that this value is actually an intrinsic property of BFO compound. [105,106] The small polarization previously obtained in bulk samples is mainly due to the poor quality of the crystal used. More interestingly, the study in 2003 had also demonstrated a thickness-dependent magnetism and a magnetoelectric coupling coefficient as high as $3V/cmOe$. [104] However, the true nature of the magnetic prop-

erty remains unresolved [107], although the presence of second phase could likely be ruled out [108]. Nevertheless, the presence of high ferroelectric polarization as well as the antiferromagnetic ordering provides us another pathway to achieve the electric-field control of magnetism as what we have discussed in the previous chapter. [17] For example, a recent study demonstrated an electric-field control of local ferromagnetism using the heterostructure of BFO and CoFe. [74] It is worth noting that besides the magnetoelectric coupling, this compound (BFO) kept surprising the whole community with fascinating properties, such as switchable photodiode [109], giant open-voltage solar cell [110], strain induced morphotropic phase boundary [111], photostrictive effect [112], etc.

2.1.2 Ferromagnet $La_{0.7}Sr_{0.3}MnO_3$

The study of perovskite manganites could be traced back to 1950 [113], when researchers found that doped manganites could be both ferromagnetic and magnetic although the parent compounds are antiferromagnetic and insulating. This finding had triggered extensive studies on the magnetic and electric properties of manganite compounds and also given the birth to a few important physics concepts in condensed mater physics. The finding of colossal (thousandfold) magnetoresistance (CMR) effect in $La_{0.67}Ca_{0.33}MnO_x$ (LCMO) thin films by Jin *et al.* in 1994 [4, 5], spawned a hailstorm of research into manganites, which continues to the present day. After that, an enormous amount of research has been carried out on manganites with large variety of A-site cations, dopants and doping levels. [114]

Of all the possible compounds, $La_{1-x}Sr_xMnO_3$ (LSMO) attracts huge research interest since it is by far the only simple perovskite manganite with Curie temperature higher than room temperature, although the magnetoresistance is much reduced compared with other manganites, such as LCMO. This interesting difference could be understood based on the fact that Ca cation has a smaller ionic radius than that of Sr cation. Thus the perovskite tolerance factor in LCMO is reduced compared with LSMO, resulting in a larger oxygen octahedral rotations in the lattice. The larger structure distortion reduces the $Mn - O - Mn$ bond angles and bandwidth, leading to the smaller Curie temperature and larger magnetoresistance. Clearly, in the manganites system, the interplay between charge, spin, orbital and lattice degrees of freedom can lead to a rich spectrum of novel functionalities and physics. [114]

The phase diagram of LSMO is shown in figure 2.2. [115] On the left side is the parent compound, $LaMnO_3$, in which the Mn cation has d^4 orbital configuration. Its ground state is characterized with a orbital ordering pattern, thus A-type antiferromagnetic ordering and Mott insulating. On the right side is $SrMnO_3$, in which the Mn cation has d^3 orbital configuration, with the ground state of G-type antiferromagnetic ordering and band insulating. With progressive doping of LMO, various magnetic and charge ordered phases emerge. Besides the ferromagnetic metallic state formed at the doping level around 1/3, three types of charge ordering states are also

formed, located at x=1/8 (CO-I), 1/2 (CO-II) and 2/3 (CO-III). Despite doping of carriers into the mother compound, all these three regions are insulating, and with the ferromagnetic state for CO-I region and antiferromagnetic states for the other two. In the study of this dissertation, we choose the LSMO compound with the doping level of 0.3, mainly because of its promising ferromagnetic properties, with the highest Curie temperature of $\sim$ 380 K and almost 100 percent spin polarization.

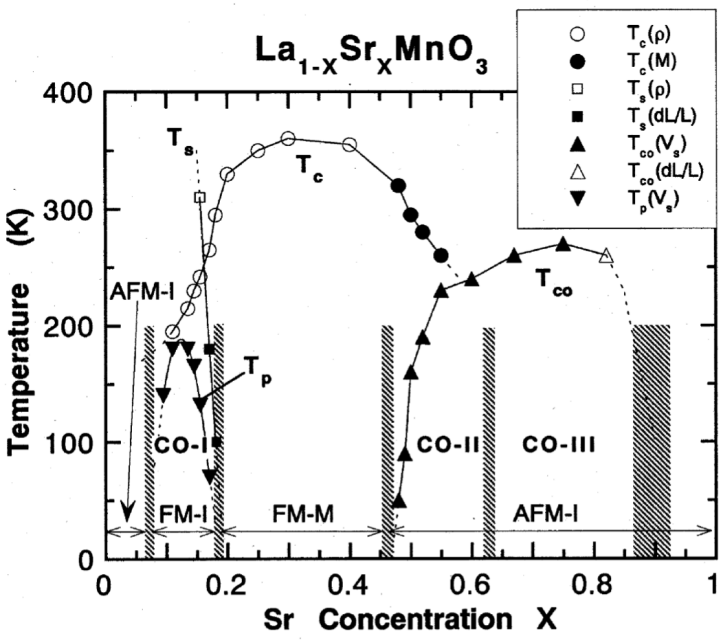

Figure 2.2: Phase diagram of $La_{1-x}Sr_xMnO_3$ as a function of temperature and doping x. AFM-I: antiferromagnetic insulator; FM-I: ferromagnetic insulator; FM-M: ferromagnetic metal; CO: three types of charge ordering states; T_C: Curie temperature; T_N: *Néel* temperature; T_p: polaron ordering temperature; T_S: structure transition temperature; T_{CO}: charge ordering transition temperature. Adapted from ref. [115].

To summarize, a quick introduction is given about the basic information of multiferroic $BiFeO_3$ and ferromagnet $La_{0.7}Sr_{0.3}MnO_3$ in this section. In both materials, the charge, spin, orbital and lattice degrees of freedom are fundamentally important for determining the intrinsic properties. Thus the interplay between these degrees of freedom across the interface would definitely be a great model system to explore and understand the rich physics involved at the heterointerface. This is a big challenge, while it also provides great opportunities to obtain novel phenomena and functionalities.

2.2 Fabrication of BFO/LSMO heterostructures

This section is dedicated to the growth of high-quality heterostructures used for the study of this dissertation. Figure 2.3 shows a simple schematic of the growth setup, which consists of a pulsed-laser deposition (PLD) chamber and a high pressure reflection high-energy electron diffraction (RHEED) system. During the growth, we use a target with the same composition as the material that we want to grow, and bombard it with high power pulsed-laser. The material is then vaporized from the target and deposited on the substrate prepared. [116, 117] RHEED is employed as an in-situ tool to characterize the surface structure of the material. High energy electrons with energy range of 20 keV was used to strike the sample surface at a grazing angle of 1 to 5°. Due to the strong scattering between the incident electrons and the material, the probing depth is only the first few atomic layers of the material, thus making RHEED study an extremely surface sensitive technique. [118]

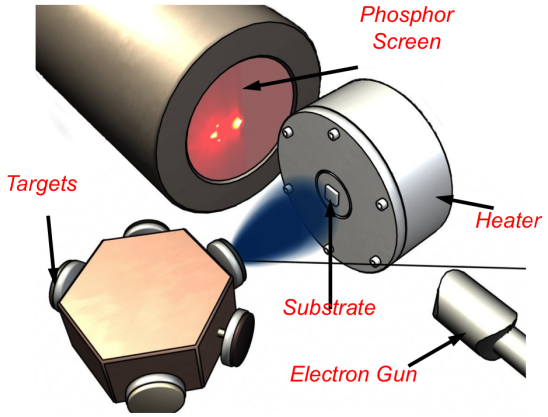

Figure 2.3: Schematic illustration of a pulsed-laser deposition system assisted with reflection high energy electron diffraction.

For all heterostructures studied in this dissertation, $SrTiO_3$ (STO) (001) single crystal is employed as the substrate, which can provide good lattice match for various perovskite materials used. Before the growth, a buffered HF acid-etch and thermal treatment process [119] was used to obtain fully TiO_2 (B site)-terminated surface on STO. This is supported by atomic force microscopy (AFM) measurements, showing perfect surface steps and terraces with step height of one unit-cell, as shown in Figure 2.4a. It is worth pointing out that such a singly terminated surface is fundamentally important for the heterointerface design as carried out in this study. Figure 2.4b shows a RHEED pattern obtained from the treated STO substrate, which consists of the information of both surface diffraction and reflection. The diffraction pattern, as a result of the electron interference from various atoms at the sample surface, can provide the first-hand information about the surface construction, lattice

symmetry, phase transition and strain relaxation. While the reflection pattern (also called specular pattern) can be used to characterize the surface morphology during the growth. [118]

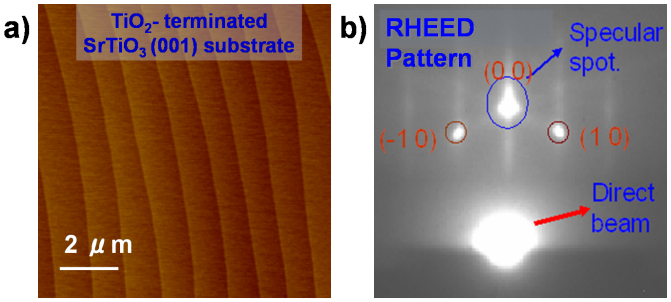

Figure 2.4: Topography of a treated $SrTiO_3$ substrate (a) and corresponding RHEED pattern (b).

To achieve the atomic scale control of the materials, a layer-by-layer (LBL) growth mode is desired. In LBL growth mode (also called Frank-Van der Merwe growth), atoms grow first in two dimensional to complete the atomic surface of the film prior to the growth of subsequent layers. Thus such growth mode usually can result in atomically smooth, fully covered atomic layers. Figure 2.5 shows a schematic of specular RHEED intensity during a typical LBL growth. At the initial stage of the growth, the RHEED specular spot intensity decreases as more atoms deposited on the sample and resulting in a rougher surface. And eventually the intensity reaches minimum for half-covered case. After that, the intensity recovers during the growth and shows a maximum again when the surface layer is fully-completed and becomes smooth again. Therefore, by monitoring the intensity oscillation in a periodic manner, one can monitor and control *in-situ* the thickness of materials during the LBL growth. [118]

Figure 2.6 shows RHEED specular intensity profiles recorded during the growth of LSMO and BFO layers on TiO_2-terminated STO substrate, respectively. For LSMO layer, clear RHEED oscillations can be observed throughout the growth, which indicates a well-controlled LBL growth mode and is consistent with the surface topography taken by atomic force microscopy (AFM). For the growth of BFO layer, a transition from layer-by-layer growth to step-flow growth was observed during the initial growth of BFO, which was supported by the continuous presence of the two dimensional spots in the corresponding RHEED patterns as well as the atomic terrace of the surface topography (shown in the inset). Thus, we have demonstrated a well-controlled growth mode for high-quality BFO/LSMO heterostructures.

Finally, it is worth noting that the LBL growth mode occurs when the total free energy of the film surface and the interface equals to the free energy of the substrate surface, thus it requires well-controlled and optimized growth parameters, such as heater temperature, background oxygen pressure and growth rate. Table 2.1 itemizes

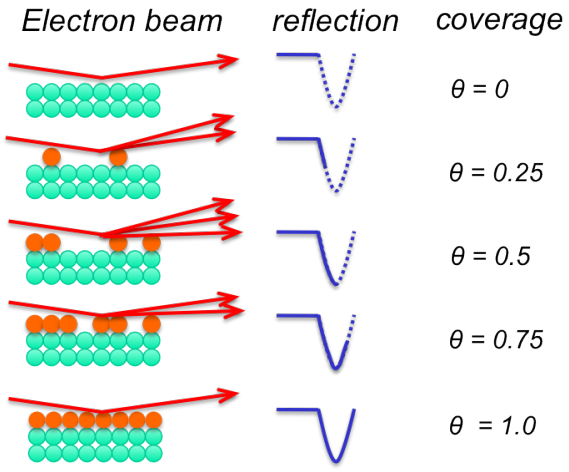

Figure 2.5: A schematic of specular RHEED intensity oscillations during the layer-by-layer growth.

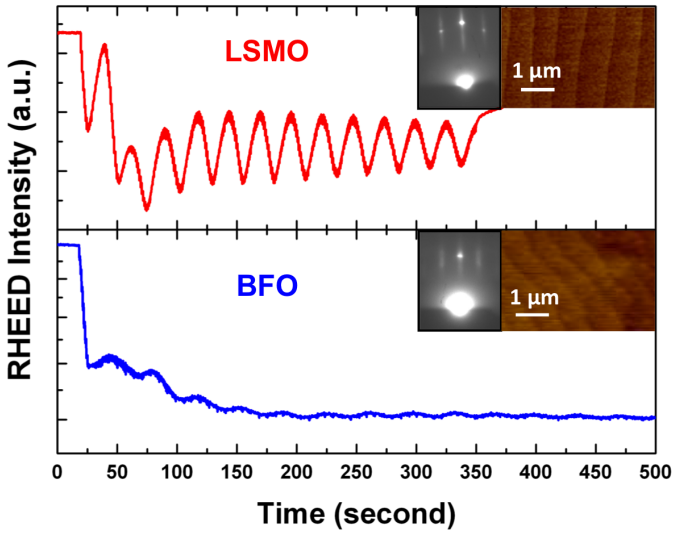

Figure 2.6: RHEED assisted PLD growth of BFO/LSMO heterostructures on STO (001) substrates. RHEED patterns and AFM images for corresponding LSMO and BFO layers are shown in the insets.

the optimized PLD growth conditions for various oxide materials with LBL (or step flow) growth mode, which are used throughout this dissertation. Clear intensity oscillations (Figure 2.7) suggest that the LBL growth mode persists for all materials used, which makes the atomic-scale control of the heterointerface possible, therefore providing a solid platform for the current study.

Material	Temperature (°C)	Pressure (mTorr)	Laser energy density (J/cm^2)	Growth rate (mono-layer/pulse)
$La_{0.7}Sr_{0.3}MnO_3$	690	150	1.5	0.04
$BiFeO_3$	690	150	1.5	0.03
$SrRuO_3$	650	100	1.5	0.04
SrO	500	1	1.5	0.015
TiO_2	700	10	1.5	0.05
$PbZr_{0.2}Ti_{0.8}O_3$	630	100	1.5	0.05

Table 2.1: Optimized PLD growth conditions for various oxide materials with layer by layer growth mode.

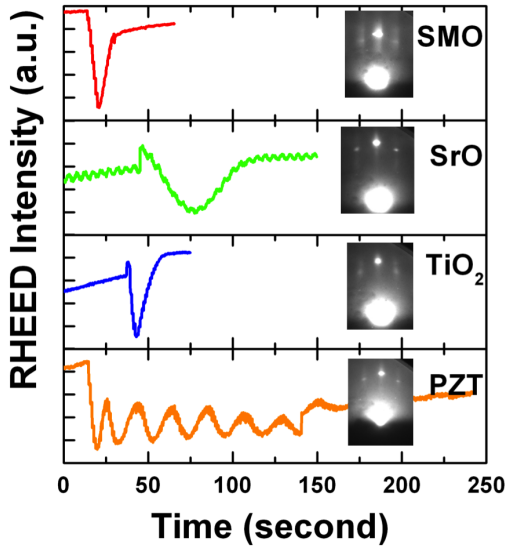

Figure 2.7: RHEED patterns and specular RHEED intensity oscillations monitored during the growth of various oxide materials.

2.3 Characterization of BFO/LSMO heterostructures

This section presents characterizations of BFO and LSMO thin films fabricated as described in the previous section with various experimental setups. The measurements suggest that thin films possess excellent structure, magnetic, electrical, and ferroelectric properties, thus providing a solid platform for subsequent studies.

2.3.1 Structure characterization of BFO/LSMO heterostructures

Structural characterizations of BFO/LSMO heterostructures were carried out with both x-ray diffraction (XRD) (Figure 2.8a) and reciprocal space mapping (RSM) (Figure 2.8b). XRD measurements (Figure 2.8a) reveal that the BFO layer is pure phase and in-plane strained to the STO substrate. The presence of Kiessig fringes along of both the (001) and (002) BFO diffraction peaks indicates a highly ordered crystalline structure of the sample, suggesting both high-quality interface and surface structures. The mosaic structure of the BFO layer was also investigated with the rocking curve scan around BFO (002) Bragg peak. The full width at half maximum (FWHM) of the rocking curve scan obtained is about 0.06°, which is close to that of the substrate use (∼0.03°), implying a good crystallinity of the BFO thin film. The RSM scans further suggest that the BFO layer is fully strained to STO substrate, with in-plane lattice constant equal to that of the substrate. We note that the out-of-plane lattice constant of 4.07 Å from RSM scans is also consistent with XRD measurements. [120]

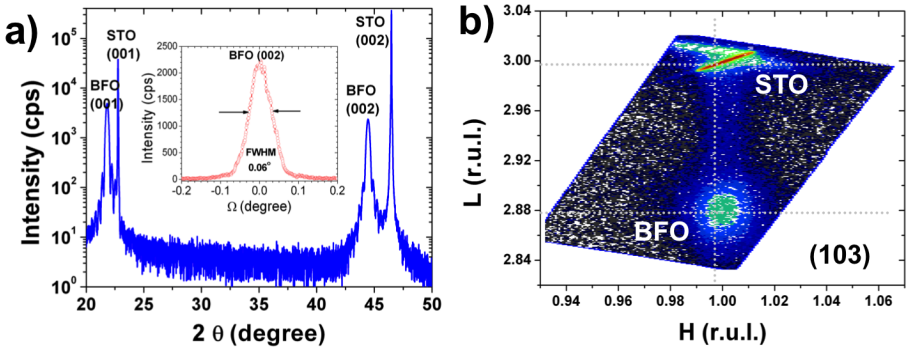

Figure 2.8: Structure characterization of BFO/LSMO heterostructures. (a) X-ray diffraction analysis of a BFO (30 nm)/LSMO (5 nm) heterostructure grown on STO (001) substrate. (b) Reciprocal space mapping of the heterostructure along the (103) zone axis of STO substrate. We note that the LSMO layer is not visible from this study, mainly because its thickness is only 5 nm.

2.3.2 Magnetic and electrical properties of LSMO thin films

a. Magnetic properties of LSMO thin film

Using optimized growth conditions described above, we have been able to fabricate the LSMO layer on STO substrate with the unit-cell control. Magnetic properties of ultrathin LSMO films with thickness ranging from 3 to 90 unit-cells were measured

with Quantum Design MPMS magnetometer and are shown in Figure 2.9. For the thickness above 13 unit-cells, the saturation magnetization and the Curie temperature are nearly constant, with values close to those of previous reports of high-quality LSMO thin films [121]. However, below the thickness of 7 unit-cells, a dramatic reduction in the saturation magnetization as well as the Curie temperature can be observed, and eventually the ferromagnetism is disappeared at the thickness of 3 unit-cells. Thus, throughout this study, LSMO samples with thickness above 7 unit-cells were used in order to decouple the influence of the LSMO size effect on the interfacial magnetic coupling with multiferroic BFO.

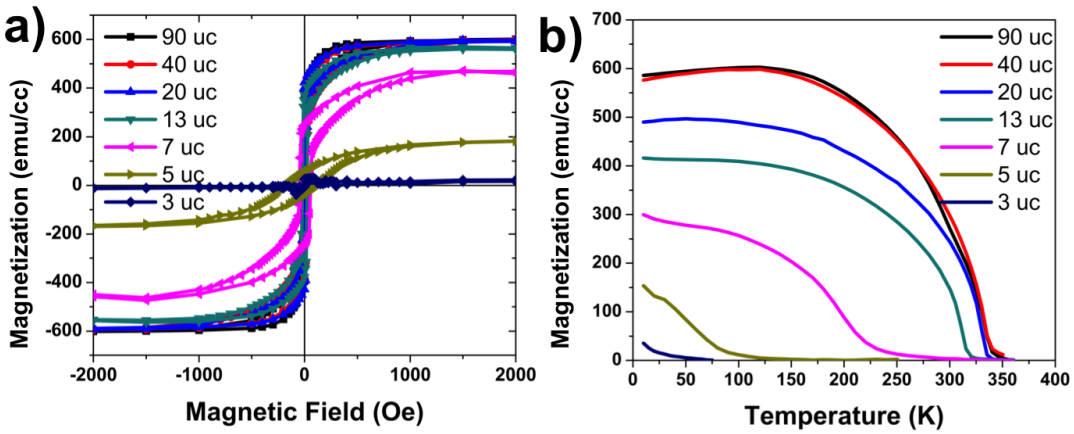

Figure 2.9: Thickness dependence of the magnetic properties of ultrathin LSMO films grown on $SrTiO_3$ (001) substrates. (a) Magnetic hysteresis loops measured at 10 K. (b) Temperature dependence of the magnetization measured with 1000 Oe magnetic field.

b. Electrical transport properties of LSMO thin film

The temperature dependence of the resistivity of ultrathin LSMO films with variable thickness between 3 and 70 unit-cells was also measured and is given in Figure 2.10. [121] Thicker films show a bulk-like metallic behavior over the whole temperature regime, and the residual resistivity of 60-80 $\mu\Omega$cm at 10 K is consistent with previous reports. [122] When the LSMO layer thickness decreases, the resistivity increases quite drastically over the whole temperature range. For LSMO layers with thicknesses of eight unit-cells and below, we observed a dramatic increase of resistivity as the temperature decreases, indicating that the films are insulating below this critical thickness. Surprisingly, the critical thickness of the conductivity behavior is much larger than that of the magnetic ordering. This discrepancy can be explained by the possible loss of a conducting percolation path due to the formation of ferromagnetic/metallic and non-ferromagnetic/non-metallic regions. Interestingly, our

recent study reveals that the LSMO layer in BFO/LSMO heterostructures remains metallic down to the thickness of 7 unit-cells (shown in chapter 6), which points to the important role of interface reconstructions on the macroscopic properties of materials.

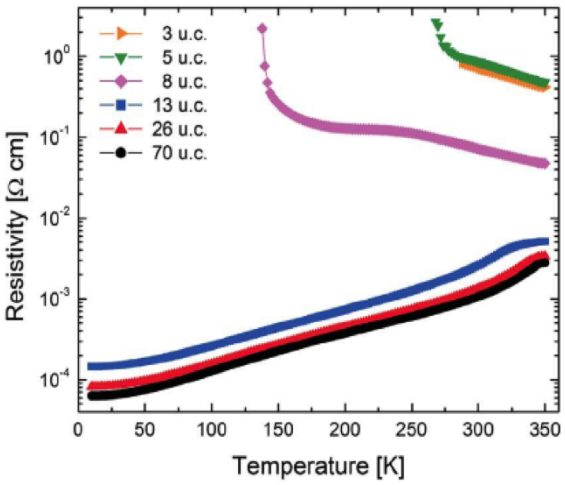

Figure 2.10: Temperature dependence of electrical transport measurements on ultrathin LSMO films with various thicknesses grown on $SrTiO_3$ (001) substrates. Adapted from ref. [121].

2.3.3 Ferroelectric properties of BFO thin films

a. Ferroelectric domain structure of BFO thin films

Since BFO has a rhombohedral perovskite structure, the ferroelectric polarization occurs along the body diagonal of the cubic lattice ¡111¿, leading to totally eight possible polarization variants as shown in Figure 2.11a. To map the ferroelectric polarizations of all these eight variants, piezoresponse force microscopy (PFM) was employed, which simultaneously records the out-of-plane (OP) and in-plane (IP) piezoresponse signals. [123] During the scan, ac bias of $3.0V_{pp}$ at 6.39 kHz is applied to the conducting probe, which scans along the [1-10] direction. Due to the interaction between the ferroelectric polarization and the biased atomic force microscopy (AFM) tip, three IP contrasts and two OP contrasts could be revealed, as shown in Figure 2.11a, which can help to map the ferroelectric polarization distribution. It is worth noting that polarizations P_2^- and P_4^- (or P_2^+ and P_4^+) are degenerate for the scan, and a 90° rotation of the sample is required to separate them. Figure 2.11b shows the IP and OP ferroelectric domain structure of BFO (100 nm) /LSMO (5 nm) thin films. The PFM IP image indicates the presence of stripe-like ferroelectric domain

structure (separated by 71° domain walls) in the BFO layer, and the polarization was switchable and stable (shown in the inset of Figure 2.11b). [124]

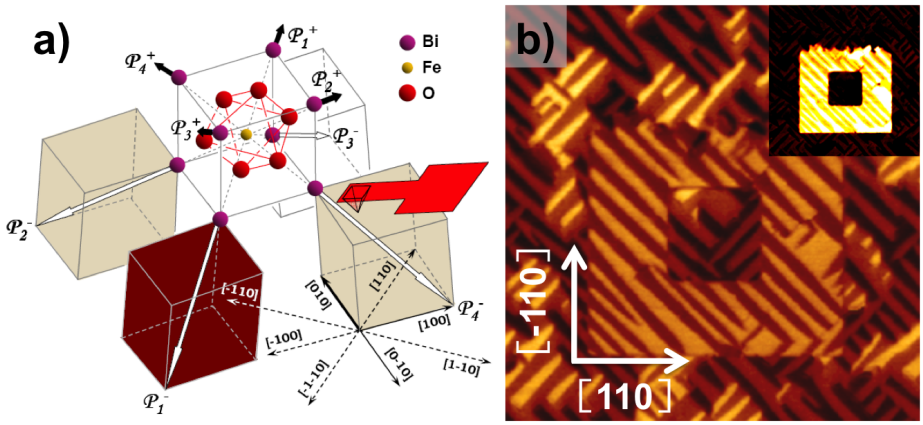

Figure 2.11: Ferroelectric domain structure of BFO thin film. (a) A schematic of eight possible polarization variants in (001) rhombohedral films. The AFM cantilever is oriented along [1-10] direction. (b) In-plane and out-of-plane (shown in the inset) ferroelectric domain structures of BFO/LSMO thin films.

b. Ferroelectric polarization hysteresis loop of BFO thin films

The ferroelectric polarization hysteresis loop of BFO thin films was measured with Radiant Technologies Inc. RT6000S ferroelectric tester probe station, and is shown in Figure 2.12. Thin film heterostructures of 100 nm BFO and 20 nm SRO bottom electrode were used in this study, which exhibit similar domain structure as shown in Figure 2.12b. SRO top electrodes (with the diameter of 32 μm) were used in this study to diminish the internal field of the heterostructure due to the electrostatic mismatch between the top and bottom electrodes. To make a low resistance contact, 150 nm of platinum was later sputtered on SRO top electrodes. The ferroelectric nature of thin films is demonstrated in Figure 2.12, which shows a sharp and square hysteresis, with the $2P_r$ value of 120-130 $\mu C/cm^2$, consistent with the previously theoretical [125] and experimental [126] reports.

c. Piezoresponse of BFO thin films

Piezoelectric properties of BFO thin films were measured with the PFM setup using the AFM tip as the top contact, which measures the tip displacement as a function of the applied electrical bias. The piezoresponse coefficient d_{33} was obtained with the reference of standard samples, and is shown in Figure 2.13a. For samples with thickness larger than 30 nm, the measured remnant d_{33} value of 60-70 pmV^{-1} is consistent with previous reports on high-quality BFO thin films. [124] However,

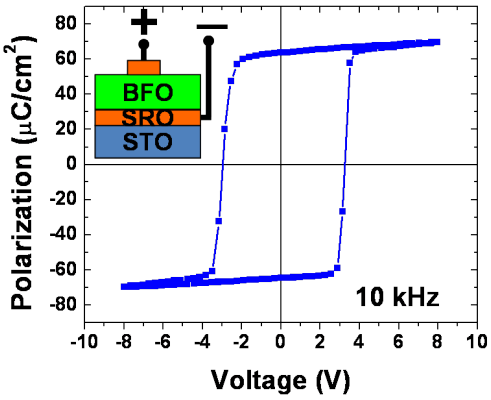

Figure 2.12: Ferroelectric polarization hysteresis loop of BFO thin films.

we observed a dramatic reduction of the piezoresponse for thickness below that. For comparison, we observed a d_{33} of about 10 pmV^{-1} on 4 nm BFO, which is about six times smaller than that of thicker films. Since the ferroelectric and antiferromagnetic orderings in BFO are strongly coupled together, a similar thickness dependence of the antiferromagnetic structure in BFO is also expected. Therefore, we limit the BFO thickness to be above 30 nm in the subsequent study in order to decouple the influence of the BFO size effect on the electrical and magnetic coupling across BFO/LSMO heterointerfaces.

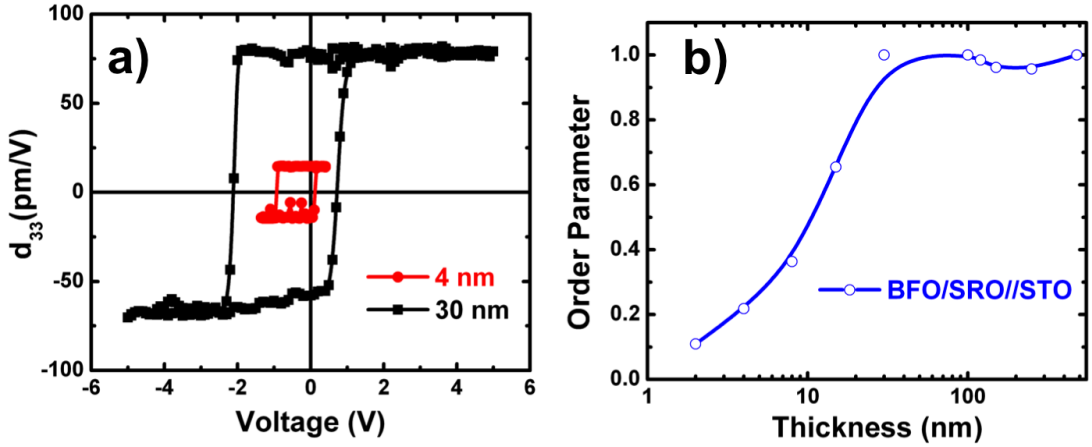

Figure 2.13: Thickness dependence of piezoelectric properties of BFO thin films. (a) Ferroelastic hysteresis loops of BFO/SRO thin films with 30 nm and 4 nm of BFO layer. (b) Normalized ferroelectric order parameter for BFO/SRO thin films as a function of BFO thickness.

Chapter 3

Interface control of bulk ferroelectric polarization

The control of material interfaces at the atomic level has led to novel interfacial properties and functionalities. In particular, the study of polar discontinuities at interfaces between complex oxides lies at the frontier of modern condensed matter research. In this chapter, we employ a combination of experimental measurements and theoretical calculations to demonstrate control of a bulk property, namely ferroelectric polarization, of a heteroepitaxial bilayer by precise atomic-scale interface engineering. More specifically, the control is achieved by exploiting the interfacial valence mismatch (polar discontinuity) to influence the electrostatic potential step across the interface, which manifests itself as the internal field in ferroelectric hysteresis loops, thus determining the ferroelectric state. A broad study of diverse systems comprising different ferroelectrics and conducting perovskite underlayers extends the generality of this phenomenon. [127]

3.1 Motivation

Over the past few years, precisely constructed, atomically sharp perovskite oxides heterointerfaces have attracted considerable attention. [13,128] The incorporation and reconstruction of spin [15, 56], charge [6, 7, 129] and orbital degrees [53, 130] of freedom across heterointerfaces has led to novel electronic properties, which are different from those inherent to the individual components. For example, pioneering work on the $LaAlO_3$ (LAO) and $SrTiO_3$ (STO) heterostructure has revealed a nontrivial and potentially useful high mobility two-dimensional electron gas (2DEG) at the interface [7], which also exhibits magnetic [40] and even superconducting [41] properties, as a consequence of the so-called "polar discontinuity" [35] (valence mismatch) across the interface.

Triggered by this innovative work, much of the current research is focused on prob-

ing the novel interfacial phenomena with various heterointerfaces. However, what is missing in a focused study of interfacial properties are the more macroscopic implications of this atomic-scale control on the broad range of properties and order parameters present in complex oxides. As techniques have allowed us to peer ever deeper into materials, at finer and finer length scales, we have not successfully answer a simple question: is it possible to use interfacial structure to control the bulk phase state of a material away from the interface? Such an approach could be particularly intriguing if one of the layers is highly polar and electrically switchable, i.e. ferroelectric in nature . In this chapter we report the ability to deterministically control ferroelectric order in materials through atomic-scale control of interfacial electronic structure. Our results suggest a strong, delocalized effect with important implications for future electronics based on such materials.

We begin by exploring the ferroelectric perovskite $BiFeO_3$ (BFO) in intimate contact with a conducting manganite $La_{0.7}Sr_{0.3}MnO_3$ (LSMO) as our model interface. Through the use of reflection high-energy electron diffraction (RHEED)-assisted pulsed-laser deposition (PLD), high-quality heterostructures of BFO/LSMO were synthesized. We have observed that the interface between BFO and LSMO can be precisely engineered with near atomic-scale sharpness. Subsequent investigations of ferroelectric order indicate that the as-grown polarization direction is strongly correlated to the interface termination and its fine level control of the interface electronic structure.

3.2 Control of heterointerfaces by epitaxial design

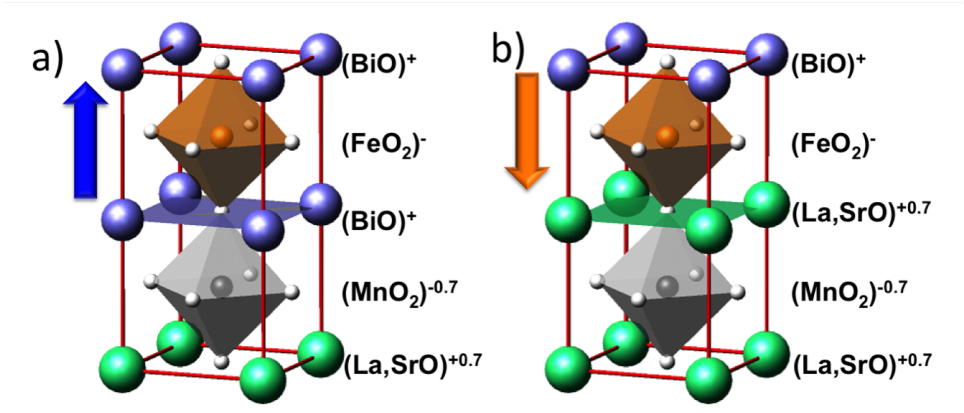

Figure 3.1: Schematics of atomic stacking sequence for the $BiFeO_3$/ $La_{0.7}Sr_{0.3}MnO_3$ heterostructure with $La_{0.7}Sr_{0.3}O$-MnO_2-BiO-FeO_2 (a) and MnO_2-$La_{0.7}Sr_{0.3}O$-FeO_2-BiO (b) heterointerface. The sheet charge density for each layer has been assigned the nominal bulk valence. The arrows indicate the as-grown directions of the ferroelectric polarizations in BFO layers.

The key to controlling the ferroelectric polarization in the BFO layer lies in the ABO_3 perovskite structure exhibited by both LSMO and BFO, which enables two different kinds of interfaces to be created in [001]-oriented heterostructures. Along the [001], the perovskite structure is made up of alternating layers of AO and BO_2. Thus if the LSMO is terminated at the MnO_2-plane at the interface we can effectively create an interface with the stacking sequence of $La_{0.7}Sr_{0.3}O$-(MnO_2)-BiO-FeO_2 (MnO_2-terminated interface) (Figure 3.1a). On the other hand, if the LSMO layer is terminated at the $La_{0.7}Sr_{0.3}O$-plane, the stacking sequence changes to MnO_2-($La_{0.7}Sr_{0.3}O$)-FeO_2-BiO ($La_{0.7}Sr_{0.3}O$-terminated interface) (Figure 3.1b).

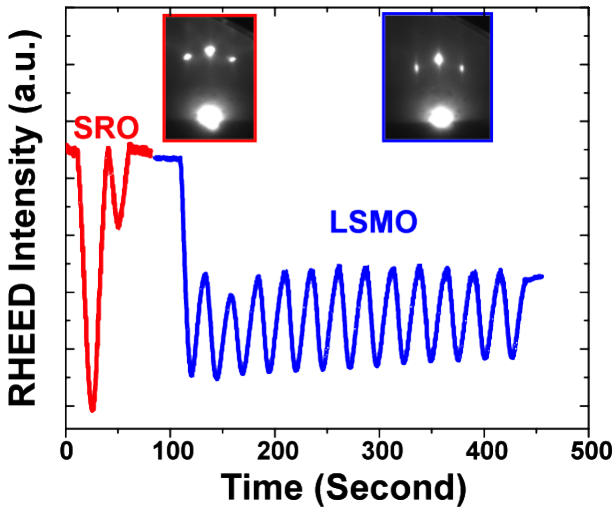

Figure 3.2: RHEED intensity oscillations of the specular reflected beam during the growth of $SrRuO_3$ and $La_{0.7}Sr_{0.3}MnO_3$ on the TiO_2 terminated $SrTiO_3$ (001) surface. Clear intensity oscillations of the specular reflection spot during the growth indicates a layer-by-layer growth mode. The changing of RHEED oscillation period during the growth of SRO indicates the changing of termination from TiO_2 (B site) to SrO (A site) termination.

Our design philosophy starts from building LSMO with two different terminations, MnO_2 and $La_{0.7}Sr_{0.3}O$ terminations respectively, by utilizing TiO_2-terminated STO (001) substrates obtained with etch/thermal anneal procedures. [119] The MnO_2-terminated LSMO was grown by direct, RHEED-controlled deposition of 13 unit-cells of LSMO on the TiO_2-terminated STO substrate. During the growth of LSMO, clear intensity oscillations of the specular reflection spot can be observed (Figure 3.2) indicating a layer-by-layer growth mode with the controlled smooth surface without any island formation, allowing us to create atomically-precise structures. For the $La_{0.7}Sr_{0.3}O$-terminated LSMO film, we first grew a very thin layer (2.5 unit-cells) of $SrRuO_3$ on STO, which effectively changes the termination of STO to SrO-terminated surface since the RuO_2-layer is highly volatile. [131] During the growth of SRO, the

changing of RHEED oscillation period clearly indicates the change of film termination from TiO_2 (B site) termination to SrO (A site) termination. Subsequent deposition of 13 unit-cells of LSMO on this surface results in a $La_{0.7}Sr_{0.3}O$-terminated layer.

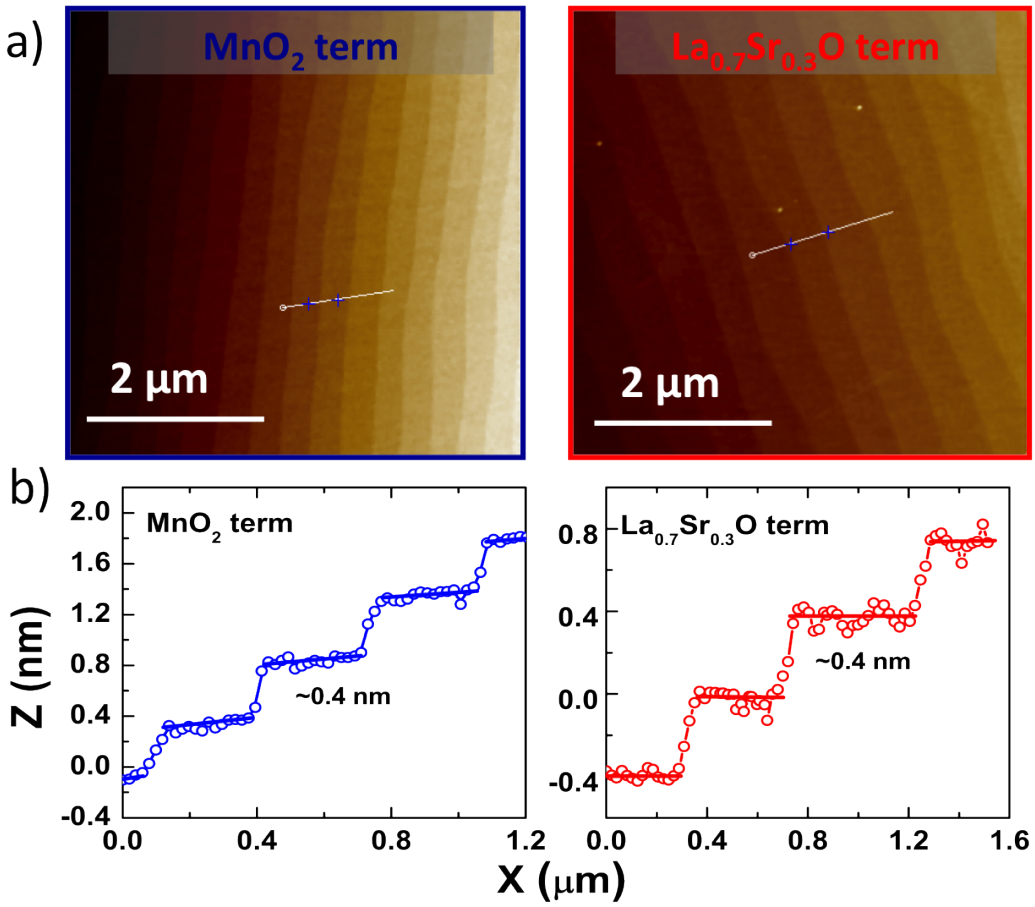

Figure 3.3: Topography of LSMO thin films with nominal $La_{0.7}Sr_{0.3}O$ and MnO_2 terminations. (a) Atomic force microscopy images of MnO_2 (left) and $La_{0.7}Sr_{0.3}O$ (right) terminated LSMO. (b) Line-scans of the AFM images showing atomically flat terraces with the step height of $\sim$ 0.4 nm (the lattice constant of one perovskite unit cell).

Atomic force microscopy (AFM) measurements were further used to probe the nature of the surface of LSMO thin films with nominal $La_{0.7}Sr_{0.3}O$ and MnO_2 terminations following growth, as shown in Fig. 3.3. The morphology of the films grown via the layer-by-layer process in both cases (Figure 3.2) is very smooth and shows the presence of atomically flat terraces as defined by the underlying vicinal substrate and separated by steps of height $\sim$ 0.4 nm (one unit cell). This confirms that each as-grown thin film has only one single termination.

In order to further confirm that our carefully-controlled growth protocol indeed leads to different terminations of LSMO layers, time-of-flight ion scattering and recoil

spectroscopy (TOF-ISARS) was used to characterize surface chemistries. [132] TOF-ISARS is a non-destructive, real-time probe, capable of providing direct information on surface composition and atomic structure of the first few monolayers. [133, 134] During measurements, pulsed potassium ions are accelerated to 10 keV and injected towards the film surface to produce recoiled ions from the sample at an incident angle of 5° and the MSRI are measured at a recoiling angle of 60°. As the consequence of the direct and strong collision between the incoming ions and the surface, the elements at the topmost surface will be decomposed to form charged ions. The created ion beam then travels through the acceleration zone with an applied electric field, with the final velocity of the ions depending on the mass-to-charge ratio. Finally, a constant electrostatic field is applied inside the reflection zone to bend the traveling path of the ion beam toward the detector. Thus, by measuring the time needed for the ions to reach the detector, the mass-to-charge ratio of the ions could be determined. Due to the limited penetration depth of the low-energy K ions, different surface sensitive probe could be achieved by choosing different incident angle of the ion beam. For small grazing incidence angles ($\sim 5°$), this technique is extremely surface sensitive and yields dramatically different signal intensity between compositions of the first and the second monolayer.

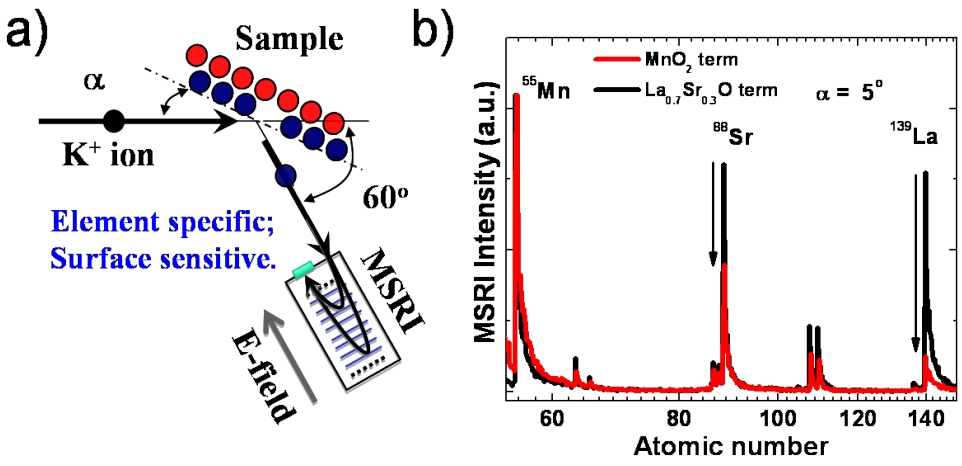

Figure 3.4: Comparison of TOF-ISARS spectra for $La_{0.7}Sr_{0.3}MnO_3$ thin films with MnO_2 and $La_{0.7}Sr_{0.3}O$ termination. The small peaks around an atomic number of 108 correspond to silver isotopes stemming from the silver paint used for the samples attachment to the heater block and does not affect the conclusion about the surface termination.

In this measurement, two LSMO samples with MnO_2- and $La_{0.7}Sr_{0.3}O$-terminated layers were prepared by the process described above and then transferred to the TOF-ISARS chamber, which has the base pressure of 10^{-8} Torr. Prior to the measurement, the samples were heated to 650 °C in an oxygen pressure of 100 mTorr for 1 hour to remove any hydrocarbon contaminates and organic residue from the surface. The

measurements were carried out at room temperature after this thermal annealing process.

Figure 3.4b shows the mass spectroscopy of recoiled ions (MSRI), normalized to the ^{55}Mn peak, for the two different surface terminations. The results reveal that the LSMO films grown on thin SRO buffer layers exhibit strongly enhanced La- and Sr-peak intensity, consistent with $La_{0.7}Sr_{0.3}O$-layer termination. In contrast, the LSMO films grown directly on the TiO_2-terminated STO substrates show relatively lower intensities of the La- and Sr-peaks suggesting MnO_2-layer termination. These results together with the AFM images (Figure 3.3, which shows the presence of atomically flat terraces as defined by the underlying vicinal substrate and separated by steps of height ~ 0.4 nm), indicate that we can indeed control the overall surface termination of the LSMO layer through the growth protocol described above.

Thus, we have shown that by using epitaxial growth, the LSMO thin films with two different termination layers could be achieved. Subsequent deposition of BFO layer on top of them will result in the BFO/LSMO heterostructures with two different interface configurations as shown in Figure 3.1.

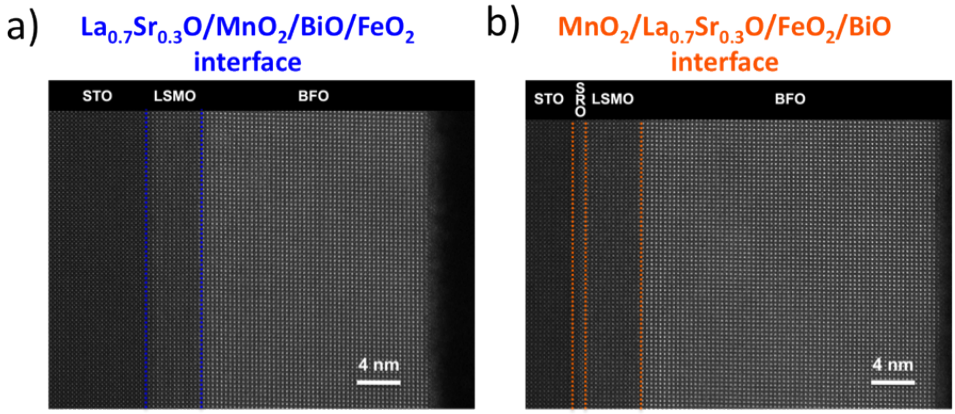

Figure 3.5: Layer architecture of BFO/LSMO heterostructures with different terminations. (a) The sample with $La_{0.7}Sr_{0.3}O$-MnO_2-BiO-FeO_2 (MnO_2 terminated interface) is designed by growing integral unit LSMO/BFO directly on STO substrates. (b) While for the sample with MnO_2-$La_{0.7}Sr_{0.3}O$-FeO_2-BiO ($La_{0.7}Sr_{0.3}O$ terminated interface, 2.5 unit-cells $SrRuO_3$ buffered STO was used.

To confirm the atomic stacking sequence of BFO/LSMO heterointerfaces, scanning transmission electron microscopy (STEM) was carried out to probe the local atomic structure of the samples. [135] Figures 3.5a and b show the low resolution cross section STEM images of the layer architecture of samples with both $La_{0.7}Sr_{0.3}O$-MnO_2-BiO-FeO_2 (MnO_2 terminated interface) and MnO_2-$La_{0.7}Sr_{0.3}O$-FeO_2-BiO ($La_{0.7}Sr_{0.3}O$ terminated interface) atomic stacking sequences. For both structures, the growth direction is from left to right. The MnO_2 terminated interface consists of a BFO/LSMO

bilayer grown on a STO substrate (Figure 3.5a). The LSMO layer is 13 nominal unit-cells thick and the BFO layer is $\sim$ 21 nm thick. Similarly, the $La_{0.7}Sr_{0.3}O$ terminated interface consists of a heterostructure of SRO, LSMO and BFO grown on a STO substrate (Figure 3.5b). The nominal layer thickness is 2.5 unit cells for SRO, 13 unit cells for LSMO and $\sim$ 27 nm for BFO.

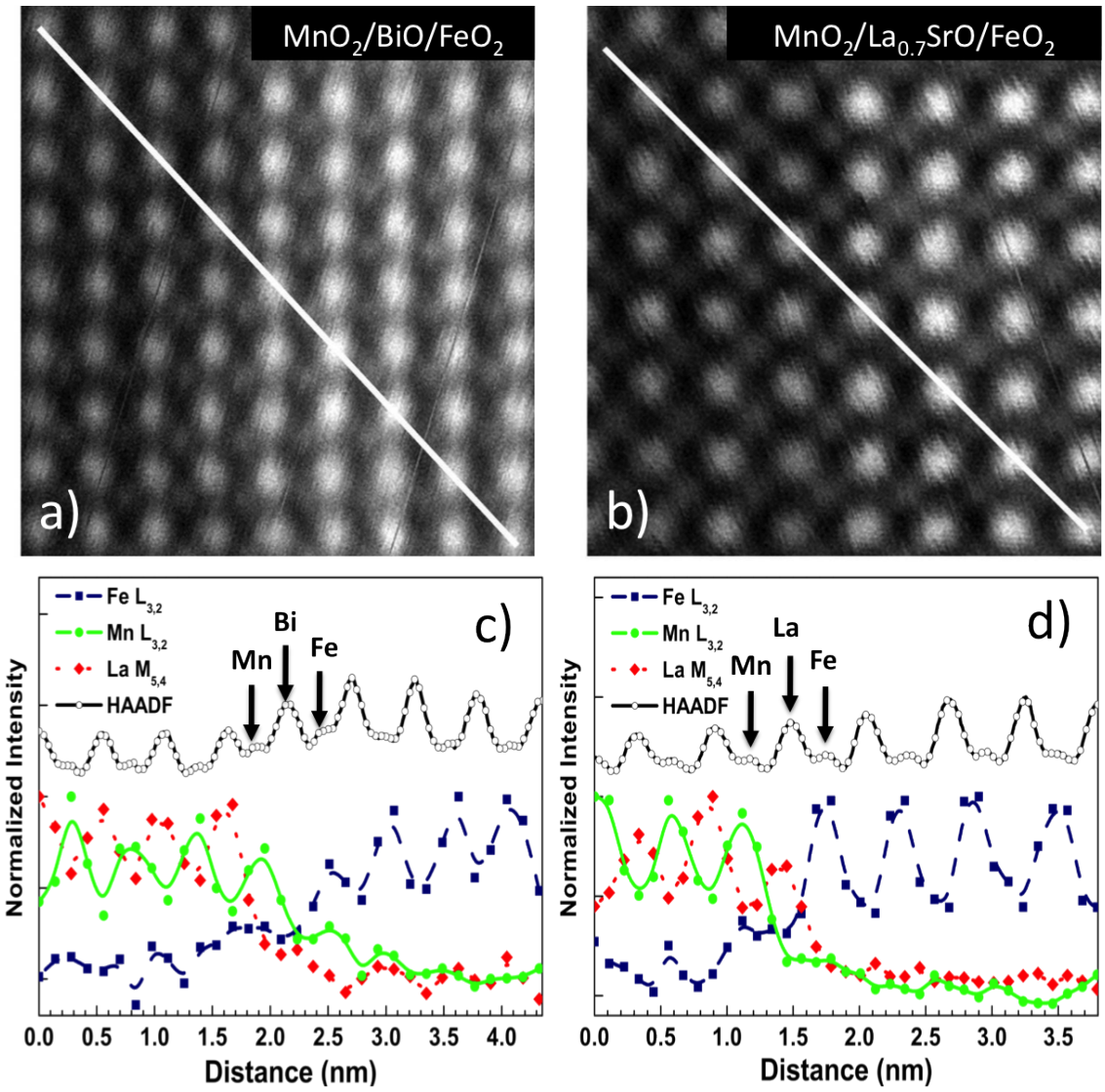

Figure 3.6: Atomic scale structure and chemical characterization of BFO/LSMO with different interfaces. High-resolution HAADF-STEM images of the heterostructures with $La_{0.7}Sr_{0.3}O$-MnO_2-BiO-FeO_2 (a) and MnO_2-$La_{0.7}Sr_{0.3}O$-FeO_2-BiO (b) interfaces. Corresponding chemical profiles across the $La_{0.7}Sr_{0.3}O$-MnO_2-BiO-FeO_2 (c) and MnO_2-$La_{0.7}Sr_{0.3}O$-FeO_2-BiO interfaces (d). The EELS line scans were acquired diagonally from the top left to the bottom right of the HAADF image (indicated with a white line).

Further information regarding interface atomic stacking sequences can be gained through the detailed high-resolution STEM imaging and analysis. In particular, atomic-scale EELS studies (Figure 3.6) have been carried out to confirm and complement the macroscopic TOF-ISARS measurements of surface/interface structure and chemistry. The cross-section high resolution STEM images show the layer architecture of the heterostructures and suggest atomically-abrupt, highly-controlled epitaxial interfaces between the LSMO and the BFO layers (Figures 3.6a and b). As imaging alone cannot rule out cation diffusion, more than twenty EELS line-scans were acquired across both LSMO/BFO interfaces at different locations. Figure 3.6c depicts the integrated EELS signals of the Fe $L_{3,2}$, Mn $L_{3,2}$ and La $M_{5,4}$ absorption edges, simultaneously recorded along a line as displayed in the corresponding STEM images (Figures 3.6a and b). The characteristics of the Fe, Mn, and the La signals reflect the expected atomic structure within the LSMO and the BFO layers and the modulations of the individual EELS signals at the interface suggest abrupt chemical profiles at the interface. Combining the information from EELS studies, high angle annular dark field (HAADF) intensity profiles, and HAADF-STEM images, the interface atomic configurations can be deduced to be $La_{0.7}Sr_{0.3}O$-MnO_2-BiO-FeO_2 and MnO_2-$La_{0.7}Sr_{0.3}O$-FeO_2-BiO (Figures 3.1a and b, respectively). Thus, the interface between BFO/LSMO in such artificial heterostructures can be engineered to exhibit two different interface terminations, which provides a solid platform to trigger the study of novel coupling phenomena at the oxide interfaces.

3.3 Interface polar discontinuity control of bulk ferroelectric polarization

In this section, we proceeded to examine how these different interfacial structures designed in the previous section can impact the nature of the electronic interactions at these heterointerfaces. Piezoresponse force microscopy (PFM) was employed to study the polarization state of the BFO in the heterostructures (MnO_2- and $La_{0.7}Sr_{0.3}O$-terminated interfaces are shown in figure 3.7, respectively). [123] PFM measurements were carried out with an AFM based setup (Veeco-DI equipped with a Nanoscope IV controller) under ambient conditions using a commercially TiPt-coated Si tip (MikroMasch). The images were acquired in contact mode with a driving voltage of 3 V_{pp} at 6.39 kHz and a scanning rate of 1 $\mu m/s$. With the same setup, piezoelectric hysteresis loops were characterized by recording the surface displacement as a function of applied DC voltage (up to ± 8 V), with a driving voltage of 0.5 V_{pp} at 6.39 kHz applied to the AFM tip. During measurements, the biased electric field is applied though the AFM tip, while the samples are grounded. The contrast of the out-of-plane PFM image is correlated with the orientation of the ferroelectric polarization, with the dark (bright) indicating upward (downward) ferroelectric polarization. Strikingly, the as-grown polarization direction is directly correlated with the interface termination of

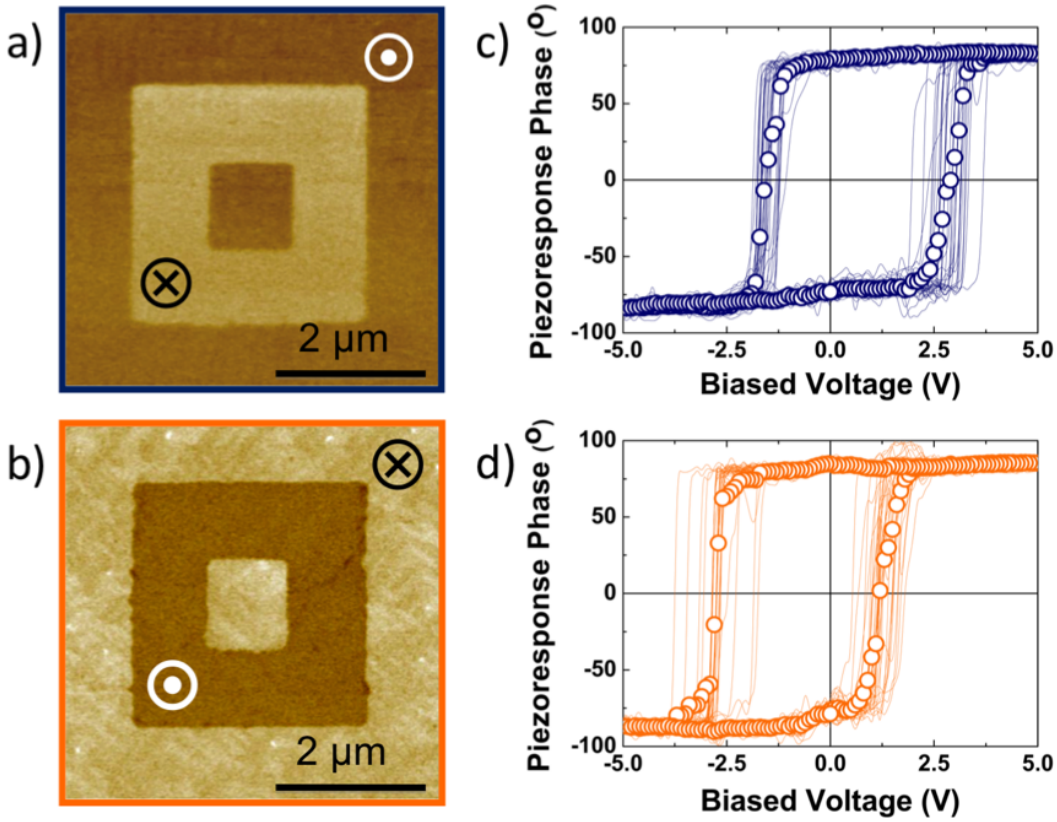

Figure 3.7: Ferroelectric polarization switching. Out-of-the plane ferroelectric polarization of as-grown BFO/LSMO heterostructure with $La_{0.7}Sr_{0.3}O$-MnO_2-BiO-FeO_2 (a) and MnO_2-$La_{0.7}Sr_{0.3}O$-FeO_2-BiO (b) interfaces, and corresponding typical local piezoelectric hysteresis loops (c, d). The samples used in the study are 75 nm BFO with 5 nm LSMO bottom electrode. External voltages of -/+ 8V have been applied through the AFM tip during the scanning to pole the ferroelectric polarization to up/down states. The shift of the loops indicates the presence of an internal field due to the electrical mismatch between the bottom (conducting layer) and top (AFM tips) electrodes. The solid circles in (c) and (d) are the average of 30 local loops.

the heterostructure. For samples possessing the MnO_2-terminated interface, the as-grown state is upward (pointing from the bottom electrode to the top surface) (Figure 3.7a). On the contrary, the as-grown state is exactly opposite (downward) for the samples possessing the $La_{0.7}Sr_{0.3}O$-terminated interface (Figure 3.7b). We have also probed the ferroelectric nature of these films via local switching studies using PFM tips. The sharp contrast between the opposite polarizations in the PFM images (Figures 3.7a and 3.7b) as well as the presence of square hysteresis loops in the local

piezoelectric (or ferroelectric) switching (Figures 3.7c and 3.7d) strongly indicates that these films are of very high-quality and possess good ferroelectric properties.

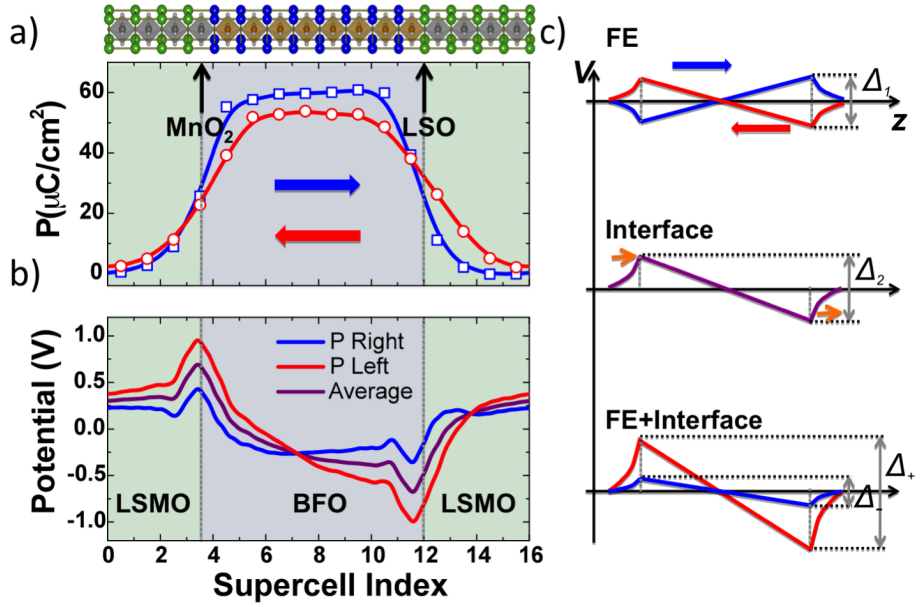

Figure 3.8: First-principles calculation and schematic illustration of electronic reconstruction across the LSMO/BFO heterointerface. (a) Calculated local ferroelectric polarization profiles through the LSMO/BFO supercell with asymmetric interface chemical compositions. A schematic of the supercell used in the study is displayed in the top panel. (b) Macroscopic average of the electrostatic potentials for the two inequivalent ferroelectric polarization directions and their average. (c) Schematic illustration of the electrostatic potential through the supercell due to the contribution of ferroelectric depolarization field (top), the asymmetric interfaces (middle) and the combination of both (bottom). The red and blue arrows indicate the ferroelectric polarization directions, while the orange arrows illustrate the interface dipole due to the valence mismatch.

To elucidate the relationship between the interface termination and ferroelectric polarization of the heterostructure, first-principles density-functional-theory (DFT) calculations [136] have been carried out. We used a supercell constructed from 8 BFO layers and 8 LSMO layers stacked along the pseudocubic [001], so that the whole supercell contains $\sqrt{2} \times \sqrt{2} \times 16$ pseudocubic perovskite units. The chemical compositions at the two interfaces in the supercell are set up to be asymmetric, i.e., one is MnO_2- and the other $La_{0.5}Sr_{0.5}O$-terminated. The in-plane lattice constant was fixed to the substrate STO lattice constant of 0.3905 nm, and the internal atomic position in the supercell were optimized.

The calculations show that the total energy of the system is lower (by 1.13 eV for the whole supercell) when the [001] component of polarization in BFO points from MnO_2- to $La_{0.5}Sr_{0.5}O$ terminated interface. The calculated preferred direction of ferroelectric polarization is consistent with the measured as-grown states of MnO_2- and $La_{0.5}Sr_{0.5}O$-terminated BFO/LSMO films. Furthermore, we have also calculated the local polarizations as a function of layer position from the relaxed supercell structures by using Born effective charges of bulk BFO obtained in a previous DFT study. [125] The calculated polarization profile is shown in Figure 3.8a. Clearly, the polarization of BFO is suppressed when it is opposite to the preferred direction, pointing to an apparently larger depolarization field in the case of opposite polarization direction compared to the preferred direction.

To trace the origin of the preference of the ferroelectric polarization, macroscopic averages of the atomic-scale electrostatic potentials across the two inequivalent interfaces have been calculated as described in Ref. [137] and are shown in Figure 3.8b. When the ferroelectric polarization is against the preferred direction ("P Left"), a large potential gradient is formed counteracting the ferroelectric polarization across the BFO layer and results in the enhancement of the depolarization field while suppressing the ferroelectric polarization (Figure 3.8a). On the contrary, the potential gradient is much reduced when the ferroelectric polarization is in the preferred direction ("P Right"), consistent with the lower total energy and preserved ferroelectric polarization in BFO.

We note that the observed potential gradient is due to the superposition of several factors, of which the two most important are illustrated in the top two panels of Figure 3.8c. The first one is the ferroelectric depolarization field. The top panel of Figure 3.8c illustrates the potential profiles from the ferroelectric depolarization field of a sandwich structure, in which a potential step (Δ_1) is built up across the ferroelectric material, with the electric field direction antiparallel to the ferroelectric polarization. The second one is the electrostatic difference between the two inequivalent interfaces, which is responsible for the observed preference of the ferroelectric polarization directions. We note that the first contribution switches sign as the polarization is reversed. Thus the average of the electrostatic potentials for two opposite polarization configurations (purple curve in Figure 3.8b) is a good estimation of the intrinsic electrostatic potential difference resulting from the interface valence mismatch, in which approximately a potential step of $\sim$1.3V forms between the two asymmetric interfaces. We note that within the framework of the so-called polar discontinuity (valence mismatch) model [7,35], the sheet charge density at the MnO_2-terminated interface (Figure 3.1a) is assigned to be +0.7e/-0.7e/+1e/-1e, which results in a nominal positive charge of +0.15e (0.7/2-0.7+1/2=0.15) at the interface, and eventually leads to an interface dipole pointing from the LSMO layer to the interface (middle panel of Figure 3.8c) due to the Thomas Fermi screening. [138, 139] Similarly, an interface dipole pointing from the interface to the LSMO layer is associated with the $La_{0.7}Sr_{0.3}O$-terminated interface due to a nominal negative interface charge of -0.15e (Figure 3.1b). As a

consequence, a potential step (Δ_2) forms across the heterostructure as shown in the middle panel of Figure 3.8c, and the sign of which is in agreement with our calculations (Figure 3.8b). Furthermore, the combination of these two mechanisms (bottom panel of Figure 3.8c) reproduces in a schematic way the DFT results (Figure 3.8b).

Experimentally, the magnitude of the interface-induced electrostatic potential step can be estimated quantitatively from the local ferroelectric hysteresis measurements (Figures. 3.7c and 3.7d). Due to the work function difference between the bottom and the top electrodes, the ferroelectric hysteresis loop is typically asymmetric about the voltage axis, with an internal field of $V_{int} = (V_+ + V)/2$ [140], where V_+ and V are the positive and negative coercive fields, respectively. Since the top electrodes (scanning probe tips coated with Ti/Pt) used for the measurements of both terminations are the same, the difference between the internal fields is taken as a measure of the induced interface electrostatic potential step. The observed difference of ∼1.2V is in excellent agreement with the results obtained by first-principles DFT calculations. This finding is also in line with the recent studies of the STO and LSMO heterointerface, in which a potential step is formed across the interface due to the valence mismatch. [138,139,141]

Structure	Electrode Termination	Polar Discontinuity	Polarization State	Internal Field (V)	Induced Field (V)
BFO/LSMO	A site	-0.3	Down	-0.55 ± 0.22	1.2 ± 0.4
	B site	+0.3	Up	0.66 ± 0.21	
BFO/SRO	A site	-1.0	Down	-0.75 ± 0.18	1.5 ± 0.3
	B site	+1.0	Up	0.79 ± 0.20	
BFO/Nb:STO	A site	-1.0	Down	-1.2 ± 0.3	2.3 ± 0.6
	B site	+1.0	Up	1.1 ± 0.3	
PZT/LSMO	A site	+0.7	Up	0.86 ± 0.32	1.6 ± 0.6
	B site	-0.7	Down	-0.72 ± 0.25	

Table 3.1: Electronic reconstruction across the polar interfaces of ferroelectric heterostructures. The valence mismatch at the interface is calculated by assuming the ionic charge assignment with the nominal bulk valence for each layer. For example: the MnO_2-terminated interface ($La_{0.7}Sr_{0.3}O$-MnO_2-BiO-FeO_2) has the interface sheet charge density as $+0.7\,e/-0.7\,e/+1\,e/-1\,e$, thus the valence mismatch is calculated to be $-0.7\,e+1\,e = 0.3\,e$. The interface electrostatic potential step is calculated to be the difference between the internal fields of the two possible interface configurations within the same structure. Note: the B site-terminated SRO is achieved by depositing an atomic layer of TiO_2 on top SrO-terminated SRO.

The generality of this experimental approach has been extended to other ferroelectrics and conducting oxides listed in Table 3.1. Firstly, the heterostructure of "polar ferroelectric BFO and the "non-polar electrode $SrRuO_3$ (SRO) has been studied (Figure 3.9). Due to the high volatility of *Ru* element in the growth temperature ($\sim 700°$), the SRO layer will be self-terminated with SrO termination (Figure 3.2),

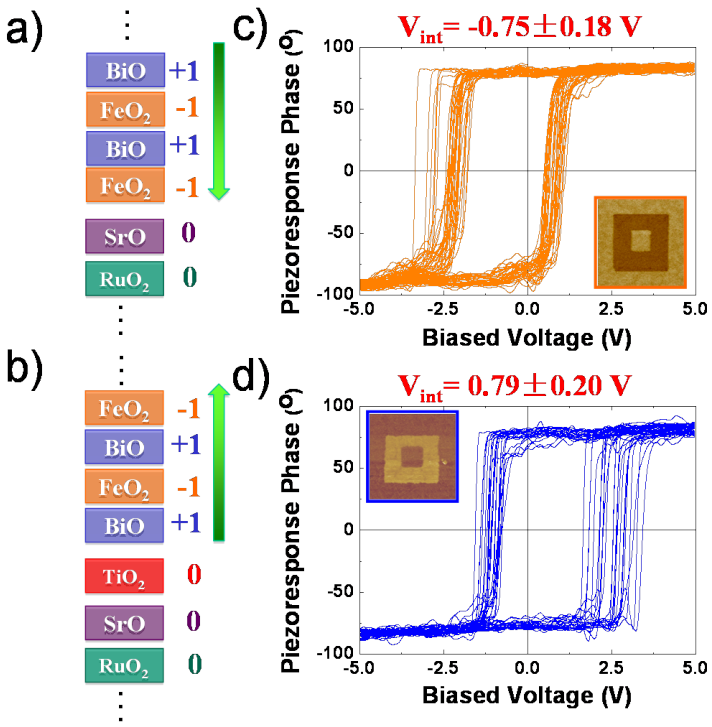

Figure 3.9: Interface tuning ferroelectric polarization at BFO/SRO heterostructures. Schematic diagram of the atomic stacking sequence of BFO/SRO heterostructure with RuO_2-SrO-FeO_2-BiO (a) and RuO_2-SrO-TiO_2-BiO-FeO_2 (b) interfaces, and the corresponding local piezoelectric hysteresis measurements of the both interface configurations(c,d). PFM measurements is shown in the inset of Figures (c,d). The RuO_2-SrO-FeO_2-BiO interface is designed by growing BFO directly on SRO/STO; while the RuO_2-SrO-TiO_2-BiO-FeO_2 interface was achieved by insertion of one atomic layer of TiO_2 between BFO and SRO.

thus the design of RuO_2-BiO termination is inaccessible. As a compromise, one atomic layer of TiO_2 was grown on the SrO terminated SRO to change the termination of the SRO from AO (SrO) to BO_2 (TiO_2). Moreover, since both RuO_2 and TiO_2 are charge neutral, thus non-polar, the heterointerface of TiO_2-BiO could be taken as a good approximation of RuO_2-BiO interface. The heterostructure of BFO and 0.5% Nb doped STO (Nb:STO) is chosen as another example, as shown in Figure 3.10. Growth of BFO directly on treated TiO_2 terminated Nb:STO will result in the SrO-TiO_2-BiO-FeO_2 interface. While SrO-terminated Nb:STO was achieved by depositing one atomic layer of SrO on top of the treated TiO_2 terminated Nb:STO substrate. Following growth of BFO on such substrates results in the TiO_2-SrO-FeO_2-BiO terminated BFO/STO heterostructure.

Despite the various carrier types carrier density, and work function of the electrodes, the PFM studies reveal exclusively that the ferroelectric polarization is con-

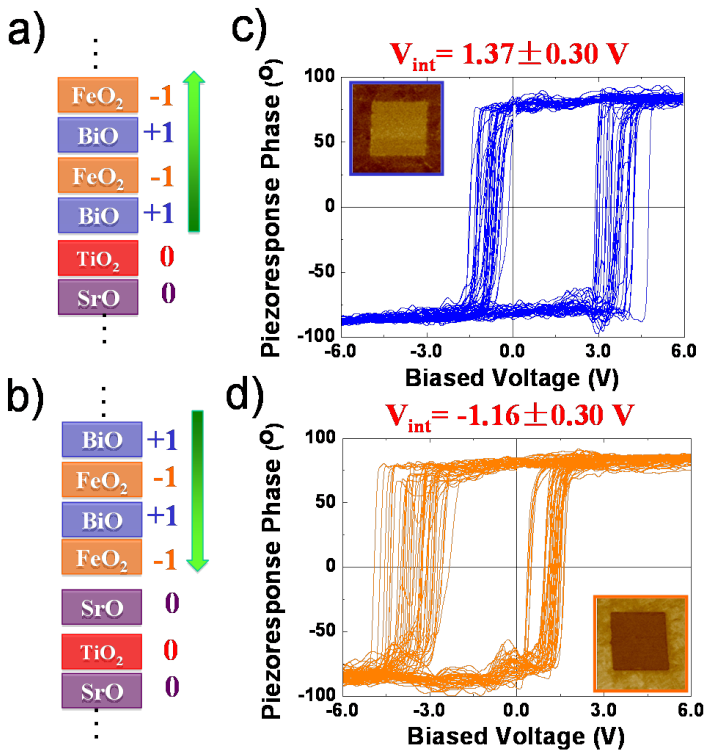

Figure 3.10: Interface tuning ferroelectric polarization at BFO/STO heterostructures. Schematic diagram of the atomic stacking sequence of BFO/STO heterostructure with SrO-TiO_2-BiO-FeO_2 (a) and TiO_2-SrO-FeO_2-BiO (b) interfaces, and the corresponding local piezoelectric hysteresis measurements of the both interface configurations(c,d). PFM measurements is shown in the inset of Figures (c,d). The SrO-TiO_2-BiO-FeO_2 interface is designed by growing BFO directly on STO; while the TiO_2-SrO-FeO_2-BiO interface was achieved by insertion of one atomic layer of SrO between BFO and STO.

trolled by the interface polar discontinuity. For BO_2-terminated SRO and Nb:STO, the as-grown polarization states are always pointing upward while the as-grown states are switched to downward for AO-terminated interfaces, as shown in Figures 3.9 and 3.10.

Furthermore, we have investigated the effect of different terminations on the ferroelectric $PbZr_{0.2}Ti_{0.8}O_3$ with LSMO underlayer (Figure 3.11). As expected, for the $La_{0.7}Sr_{0.3}O$-MnO_2-PbO-$Zr_{0.2}Ti_{0.8}O_2$ (+0.7 e/-0.7 e/0 e/0 e) interface, the as-grown polarization is pointing downward because of the accumulated negative interface charge and it becomes upward for the MnO_2-$La_{0.7}Sr_{0.3}O$-$Zr_{0.2}Ti_{0.8}O_2$-PbO (-0.7 e/+0.7 e/0 e/0 e) interface.

It is worth noting again that our simplified models (Figure 3.8c) are in excellent agreement with the results obtained with first-principle calculations (Figure 3.8b). Thus, instead of performing first-principle calculations in every heterostructure, a

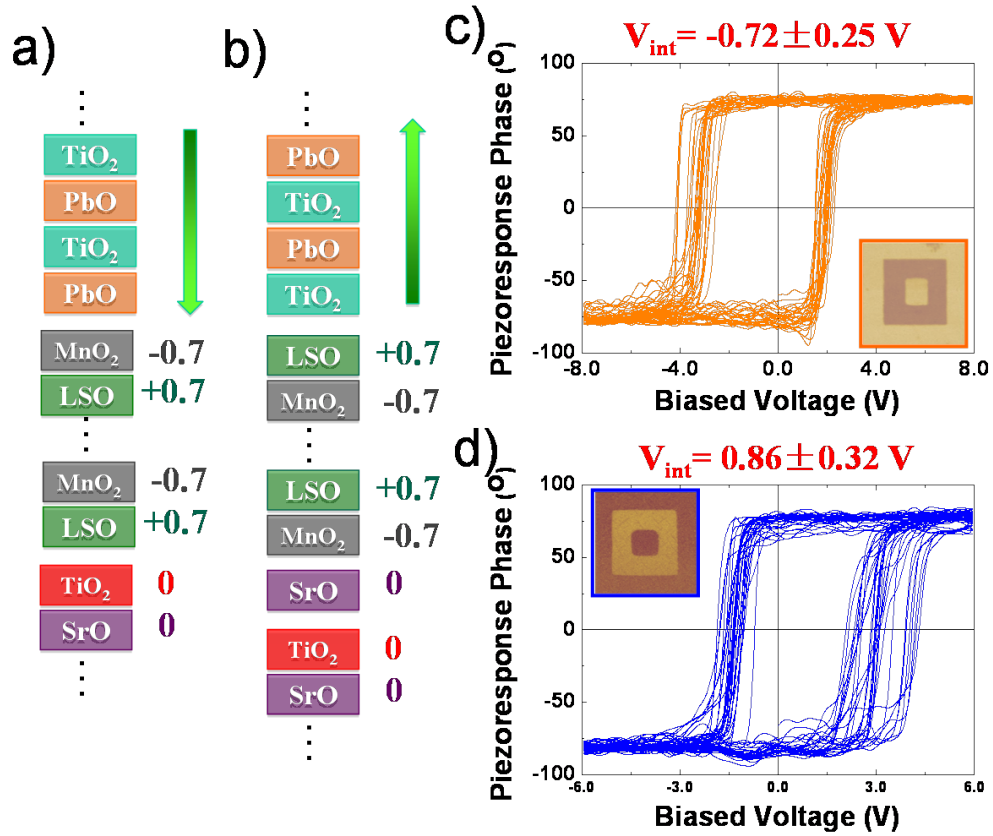

Figure 3.11: Interface tuning ferroelectric polarization at PZT/LSMO heterostructures. Schematic diagram of the atomic stacking sequence of PZT/LSMO heterostructure with $La_{0.7}Sr_{0.3}O$-MnO_2-PbO-$Zr_{0.2}Ti_{0.8}O_2$ (a) and MnO_2-$La_{0.7}Sr_{0.3}O$-$Zr_{0.2}Ti_{0.8}O_2$-PbO (b) interfaces, and the corresponding local piezoelectric hysteresis measurements of the both interface configurations(c,d). PFM measurements are shown in the inset of Figures (c,d).

generic model has been developed to interpret the observed Electronic interaction. As illustrated in Figure 3.8c, to overcome the possible divergence of the electrostatic field, the net interface charge density σ induced by the interface polar discontinuity would be screened by carriers inside the conducting material. With the assumptions that the screening charge is entirely located within a semi-infinite metal (conducting) layer with surface/interface at $z = 0$, the distribution of the screening charge could be determined by the Thomas-Fermi screening length λ with an exponential decay from the interface to the bulk as below [139]:

$$\rho(z) = \sigma/d^2\delta(z) - \alpha(z)\frac{\sigma}{\lambda}\exp\left(-z/\lambda\right)\begin{cases}\alpha = 0 & \text{if } z > 0\\ \alpha = 1 & \text{if } z < 0\end{cases} \tag{3.1}$$

where, d is the in-plane lattice constant of the heterostructure, $\alpha(z)$ is a step func-

tion. Thus this becomes a standard EM problem. The induced electric displacement, $\epsilon_0\epsilon E(z)$, is determined by the integral of the free charge density $\rho(z)$, where ϵ is the dielectric constant of the conducting layer. It is straightforward that the interface induced electrostatic potential step ΔV can be calculated directly with integral of the electric field by:

$$\Delta V = \int_0^\infty E(z)\, dz = \lambda \frac{\sigma}{d^2 \epsilon_0 \epsilon}, \tag{3.2}$$

We note that the Thomas-Fermi screening length (λ) in the electrode is given by:

$$\lambda = \sqrt{\frac{(\pi/3)^{1/3}\hbar^2 \epsilon_0 \epsilon}{4me^2 n^{1/3}}} = \sqrt{\frac{(\pi/3)^{1/3} a_0 \epsilon}{4m^* n^{1/3}}}, \tag{3.3}$$

where m is carrier effective mass, n is carrier density. a_0 is Bohr radius, and $m^* = m/m_e$.

Finally, the interface polar induced potential step can be expressed as:

$$\Delta V = \sqrt{\frac{(\pi/3)^{1/3} a_0 \epsilon}{4m^* n^{1/3}}} \frac{\sigma}{d^2 \epsilon_0 \epsilon} = \sqrt{\frac{(\pi/3)^{1/3} a_0}{4m^* n^{1/3} \epsilon}} \frac{\sigma}{d^2 \epsilon_0}, \tag{3.4}$$

Clearly, the interface induced potential step is proportional to interface polar discontinuity, thus charge density σ/d^2, and inversely proportional to the dielectric constant ($\sqrt{\epsilon}$), the effective mass ($\sqrt{m}$) and carrier density ($n^{1/6}$).

Structure	ϵ	m/m_e	n (10^{21}/cm^3)	λ (nm)	V_{th} (V)	V_e (V)
BFO/LSMO	30 [138]	4 [143]	5 [138]	0.24	1.1	1.2 ± 0.4
BFO/SRO	100 [144]	4.4 [145]	20 [146]	0.38	1.6	1.5 ± 0.3
BFO/Nb:STO	150 [147, 148]	7 [149]	0.1 [149]	0.79	2.4	2.3 ± 0.6
PZT/LSMO	30 [138]	4 [143]	5 [138]	0.24	2.6	1.6 ± 0.6

Table 3.2: Comparison between experimental results and phenomenological calculations for the interface induced electrostatic potential step.

Using the parameters obtained from literatures and Equation 3.4, we have calculated the Thomas Fermi screening length as well as interface induced potential steps as listed in Table 3.2. The consistency between the theoretical values of the potential step based on this simple model and the experimental values observed with the ferroelectric hysteresis loop measurements, is remarkable and serves to substantially extend the generality of the findings. We note that for the Nb:STO case, since the charge carrier density is far below the screening charge density, the charge carrier will be fully depleted at the interface. Thus other screening mechanisms, such as ionic screening (polarization penetration) [142], will be required. In that case, a more suitable method, such as DFT will be required to describe the construction across the interface. Nevertheless, the interface dipole will still be persisted, thus creating the interface potentials step with the similar manner as we proposed above.

3.4 Summary

In summary, we have demonstrated that atomically precise interface control can lead to dramatically different polar states in ferroelectrics. This occurs primarily through the coupling of the interface potential to the polar order. We note that while there is considerable interest in the scientific community focused on the interface itself (and various phenomena related to the interface), we argue that the influence on the bulk properties of the thin films can be equally important. Clearly, such a coupling effect between interface properties and the bulk order parameters of the thin films is, in principle, not limited to the electrostatic degree of freedom. Imbalance in other degrees of freedom (for example, the spin or orbital degrees of freedom) may be used to control the properties of the bulk as well. In the next few chapters, we will focus on another interesting aspect of this, namely how the interface spin interaction could affect the macroscopic magnetism of LSMO layer.

Chapter 4

Magnetic coupling across BFO/LSMO heterointerfaces

4.1 Review of exchange-bias coupling

As stated in chapter 1, at the interface between a ferromagnet and an antiferromagnet, the spin degree of freedom reconstructs in a manner to form exotic interfacial spin structures and leads to novel functionalities. As one of the most intriguing phenomena associated with this spin coupling, exchange-bias coupling (also called unidirectional anisotropy) was first discovered in 1956 by Meiklejohn and Bean. [150] During a study of ferromagnetic (FM) Co particles embedded in their native antiferromagnetic (AFM) oxide (CoO), they observed a shift of the center of the magnetic hysteresis loop from its normal position of $H = 0$ to $H_E \neq 0$. And such a shift is usually taken as a characteristic signature of the exchange-bias coupling today. After this break through finding, exchange-bias coupling has attracted extensive research interests [96, 151–153], due to its crucial technological importance [154, 155].

Traditionally, exchange-bias coupling is induced when cooling the magnetic bilayer across the Néel temperature of AFM layer with a magnetic field. Figure 4.1 shows a schematic illustration of spin configurations for exchange-bias coupling between an AFM-FM bilayer. In the current case, a FM coupling is assumed at the interface. When the temperature is below the Curie temperature of FM layer while above the Néel temperature of AFM layer, the FM spins line up with the magnetic field, while the AFM spins remain in random states (Figure 4.1a). After subsequent cooling to the temperature below Néel temperature, the top layer AFM spins align ferromagnetically with those of the FM, as a consequence of the FM coupling at AFM-FM interface. The remaining layers of the AFM follow the intrinsic AFM ordering thus to achieve a zero net magnetization in the AFM layer, as expected. Therefore, energetically favored spin configuration is formed as shown in Figure 4.1b. When sweeping the magnetic field from positive to negative, the FM spin starts to rotate, while AFM spins

remain unchanged due to the large AFM anisotropy (Figure 4.1c). This antiparallel configuration is energetically unfavorable due to the presence of FM coupling across the AFM-FM interface. In other words, the magnetic field required to reverse an FM layer to be antiparallel to the interfacial AFM spins (Figure 4.1c) is larger than what is needed the other way(Figure 4.1e). Therefore, the FM spins have one single stable spin configuration, i.e. the anisotropy is unidirectional.

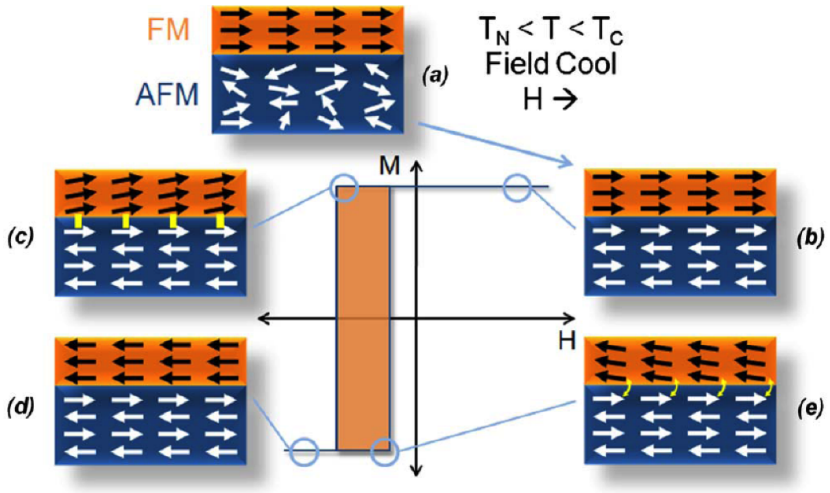

Figure 4.1: Schematic illustration of spin configurations for exchange-bias coupling between a FM-AFM bilayer. The diagrams show the spin configuration above T_N (a) and below T_N with different applied magnetic fields. The AFM spin structure is frozen upon the temperature below T_N, which leads to the unidirectional anisotropy of FM layer through magnetic coupling. Adapted from ref. [96, 156].

With this simple mode, one can go on step further to estimate the exchange-bias field. In such a system, the spin free energy can be described as below [157, 158]:

$$F = HM_{FM}t_{FM}\cos\theta - J_{Int}\cos\theta + K_{FM}\sin^2\beta; \tag{4.1}$$

where H is the magnetic field, M_{FM}, t_{FM} and K_{FM} are the magnetization, thickness and magnetic anisotropy of the FM layer respectively, J_{Int} is the magnetic interaction at the interface, θ is the angle between the magnetic field and FM spins, and β is the angle between the applied magnetic field and FM anisotropy axis. Note that in this simple mode, it is assumed that the magnetic anisotropy of the AFM layer is much larger than that of the FM layer.

By solving the equation above, an effective magnetic field can be defined as:

$$H' = H - \frac{J_{Int}}{M_{FM}t_{FM}} = H - H_E; \tag{4.2}$$

with

$$H_E = \frac{J_{Int}}{M_{FM} t_{FM}}. \tag{4.3}$$

We note that although this simple model can provide a meaningful physics picture about the exchange-bias coupling in term of the relationship between the exchange-bias field (H_{EB}) and the interfacial magnetic coupling strength (J_{Int}), the thickness (t_{FM}) and magnetization (M_{FM}) of the ferromagnetic layer, it is not satisfactory in a few fundamental aspects.

Firstly, the amplitude of the exchange-bias field is generally a few orders of magnitude lower than what is expected based on this model. To account for this discrepancy, numerous theoretical models have been proposed, such as Néel model [159], random interface model [160–162] and AF domain wall model [163]. The key idea of those models is that only part of the uncompensated spins are pinned at the interface. This has been confirmed by recent x-ray circular dichroism (XMCD) experiments carried by Stohr *et al.* [164] They showed that in fact only a few percent (4 %) of the AFM interfacial moments are pinned, and the majority of the spins rotate coherently with the ferromagnetic layer. However, the nature (or origin) of the pinning is still unknown. Although previous models try to related this pinning with either random defects or AFM domain walls at the interface, recent experiment studies show that the pinned spins can be located much deeper in the bulk of the AFM. [165–167]

Secondly, the simple model can not explain the exchange-bias coupling in systems with compensated AFM interfacial spin structures. One major problem with this model is that it assumes a rigid spin lattice structure, i.e. AFM spins remain in their bulk configuration, which however is not valid for the real system with a finite AFM layer anisotropy. We note that the magnetic coupling across the interface between a compensated AFM and a FM leads to spin frustration as has been discussed in chapter 1, resulting in novel and uncompensated interfacial spin structures. Based on this argument, a few theoretical models have been proposed to explain the exchange-bias effect observed in the compensated AFM interface. [168–171] However, the pinning mechanism of the interfacial spins is still unclear.

Finally, we emphasize that although exchange-bias coupling has been discovered for more than 60 years, the underlaying physics is still unclear and is attracting extensive research interests, both from theoretical and experimental sides. The key questions for this lay in two issues: the first one is how interfacial spins (both in AFM and FM layers) reconstruct at the interface between AFM and FM; the second one is how the induced spins are pinned at the interface, leading to exchange-bias coupling (or unidirectional anisotropy) to the FM layer. In the study of this dissertation, we will focus on the former issue, while leaving the second one for future studies.

4.2 Exchange-bias coupling at BFO/LSMO heterostructures

This section is dedicated to the study of exchange-bias coupling at $BiFeO_3$ and $La_{0.7}Sr_{0.3}MnO_3$ (BFO/LSMO) heterostructures. The correlation between exchange-bias coupling with interface atomic structure and the related temperature, and thickness dependence measurements are investigated. Magnetic measurements were carried out with a Quantum Design SQUID magnetometer (MPMS).

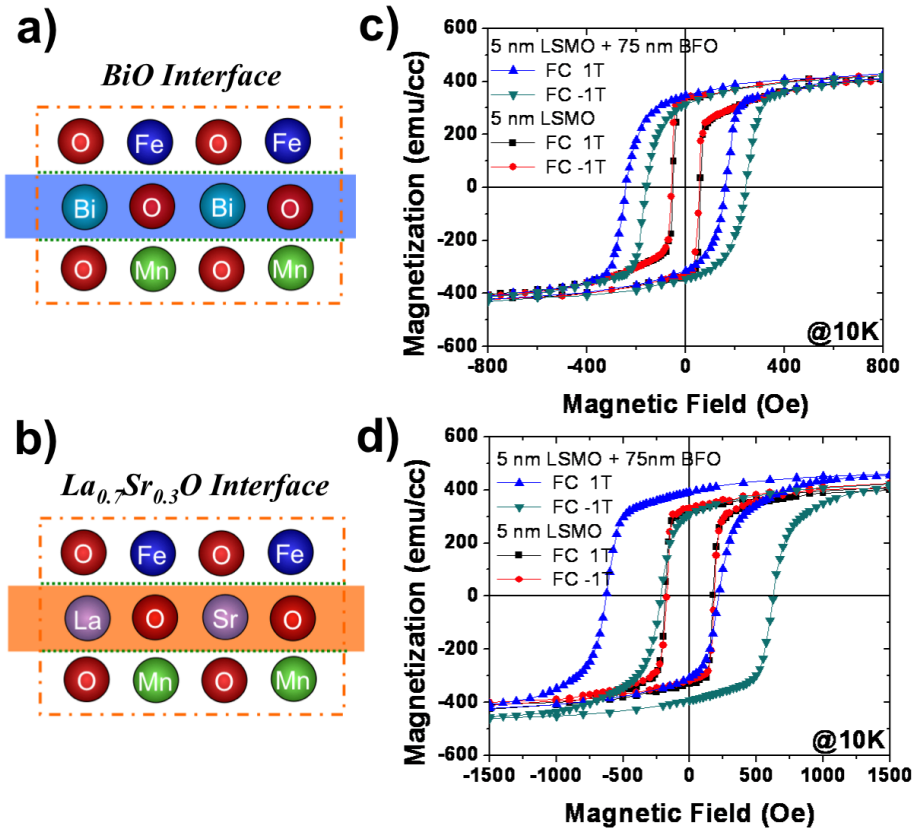

Figure 4.2: exchange-bias coupling at BFO/LSMO heterointerfaces. Schemtatic atomic stacking sequences (a, b) and Exchange-biased hysteresis loops (c, d) of LSMO/BFO heterostructures with BiO interface and $La_{0.7}Sr_{0.3}O$ interface, respectively. Magnetic hysteresis loops of LSMO films terminated by MnO_2 (a) and $La_{0.7}Sr_{0.3}O$ top layers are shown for comparison.

As stated in previous chapter, two possible atomic stacking sequences can be formed between BFO and LSMO layers, namely BiO and $La_{0.7}Sr_{0.3}O$ interfaces, as illustrated in Figure 4.2a and 4.2b. First, we compare the deference of magnetic coupling between them. Magnetic measurements were carried out using a Quantum

Design SQUID magnetometer (MPMS) along the [100] axis. Before measurements, samples were cooled down from 350 K to the measurement temperature with the (+/-) magnetic field along the [100].

Figure 4.2c shows the magnetization curve of BFO/LSMO heterostructure with BiO interface. Compared with the MnO_2 terminated LSMO film (without BFO), the magnetic hysteresis of BFO/LSMO heterostructure clearly exhibits both an enhancement of the coercive field (~200 Oe vs. ~40 Oe) and a shift of the hysteresis loop along the magnetic axis with the bias field of ~40 Oe, which are the hallmarks of exchange-bias coupling. On the other hand, much larger exchange-bias field (~200 Oe) and coercive field enhancement (~400 Oe) were observed in the heterostructure with LSO interface as shown in Fig. 4.2d. It is important to emphasis that, without the BFO layer, the magnetic hysteresis loops of LSMO thin films with both MnO_2 (Fig. 4.2c) and $La_{0.7}Sr_{0.3}O$ (Fig. 4.2d) terminations are symmetric around the zero-field under either positive or negative cooling field. This suggests that the exchange-bias effect observed is purely a consequence of the magnetic coupling between the AFM (BFO) and FM (LSMO) layers in the heterostructure, and the stronger exchange-bias coupling observed in $La_{0.7}Sr_{0.3}O$ (LSO) interface indicates possibly a stronger magnetic coupling, compared with that of the other interface.

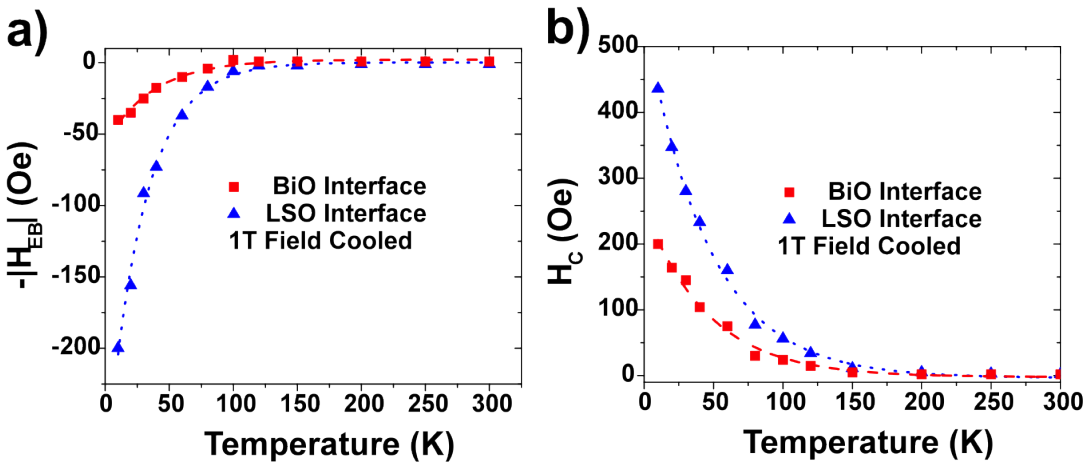

Figure 4.3: Temperature dependence of exchange-bias coupling. Temperature dependence of (a) exchange-bias fields (H_{EB}) and (b) magnetic coercive fields (H_C) for both interfacial configurations. The dot and dash lines are the empirical fittings for the experimental data with the equation as: $H(T) = H_0 \exp(-k_B T/E_0)$, where H_0 is the coercive field (exchange-bias coupling) strength at zero temperature and E_0 is the activation energy of the magnetic coupling at the interfaces.

Temperature dependence measurements of both the exchange-bias field (H_{EB}, Fig. 4.3a) and coercive field (H_C, Fig. 4.3b) for these two interfaces reveal yet another interesting aspect of the magnetic interaction between BFO and LSMO layers. For

both BFO/LSMO heterostructures, the exchange-bias shift vanishes above ∼100-120 K (Figure 4.3a), suggesting the existence of a "blocking temperature", which in our case is significantly lower than both the ferromagnetic T_C of the LSMO film (measured to be ∼320 K in these thin films) and the antiferromagnetic T_N of the BFO film. It is interesting to note that this blocking temperature corresponds closely to the temperature above which spin polarization, as measured by photoemission, is lost in LSMO as well as the onset of tunnel magnetoresistance in LSMO/STO/LSMO tunnel junctions. Careful analysis reveals that for both cases, the coercive and exchange-bias fields decrease exponentially with increase of temperature, which is a strong evidence of the spin frustration at the interface. [172, 173] The dot and dash lines are the empirical fittings for the experimental data with the equation as:

$$H(T) = H_0 \exp\left(-k_B T / E_0\right), \tag{4.4}$$

where H_0 is the coercive field (exchange-bias coupling) strength at zero temperature and E_0 is the activation energy of the magnetic coupling at the interfaces. This finding is further supported by the finding of magnetism at the proximity of BFO in LSMO/BFO heterostructure using x-ray magnetic circular dichroism (XMCD) measurements, which will be discussed in details in chapter 4. The difference between the coupling strengths at these two interfaces indicates that the magnetic coupling across the interface is strongly correlated with the lattice and electronic structures at the heterointerface.

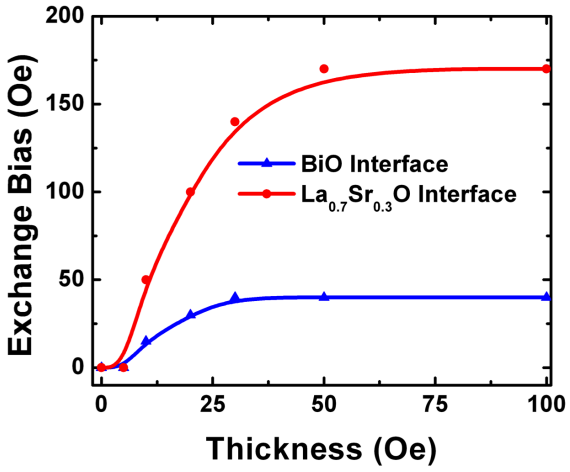

Figure 4.4: Thickness dependence of exchange-bias coupling for BFO/LSMO heterostructures.

To obtain further physics insight into the exchange-bias coupling for both heterointerfaces, thickness dependence measurements of the antiferromagnetic BFO layer have been carried out, with data shown in in Figure 4.4. For BFO layers over ∼20-30 nm

thick, H_{EB} is essentially constant, independent of thickness of the antiferromagnetic layer; below this thickness it progressively decreases and below ∼5 nm of BFO, the bias field essentially goes to zero. The critical thickness could mainly be induced by the finite-size scaling of the Néel temperature (antiferromagnetic ordering) of BFO. Similar trend has also been reported in the other systems, for example NiFe/CoO reported by T. Ambrose and C. L. Chien. [174] Moreover, it is worth noting that the similar temperature and thickness dependent measurements strongly indicates similar coupling mechanism between these two heterointerfaces, although the coupling strengths are different.

4.3 Comparison with the case of CoFe/BFO heterostructures

Finally, It is important to note that the mechanism of the exchange-bias coupling described for BFO/LSMO heterostructures studied here is fundamentally different from what has been reported in previous studies of metallic ferromagnets ($Co_{0.9}Fe_{0.1}$(CoFe)) in contact with BFO. In the latter case, previous studies have shown that the exchange-bias coupling is directly correlated with the density of ferroelectric (also antiferromagnetic) domain walls (more precisely, 109° domain walls) in BFO. [175, 176] However, this is not observed in the study on BFO/LSMO heterostructures. Regardless of the BFO domain structure, similar exchange-bias field are observed at temperature less than ∼ 120 K. This low temperature onset of the exchange-bias field is yet another important difference between the BFO/LSMO heterostructures and the previously studied CoFe/BFO system, which points to a fundamental difference in the nature of exchange coupling. Temperature dependence studies of CoFe/BFO heterostructures show no observable change in the magnitude of exchange-bias field as a function of temperature from 300 to 10 K regardless of the underlying BFO domain structure. Therefore, these differences in coupling behavior suggest the possibility of a fundamentally different mechanism at such epitaxial interfaces between BFO and LSMO, which will be studied in next chapter.

Chapter 5

Origin of exchange-bias coupling: interface magnetism and orbital reconstruction

In this chapter, we report the formation of a novel ferromagnetic state in antiferromagnet $BiFeO_3$ at the interface with $La_{0.7}Sr_{0.3}MnO_3$. Using x-ray magnetic circular dichroism at Mn and Fe $L_{2,3}$-edges, we discovered that the development of this interfacial ferromagnetic spin structure is strongly associated with the development of a significant exchange-bias coupling. Moreover, our polarization-dependence of x-rays absorption measurements at oxygen K-edge strongly suggest that the novel magnetic state is directly related to an electronic orbital reconstruction at the interface. [177]

5.1 Motivation: origin of the exchange-bias coupling

In the previous chapter, we have reported the emergent of an exchange-bias coupling at $BiFeO_3/La_{0.7}Sr_{0.3}MnO_3$ (BFO/LSMO)heterostructures. However, the origin/mechanism of this interesting effect is still unclear. In an exchange-bias system, the exchange-bias field breaks the in-plane inversion symmetry by shifting the otherwise symmetric hysteresis loop to one side along the magnetic field axis. This indicates that a pinned (unrotatable) spin-state is formed at the interface, which is usually located at the antiferromagnet (AFM) side due to its larger spin anisotropy energy. [96] In the current system, the strong AFM superexchange coupling between the Fe^{3+} (d_5) ions lead to the G-type AFM spin structure (Fig. 5.1a), which has a compensated spin structure at the (001) plane. [100] Thus in order to help elucidate the origin of the exchange-bias coupling at the BFO/LSMO interface, it is fundamentally necessary to obtain direct information of the interfacial spin structures, especially at BFO side.

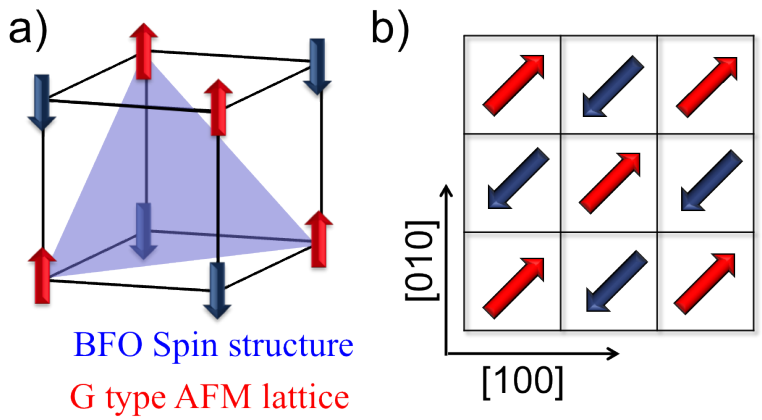

Figure 5.1: Magnetic spin architecture structures of $BiFeO_3$ thin films in three dimension (a) and [001] plane-view (b).

In this chapter, we report an unexpected ferromagnetic order induced in the Fe sublattice at the interface with LSMO as a consequence of a complex interplay between the orbital degree of freedom and its coupling to the spin degree of freedom. [177] Using x-ray magnetic circular dichroism at Mn and Fe $L_{2,3}$-edges, we discovered that the development of this ferromagnetic spin structure in the BFO sublattice at the interface with LSMO is strongly associated with the development of a significant exchange-bias coupling, both exhibiting the same temperature dependence. Moreover, our results demonstrate that the magnetic state is directly related to an electronic orbital reconstruction at the interface, which is supported by the polarization-dependence of x-rays absorption measurements at oxygen $K-$edge. The discovery of correlation between the electronic orbital structure at the interface and exchange-bias coupling suggests the possibility of using an electric field to control the magnetization of ferromagnet without complex domain engineering.

5.2 Interface ferromagnetism at LSMO/BFO heterointerface

To probe the interface magnetic configuration, x-ray absorption spectroscopy (XAS) spectra were acquired by recording the total electron yield (TEY) current as a function of x-ray photon energy at beamline U4B of the National Synchrotron Light Source at Brookhaven National Laboratory. During the measurement, L-edge XAS were used to probe the excitation of electrons from $2p$ to $3d$ level for the transition metals. Since different elements have very different characteristic XAS spectra (in terms of energy position and line shape), XAS is an element specific measurement technique. In the TEY (photon-in-electron-out) experiment, the total yield electrons

due to the element specific resonance absorption have a typical escape depth of 5-10 nm, making it an ideal tool to probe heterointerfaces such as ours. [16, 178]

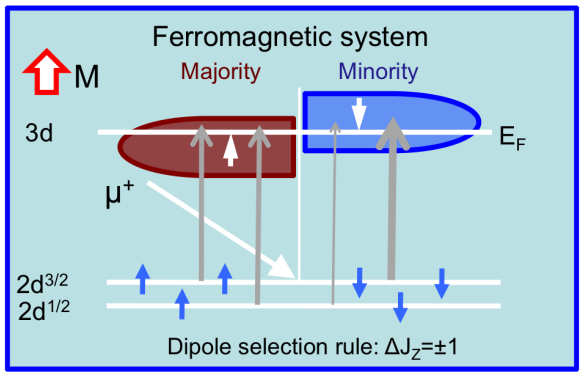

Figure 5.2: Schematic illustration of X-ray magnetic circular dichroism.

Left- and right-circular polarized photons were used in the measurement, and they carry different angular momenta, which would be transferred to photoelectrons during the absorption process. Because of spin-orbital coupling, absorption cross sections for left- and right-circular polarized photons are different. Thus, X-ray Magnetic Circular Dichroism (XMCD) can be used to probe the ferromagnetic ordering of the heterostructure at the interface, by measuring the differential absorption spectra of the left- and right- circularly polarized x-rays in the vicinity of atomic core levels; as shown in Figure 5.2. [179] In the current study, we examined the Mn and Fe L_3 ($2p_{3/2}$ to 3d) and L_2 ($2p_{1/2}$ to 3d) spin-orbit split core levels. The sign of the XMCD signal gives us information about the direction of the spin, and the amplitude of the peak gives us information about the magnitude of the magnetization. A schematic figure of the experimental setup is shown in Figure 5.3. 70% circular polarized x-rays were

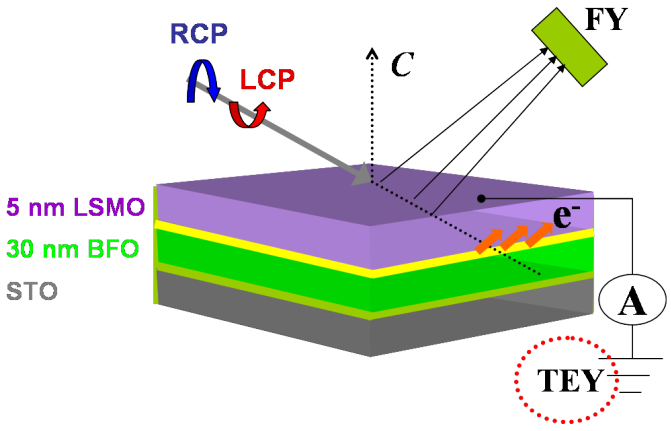

Figure 5.3: Schematic diagram of experimental setup used to obtain the x-ray magnetic circular dichroism.

employed to gain higher beam intensities. To obtain a sizable magnetic dichroism, the film plane is tilted with respect to the photon beam propagation direction, with an incident angle of 30° employed in this study.

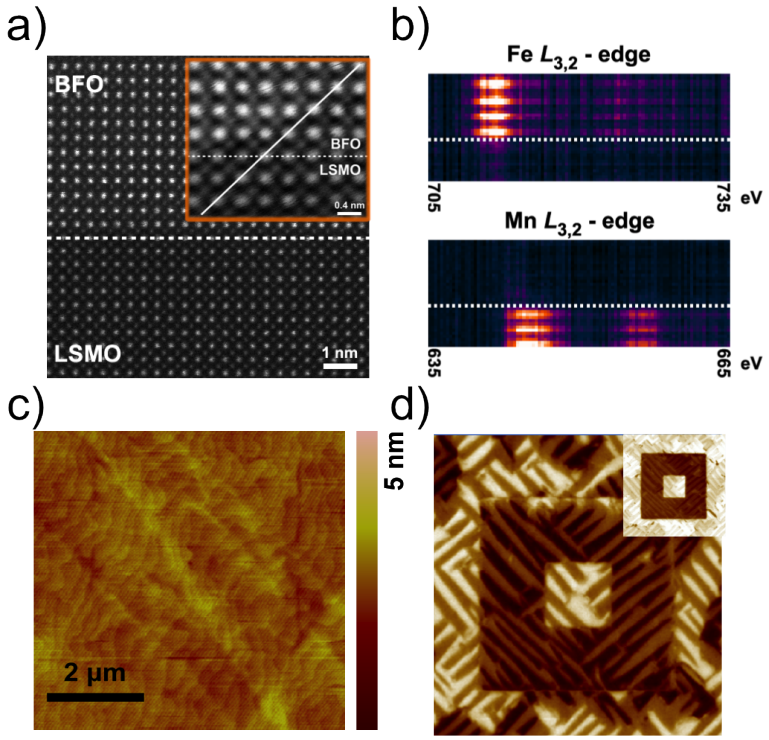

Figure 5.4: Structure and chemical characterization of LSMO/BFO heterostructures. (a) HAADF-STEM image obtained at 300 kV (TEAM 0.5 microscope) and (b) elemental STEM-EELS line scan acquired at 45° across the LSMO/BFO interface (100 kV, VG HB 501 microscope). (c) surface topography of the LSMO/BFO/SRO//STO heterostructure as measured by contact mode atomic force microscopy. (d) In plane ferroelectric domain structure of BFO/SRO//STO heterostructure measured with piezo force microscopy, with out-of-plane domain structure shown in the inset.

To study the interface spin structures, especially the spin arrangement in the AFM BFO at the heterointerface with FM LSMO, heterostructure of LSMO/BFO was designed as shown in Figure 5.3, in which, ferromagnet LSMO (top layer, 5 nm) and BFO (bottom layer, 30 nm) were grown on 5 nm $SrRuO_3$ buffered (001) Nb-doped $SrTiO_3$ substrates, using pulsed-laser deposition while monitoring the growth process with reflection high-energy electron diffraction. The atomic and chemical configuration at the LSMO/BFO interfaces was studied with high-angle annular dark-field (HAADF) imaging and spatially resolved electron energy-loss spectroscopy (EELS) performed in scanning transmission electron microscopy (STEM) mode. Figure 5.4a shows a typical HAADF image of such a LSMO/BFO heterostructure. The clear contrast indicates an atomically sharp interface between the LSMO and BFO. The chemically

abrupt nature of these interfaces is confirmed through EELS measurements on Fe- and Mn-edges across the interface (Fig. 5.4b), which clearly shows the transition from Mn to Fe at the interface, and the cationic intermixing at the interface is minimal. Moreover, the identical Fe spectra taken at the interface and far from the interface of BFO clearly indicate that the valence state of the Fe at the interface is the same as that in the bulk, i.e., the +3 oxidation state. [180] Thus, the charge transfer between BFO and LSMO at the interface could be eliminated. The smooth topography of the heterostructure is further confirmed by atomic force microscopy measurements (Fig. 5.4c), which reveals that the surface of the film has an atomic-scale step structure with a root-mean-square roughness ∼0.25 nm. The ferroelectric domain structure of a typical BFO/SRO//STO heterostructure was analyzed using piezoresponse force microscopy (PFM) (Fig. 5.4d), and indicated the presence of stripe-like domains (71° domain walls) [176], as shown in previously study, where the polarization direction was nicely switchable and stable.

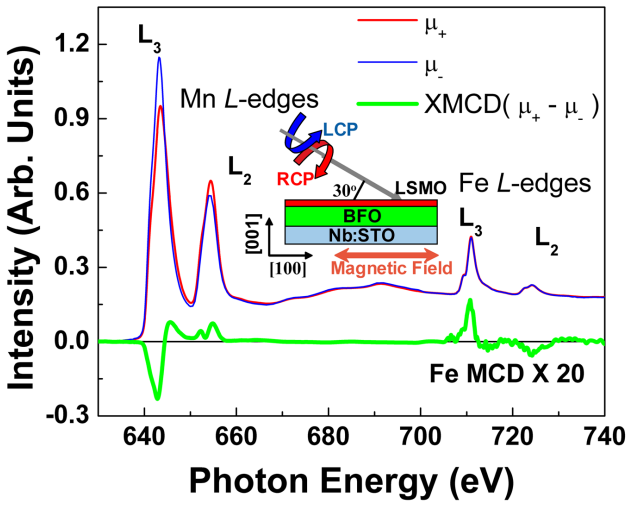

Figure 5.5: X-ray absorption spectra and x-ray magnetic dichroism of Mn and Fe $L_{2,3}$ edges at the $La_{0.7}Sr_{0.3}MnO_3/BiFeO_3$ heterostructure. The XMCD signal of Fe is multiplied by a factor of 20. The XMCD spectra of Mn and Fe L_3 edges have opposite signs, suggesting that the coupling between the Mn and Fe across the interface is antiferromagnetic in nature. The data were taken at 10 K.

With suitable samples in-hand, we start to measure/explore the interesting spin structure at the interface. Figure 5.5 shows the representative XAS and XMCD spectra measured at the Mn and Fe L-edges at 10K. Well-defined XMCD spectra were observed for both the Mn and Fe L-edges. The XMCD of $\sim$ 23 % at the Mn L_3-edge is consistent with previously measured values. [181] However, the $\sim$ 4 % XMCD observed at the Fe L_3-edge is surprisingly large considering that the nominal canted moment of BFO ($\sim$ 0.02-0.05 μ_B/Fe) [182, 183], is well below the resolution

of such XMCD studies. To rule out experimental artifacts, we carried out control measurements on a 30 nm BFO sample without the LSMO capping layer in which no measurable XMCD effect was observed (green data, Fig. 5.6). We note that a macroscopic SQUID measurement of the same sample does show a measurable, albeit small, saturation moment of $\sim$0.03 μ_B/Fe, consistent with published values for the canted moment of BFO. [183] Finally, we repeated the XMCD measurements on another LSMO/BFO heterostructure grown under identical conditions; the results of this run are essentially identical to the first set of data and are also presented in Fig. 5.6. This data strongly suggests that in the top few nanometers of the BFO film a new magnetic spin structure is present that is markedly different from that in the remainder of the BFO film. Additionally, the relative orientation between the Mn and Fe magnetic spins can be deduced from the sign of the dichroism at their respective edges. Figure 5.5 shows that the XMCD spectra have opposite signs for the Mn and Fe L-edges, indicating that the coupling between the Mn and Fe across the interface is antiparallel in nature. Although the actual spin structure at the interface could be complex, these XMCD spectra suggest that the coupling between the bulk LSMO spins and the bulk antiferromagnetic spin lattice of BFO is mediated through a very thin (a few unit cells) novel magnetic layer localized at the interface. [179]

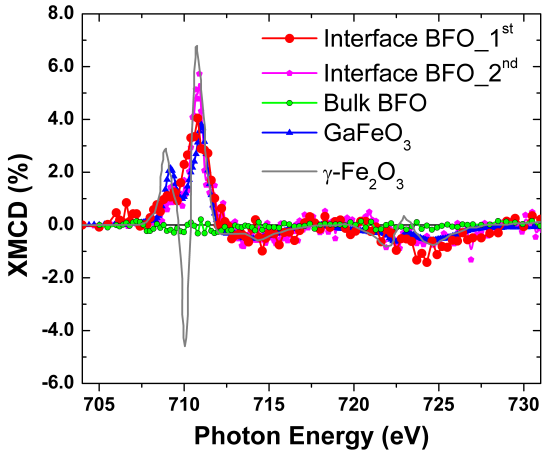

Figure 5.6: Comparison of the interface Fe XMCD with the reference samples of bulk BFO, $GaFeO_3$ and γ-Fe_2O_3. The spectra of $GaFeO_3$ and γ-Fe_2O_3 are normalized to the same scale as those of interface BFO state. No measurable XMCD is observed in BFO layers without a top LSMO layer. The comparison between the interface BFO state and the spectra for $GaFeO_3$ and γ-Fe_2O_3 suggests that the electronic state of the induced magnetic moment is similar to the $GaFeO_3$ system (O_h site, Fe^{3+}).

To trace the origin of the magnetization at the interface, we have compared the dichroism of the interface BFO with reference samples, namely, ferrimagnetic

γ-Fe_2O_3 [183] and multiferroic $GaFeO_3$ [184] (Fig. 5.6), with both curves normalized to the dichroism of the interface BFO state. In γ-Fe_2O_3, the Fe atom occupies both octahedral (O_h) and tetrahedral (T_d) sites that are magnetized antiparallel to each other. The comparison between XMCD spectra for BFO and γ-Fe_2O_3 in Fig. 5.6 clearly shows that the dichroism of the BFO is very different from that of the γ-Fe_2O_3, specifically in that it lacks the reversal of the XMCD spectra corresponding to the T_d site at $\sim$ 710 eV. The comparison between the XMCD for BFO and $GaFeO_3$, on the other hand, reveals almost identical features, confirming the similarities in the lattice structure and electronic state of Fe in these two materials (O_h site, Fe^{3+}). From these results, it can be concluded that the relatively large magnetic moment at this heterointerface is arising from Fe^{3+} ions on O_h sites and unlikely to be the result of anion non-stoichiometry that might change the valence state of the Fe, which is also supported with the EELS measurements across the interface (Fig. 5.4).

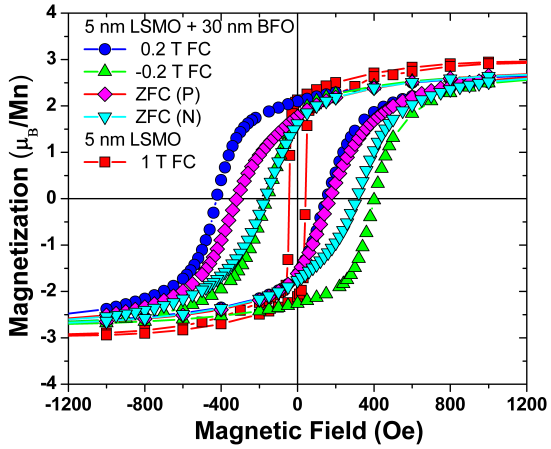

Figure 5.7: Magnetic hysteresis loops of a single LSMO layer (red), and LSMO/BFO (blue and green) heterostructure measured along [100] direction at 10 K after +/- 0.2 T field cooling from 350 K, respectively, showing a strong enhancement of the coercive field as well as the shift of the hysteresis loop along the magnetic axis. exchange-bias effect has also been observed for zero field cooled (ZFC) measurements, which depends on the sign of the magnetic virgin state.

Bearing in mind that a novel spin state has been formed in the AFM BFO at the heterointerface with FM LSMO, we have gone further to study how this emergent state is correlated with the exchange-bias effect observed. Macroscopic SQUID magnetometry was carried out at 10 K along the [100] direction. Figure 5.7 shows a typical magnetic hysteresis loop for the heterostructure consisting of 5 nm LSMO and 30 nm BFO after field cooling from 350 K to 10 K in both +/-0.2 T magnetic fields. We observe both a strong enhancement of the coercive field ($\sim$275 Oe) compared

to that of the LSMO/STO sample (∼40 Oe, red curve, Fig.5.7) and a shift of the hysteresis loop opposite to the cooling field direction with an exchange-bias field of 140 Oe (exchange-bias field, EB).

As we stated in the previous chapter, such an EB effect requires the presence of pinned, uncompensated spins in the antiferromagnet at the interface [96,160,168,178, 185] and is induced by the interface coupling between LSMO and BFO. Exchange-bias effect has also been observed for zero field cooled (ZFC) measurements. During the ZFC process, LSMO will self polarized, which could lead to either negative (N) or positive (P) magnetic virgin state. With negative (positive) virgin state, a positive (negative) shift of the hysteresis loop along the magnetic field axis was observed, which is similar with the case applying negative (positive) coupling field, although the exchange-bias field is suppressed. The reduction of the exchange-bias field could be understood by taking into account the fact that the magnetization of virgin state is smaller than the saturation magnetization, meaning a less aligned magnetic domain configuration at the interface. This result indicates a strong direct magnetic coupling between LSMO and BFO.

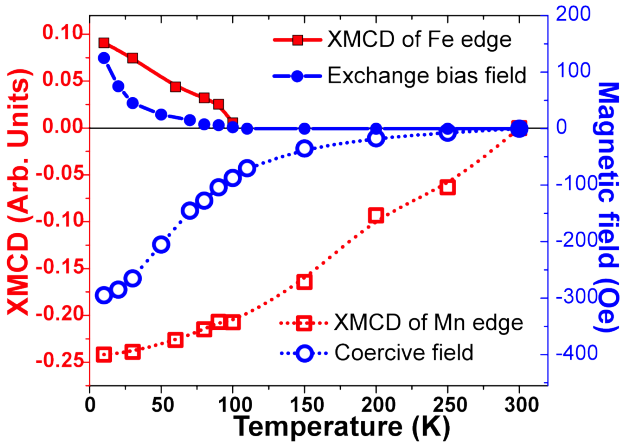

Figure 5.8: Temperature dependence of the XMCD signal of Fe (solid red) and Mn (open red) compared with the exchange-bias field (solid blue) and coercive field (open blue) as measured by SQUID.

Temperature dependent XMCD and SQUID measurements (Figure 5.8) clearly demonstrate a strong interdependence between the ferromagnetic state in the Fe-sublattice at the interface and the exchange coupling between these two layers. As expected, the XMCD of Mn persists until ∼ 300 K, consistent with the Curie temperature of ultra-thin LSMO films. [121] The temperature dependent measurements of hysteresis loops show, however, that the EB field vanishes at a blocking temperature (TB) of ∼100 K. Interestingly, an exactly analogous behavior is also found for the

XMCD spectra of Fe (this was repeated in 3 samples), strongly suggesting that the novel magnetic moment in the Fe-sublattice is the source of the EB.

5.3 Spin sum rule and calculation of the interface spin moment

To have a clear physics picture about the interface spin structure, the magnitudes of the magnetization for the various layers were quantitatively estimated using the XMCD spin sum-rule [186] to obtain both the orbital (Eq. 5.1) and spin (Eq. 5.2) components in the unit of μ_B/atom, using following equations:

$$m_{orb} = -\frac{4\int_{L_3-L_2}(\mu_+ - \mu_-)\,d\omega}{3\int_{L_3+L_2}(\mu_+ + \mu_-)\,d\omega}(10 - n_{3d}), \tag{5.1}$$

$$m_{spin} = -\frac{6\int_{L_3}(\mu_+ - \mu_-)\,d\omega - 4\int_{L_3+L_2}(\mu_+ - \mu_-)\,d\omega}{\int_{L_3+L_2}(\mu_+ + \mu_-)\,d\omega}(10 - n_{3d})(1 + \frac{7\langle T_z\rangle}{2\langle S_z\rangle})^{-1}. \tag{5.2}$$

where $\mu_+(\mu_-)$ is the absorption intensity with left (right) circular polarized x-rays, n_{3d} is the number of $3d$ electron per cation, which could be estimated as the nominal number of $3d$ electrons in the compounds, 5 (3.7) for Fe (Mn) in the current system. $\langle T_z\rangle$ is the expectation value of the magnetic dipole operator and $2\langle S_z\rangle$ is the value of m_spin in Hartree atomic units, which could be omit during the calculation, since the contribution of $(7\langle T_z\rangle)/(2\langle S_z\rangle)$ is very small (few %).

Figure 5.9 shows the integration for the XAS and XMCD spectra. The photon incident angle (30°) and the degree of circular polarization (70%) have been taken into account by multiplying μ_+ and μ_- by $[1/\cos(30°)]/70\%$. First, as a validity check, the magnetization of the Mn in the LSMO layer is calculated from the Mn-XMCD signal. We have found that the spin and orbital components of the magnetization are calculated to be ~ 3 μ_B/Mn and 0.14 μ_B/Mn, respectively. We note that within the limit of the uncertainties in the sum rule estimation process for low $3d$ metals, the calculation values are in great consistent with the magnetization measurements on LSMO ultra thin film as shown in Figure 5.7, while it is about 10% larger than the magnetization of LSMO/BFO films as measured by SQUID. The magnetization of the BFO layer at the interface was obtained using a similar method as for the LSMO layer. However, the resulting spin and orbital moment of 0.63 μ_B/Fe and 0.09 μ_B/Fe, respectively for Fe are likely underestimated, considering the relatively small magnetic moment (~ 0.03 μ_B) of BFO thin film, which also contribute to the measured XMCD.

Moreover, since the TEY mode used is an interface sensitive probe, detailed studies of the TEY will provide us more information about the spin-structure across the interface. In TEY mode, the x-ray only probes the top layer of the thin film, with

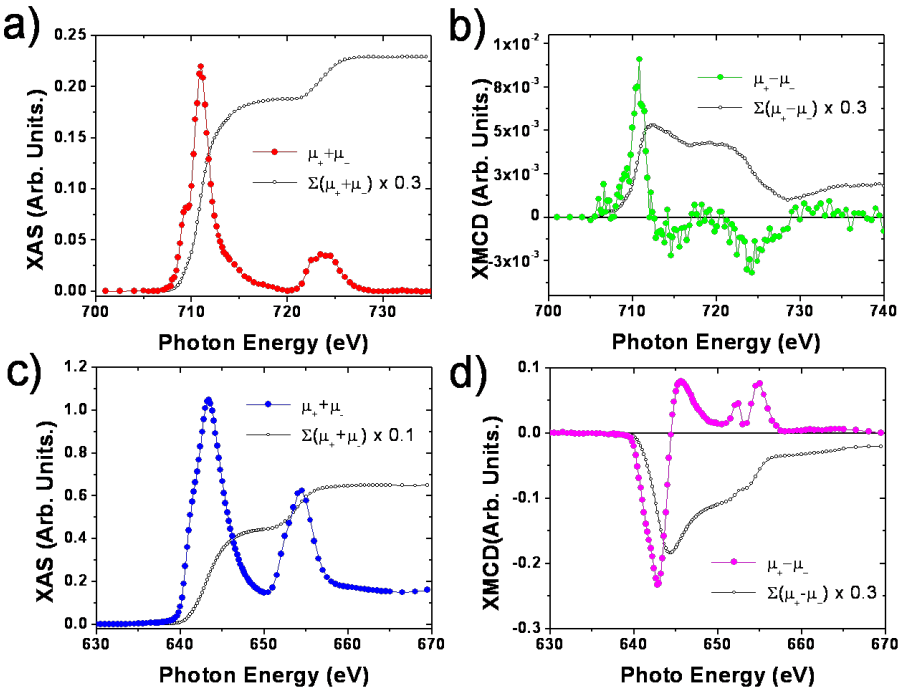

Figure 5.9: The XAS (a,b) and XMCD (c,d) integration applied in sum-rules calculations for Mn and Fe respectively.

the total electron escape profile described as [187]:

$$I(x) = I_0 \exp(-x/x_0) \tag{5.3}$$

where x_0 is the escape depth, which is the mean scattering path of the electron in the material. For LSMO, the escape depth is found to be around $\sim$ 5 nm. [188] While, to the best of our knowledge, we could not find published values for escape depth from BFO. So in our simple estimation, we have used the escape depth ($\sim$ 3.5 nm) measured for another similar canted antiferromagnetic iron compound, α-Fe_2O_3. [189] Based on these parameters, the ratio between the total electron yield (TEY, I(x)) to the total excited electrons (I_0) could be descried based on the Figure 5.10. If we choose 10% as a cutoff for the TEY signal, then the TEY measurement would be only sensitive to the $\sim$4 nm interfacial region of BFO, in addition to the 5nm of the LSMO that is above the BFO layer (i.e., a total TEY layer thickness of $\sim$9 nm). Thus, based on this first order estimation, the contribution to the Fe-XMCD should be mainly coming from this 4nm layer at the interface to the LSMO.

To estimate the spin moment of this 4 nm interfacial layer, detailed information about the profile of the spin moment is indeed needed, which, however, out of reach of current measurements. Since the magnetization behavior of Fe is mainly an interface effect, it is reasonable to assume an exponential decay of the magnetization away

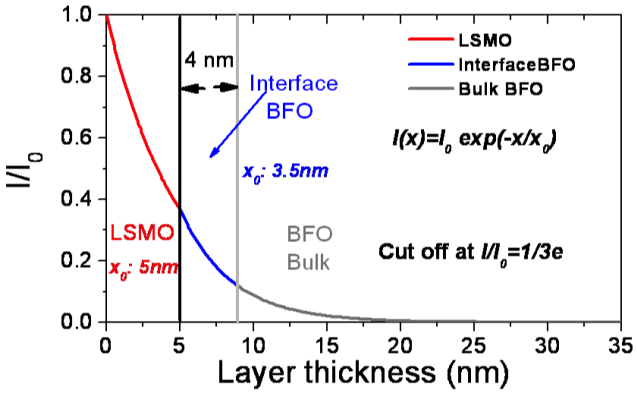

Figure 5.10: Total Electron Yield (TEY) intensity profile for the LSMO/BFO heterostructure with 5 nm LSMO and 30 nm BFO layers.

from the interface on the BFO side. To give an approximate description, a profile with exponential decay is assumed [16]:

$$m(x) = m_0 \exp(-(x-5)/x'); 5nm \leq x \leq 9nm. \tag{5.4}$$

where x' is chosen as 2 nm. (We note that the choice of the spin profile here is arbitrary, and further studies such as polarized neutron diffraction and theoretical simulation/calculation are needed to get a clear picture about this.) Then the TEY intensity from Fe L edge can be estimated as:

$$I_1 = I_0 \exp(-5/5) \int_5^9 \exp(-(x-5)/3.5)\, dx; \tag{5.5}$$

As a consequence, the TEY intensity coming from the spin polarized Fe can be expressed as:

$$I_2 = I_0 \exp(-5/5) \int_5^9 \exp(-(x-5)/3.5) \exp(-(x-5)/2)\, dx; \tag{5.6}$$

Since $I_1/I_2 = 2.38/1.22 = 1.95$, the spin and orbital moment at the interface could be estimated as $1.2\mu_B$/Fe (1.95×0.63 μ_B/Fe) and $0.2\mu_B$/Fe (1.95×0.09 μ_B/Fe) respectively. We note that this estimation will change with the value of x'; so, if x' is 4 nm, the moment is accordingly smaller, with spin and orbital moments are estimated to be $0.9\mu_B$/Fe and $0.1\mu_B$/Fe respectively. We reiterate that the exact value of the moment is not the central finding in this study; what is central is that there is a significantly enhanced moment compared to the bulk, canted moment ($\sim$ 0.03 μ_B/Fe), which is beyond the detection limit of current XMCD measurements, and the interfacial moment is antiferromagnetic coupled to the LSMO bulk spins and localized near the interface, which, moreover, is responsible for the exchange-bias coupling observed in the LSMO/BFO heterostructure.

5.4 Orbital reconstruction and magnetic coupling across the interface

In the previous two sections, we have studied the interface ferromagnetism in the BFO layer at the interface with LSMO. In this section, we would like to go one step further to answer the following questions: what is the origin of the interface ferromagnetism, and what is the underlying physics involved for the AFM coupling between the interfacial BFO and bulk LSMO spins?

We note that in transition metal oxides, the magnetic coupling between the metal ions is mainly determined by the occupancy of d orbitals. [114] In order to study the orbital structure information at the interface, the oxygen K-edge spectra were measured with both in-plane and out-of-plane linearly polarized x-rays. The difference between the XAS spectra with different linearly polarized x-rays is called x-ray linear dichroism (XLD), which could provide direct information of the $3d$ electron orbital polarization in the transition metal oxides. [53] During the measurement, the polarization directions of the linearly polarized x-rays (98 % polarized) are tuned by rotating the x-ray incident angle, with 90° and 30° corresponding to complete in-plane (E//a) and majority of out-of-plane (E//c) polarized component, respectively, as shown in the inset of Fig. 5.11.

Figure 5.11a shows the polarized XAS of the oxygen $K-$edge for the LSMO/BFO heterostructure. In contrast with the higher energy region (s, p characters of metal elements), the lower energy region (O $2p$-Mn (Fe) $3d$) reflects a strong dependence of the spectra on the linear polarization directions of incident x-rays. To investigate the hybridization process, temperature dependent studies of the linearly-polarized XAS were performed as shown in Figs. 5.11b,c. Since the TEY signal comes from approximately the top 5-10 nm of the sample, the overall spectra are similar to that of the reference pure LSMO (top layer); however, the spectra also reveal information about the near-interface BFO. For example, the feature around ∼530 eV (labeled as P_{1a} and P_{1c}) corresponds to a mixture of Fe (t_{2g} orbital) and Mn (t_{2g} and e_g orbitals) states, while the feature located at $\sim$ 532 eV (labeled as P_{2a} and P_{2c}) is related to only the e_g levels of BFO (green curves in Figs. 5.11b,c). By following these features as a function of light polarization direction (in-plane and out-of-plane), we obtain insight into the electronic orbital structure of the BFO at the interface. Figure 5.11d shows the temperature dependence of the peak positions of both the P_1 and P_2 features deduced from Fig. 3b,c. With changing temperature (from 300 K down to 10 K), the P_{1a} (red), P_{1c} (blue) and P_{2a} (green) features show a slight blue shift of the peak positions, due to a localization of the band at the low temperature. On the other hand, a dramatic change for the spectra measured by out-of-plane polarized x-rays (E//c) is observed (see purple curve in Fig. 5.11d). The clear red shift of the peak position of the P_{2c} feature ($d_{3z^2-r^2}$ orbital) suggests that normal to the interface a strong hybridized state between LSMO and BFO $d_{3z^2-r^2}$ orbitals via oxygen $2p$

orbital is formed below ∼100 K. Again, the similar temperature dependence between the hybridization effect (i.e., the position of the O K-edge in the BFO and LSMO, Fig. 5.11d) and the induced magnetization (as well as the EB effect) all point to a direct correlation between these observations and an electronic orbital reconstruction at the interface.

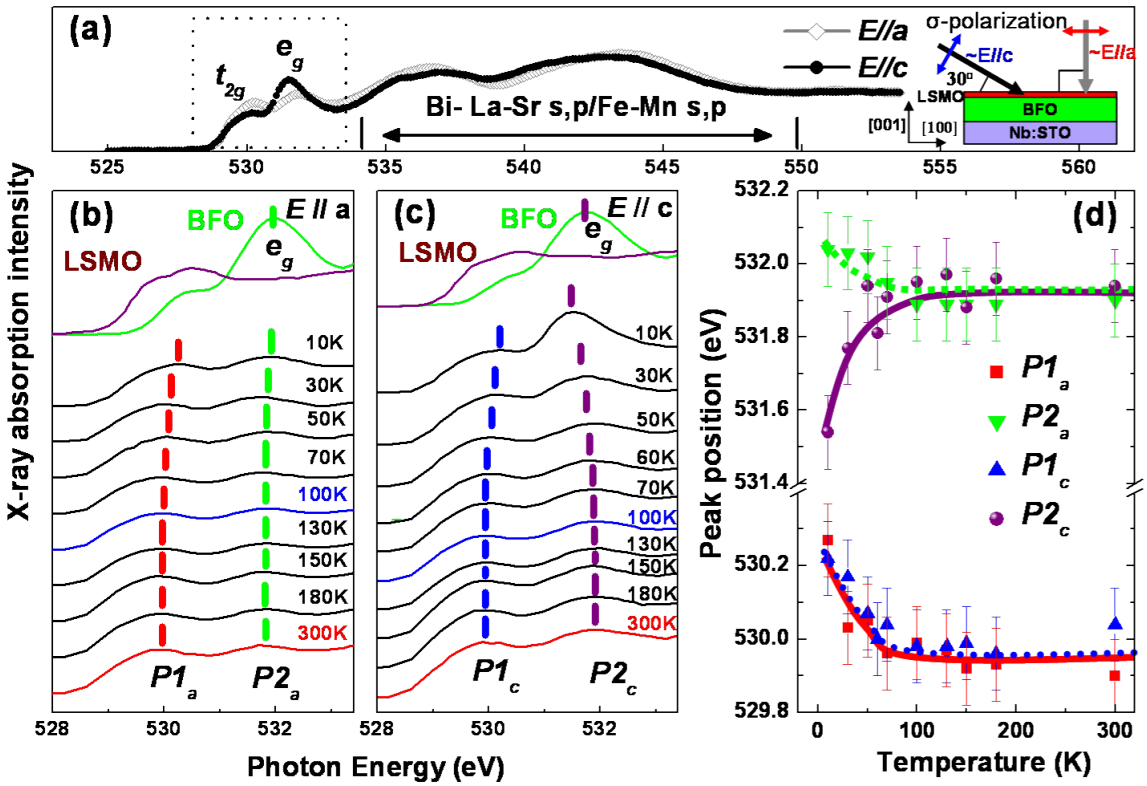

Figure 5.11: Probing hybridization effect by oxygen $K-$edge linearly polarized x-rays spectroscopy. (a) Polarization dependent oxygen K-edge XAS spectra with linearly polarized x-rays in wide energy range at T=10 K. Temperature dependent measurements of the polarized XAS spectra with polarization direction in-plane (b) and out-of-plane (c) for the specified bonding region of O 2p-Mn (Fe) 3d. (d) Temperature dependence of peak positions of interface orbitals. The red shift of orbital indicates the strong hybridization between Mn and Fe across the interface.

We note that the linear dichroism signal could originate from both magnetic (spin) [190] and electronic (orbital) [53, 191] anisotropy. To exclude the contribution of the magnetic anisotropy from the induced magnetism, data shown in Figure 5.11 were taken without magnetic field, while comparison with the results taken with an applied magnetic field (0.2 T) has also been shown in Fig. 5.12. It is clear that no change of the spectral shape or peak position was observed between with and without applied magnetic field. Thus, the contribution of the Fe ferromagnetic ions to the linear

dichroism could be neglected. Furthermore, the magnetic Curie temperature of LSMO (300 K) and Néel temperature of BFO (643 K)) in our samples, LSMO/BFO//STO, are well above the transition temperature (100 K) we observe in the XLD, XMCD and exchange-bias experiments. Hence, the temperature dependence of the O K-edge linear dichroism in our samples cannot be attributed to the magnetic anisotropy or orbital anisotropy that develops with the Curie (LSMO) or Neel (BFO) transitions. Therefore, we attribute the energy shifts in the spectra primarily to a hybridization effect, possibly originating from an orbital reconstruction.

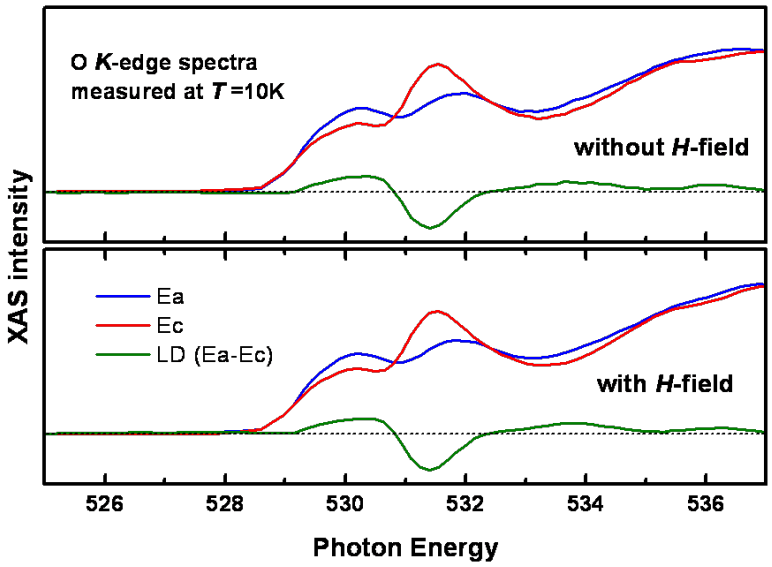

Figure 5.12: Comparison between the XAS and XLD of oxygen $K-$edge taken with (0.2 T) and without applied magnetic field. Measurements were carried out at 10 K with the magnetic field direction parallel to the film plane [100] axis.

We now focus on bringing these experimental observations (XMCD and XLD) together to help explain the origin of ferromagnetism in the BFO layer at the interface as well as the resulting exchange-bias coupling. The hybridization between the $d_{3z^2-r^2}$ orbitals of Fe and Mn at the interface will modify the energy state and break the degeneracy of the Mn $d_{x^2-y^2}$ and $d_{3z^2-r^2}$ orbitals as well, as illustrated schematically in Fig. 5.13a. Due to the strong hybridization effect, the energy levels of the bonding orbital will be pushed lower, while the energy level of anti-bonding orbital will be pushed higher by a similar amount. The energy level of the $d_{x^2-y^2}$ orbitals in the Fe and Mn will not be significantly influenced due to the small coupling strength between them. [192] Before taking into account the hybridization, the prerequisite of Fermi energy continuity at the interface suggests a possible energy alignment as shown in

Fig. 5.13a, in which the energy level of BFO is lower than that of LSMO due to the insulating nature of BFO and metallic nature of LSMO. After the hybridization, the electrons in the$d_{3z^2-r^2}$ orbital states will occupy the lower energy bonding orbital (which is confirmed by the oxygen $K-$edge study as shown in Fig. 5.11), while the electron at the Mn site will take the $d_{x^2-y^2}$ orbital state since this energy level is lower than that of the anti-bonding $d_{3z^2-r^2}$ orbital state. As a consequence, $d_{x^2-y^2}$ orbital ordering will be favored at the interface for LSMO.

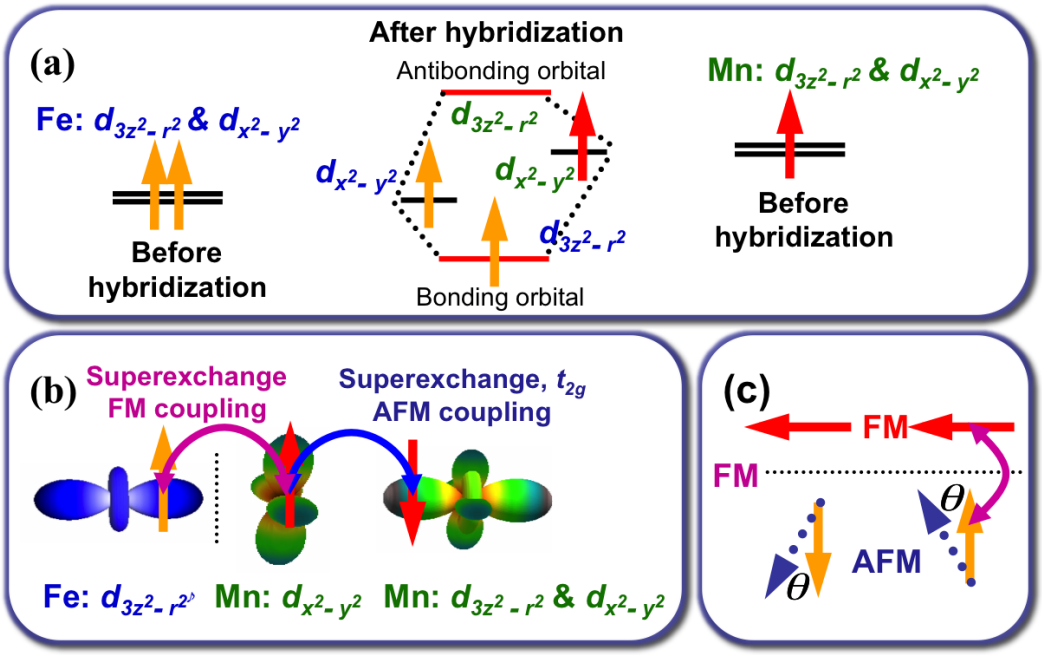

Figure 5.13: Schematic of the hybridization induced orbital reconstruction and the corresponding spin configuration at the interface. (a) Schematic of the interface electronic orbital reconstruction, with hybridization. orbital ordering will be formed at the interface for LSMO. (b) Proposed interface spin configuration and coupling mechanism with orbital ordering in the interfacial LSMO. The superexchange interaction between Fe and Mn ions is ferromagnetic, while the coupling between 1^{st} Mn and 2^{nd} Mn layer is antiferromagnetic due to the superexchange interaction between t_{2g} spins. (c) Schematic of the origin of the interface magnetism. The competition between the ferromagnetic coupling across the interface triggered by the orbital order and the antiferromagnetic ground state of bulk BFO leads to a frustrated spin state with a large canting angle.

Armed with the information of the orbital structure at the interface, we now turn to the magnetic coupling mechanism at the interface. From the Goodenough-Kanamori-Anderson (GKA) rules [24, 25, 27], the superexchange coupling between Fe^{3+} and Mn^{3+} (with $d_{x^2-y^2}$ orbital ordered in-plane, Fig.5.13b) and Fe^{3+} and Mn^{4+} both expected to be strongly ferromagnetic, mainly because there is essentially a low energy cost to excite an electron from the $d_{3z^2-r^2}$ orbital in Fe to an empty $d_{3z^2-r^2}$

orbital in Mn when its spin is parallel to the t_{2g} spins in both Fe and Mn. Moreover, the $d_{x^2-y^2}$ orbital ordering naturally leads to the antiferromagnetic coupling between the interfacial Mn layer and its neighboring Mn layer via the superexchange interaction between neighboring t_{2g} spin and oxygen $2p$ orbital, which is responsible for the $A-$type (planar) antiferromagnetic ordering in metallic manganites such as $Pr_{1/2}Sr_{1/2}MnO_3$ and $Nd_{1/2}Sr_{1/2}MnO_3$ [193]. Fig. 5.13b leads to the conclusion that the interfacial Fe spins and the Mn spins in bulk LSMO region are coupled antiferromagnetically, as is experimentally observed, in Figs. 5.5 and 5.8.

Having established this, we now examine the spin structure, in the BFO near the interface. Fig. 5.13c schematically describes the spin structure at the interface in the LSMO and the BFO layers. The competition between the ferromagnetic coupling across the interface is triggered by the orbital order (Fig. 5.13a,b), and the antiferromagnetic ground state of bulk BFO leads to a frustrated spin state with a large canting angle, Fig.5.13c. The magnitude of the canting angle is thus directly controlled by the strength of the interface coupling, while in the current study, the strong magnetic coupling between Fe and Mn at the interface due to the orbital ordering of LSMO would induce strong canting (magnetic moment) at the interface of BFO. We speculate that the EB effect is caused by the antiferromagnetic coupling between the interfacial Mn and the second Mn layers together with the induced moment in BFO. However, the induced moment in BFO must be pinned by additional mechanism such as the spin anisotropy [168] in BFO or the interface roughness [160], which may cause a complicated magnetic domain structure. Clarifying such a microscopic structure is an important future direction.

5.5 Conclusions

To summarize, we have shown that at the interface between LSMO and BFO a new magnetic phase has been induced as a consequence of the electronic orbital reconstruction. This magnetic state directly influences the exchange-bias coupling between the BFO and the LSMO upon freezing in at low temperatures and produces the pinned, uncompensated spins required for EB. Finally, we emphasize that changing of the interface electronic state (electronic doping level of Mn ions) by simply switching the polarization direction could in-principle modulate the interface magnetic coupling and eventually enable control of the magnetic state of ferromagnet LSMO, which is the main focus of next chapter.

Chapter 6

Magnetoelectric coupling at BFO/LSMO heterostructures

6.1 Motivation: a new approach for electric-field control of magnetism via exchange-bias coupling

Recently, there have been significant efforts to electrically control the magnetization of ferromagnetic thin films, since the associated magnetoelectric coupling has great potential for applications in data storage, sensors, and spintronics. [17,61,62,64] One key pathway to obtain the magnetoelectric coupling is through multiferroic materials, which show both ferroelectric (FE) and ferromagnetic (FM) spontaneous orderings. [57, 58] However, the mutually exclusive of materials constrains for FE and FM order parameters have led to the rarity of multiferroic materials, and hindered the progress of the magnetoelectric study. [66] Nevertheless, it is worth to pointing out that there has been significant progress in direct single phase magnetoelectric coupling in multiferroic materials. [57–60,63,65] For example, Tokunaga *et al.* have shown electrical control of magnetization in domain walls of multiferroic $GdFeO_3$. [194] Although this is a significant achievement, the relatively small magnetoelectric coupling strength hinders it for practical applications. To overcome this issue, a unique method has been proposed to use indirect coupling through a heterointerface between a FE materials and a FM materials, in which the charge degree of freedom, i.e., electric polarization, is used to manipulate the ground state of the FM materials to achieve the magnetoelectric coupling. [17, 61, 62, 64] The discovery of room temperature multiferroic $BiFeO_3$ (BFO, both FE and antiferromagnetic (AFM)), however, gives the magnetoelectric coupling a new knob, in which the magnetoelectric coupling can be mediated through an intermediate AFM order parameter. [72] In this approach, a bilayer heterostructure consisting of a thin FM material and a layer of AFM/FE mul-

tiferroic is employed. The AFM order parameter in the multiferroic acts as a medium that indirectly couples the FM ordering of a FM thin film and the FE ordering of the multiferroic. [17] The coupling mechanism between the AFM and the FM is the so-called exchange-bias coupling, which introduces an unidirectional anisotropy to the spin. [96] While the magnetoelectric coupling could be achieved by using either the intrinsic coupling between AFM and FE or the control of the magnetic coupling between the FM and AFM with FE polarization. Controlling this exchange-bias coupling may allow for the manipulation of magnetization, by biasing at a magnetic field and electrically shifting the magnetic hysteresis curve beyond the coercive field in either direction. This behavior is shown schematically in Figure 6.1. An ideal candidate structure for this type of indirect coupling is the heterostructure of multiferroic (AFM/FE) BFO and ferromagnetic LSMO, which were previously mentioned to show significant exchange-bias coupling due to interfacial magnetism in the previous two chapters. [177] We note that the interface magnetism is strongly correlated with the interface electronic state (i.e. electronic doping level of Mn ions at the interface), thus it is promising to modulate the interface magnetic coupling and eventually enable control of the magnetic states of the ferromagnet by electrically control of the FE polarization in the BFO layer. [195]

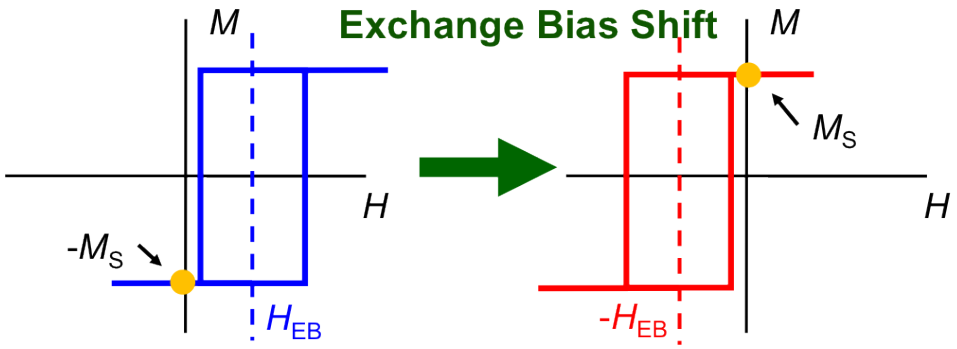

Figure 6.1: Schematic of proposed method to manipulate the magnetism through exchange-bias coupling.

6.2 Ferroelectric field effect transistor

In this chapter, an experiment has been conducted to test the proposed idea, i.e. electrically control of the magnetism, with a typical vertical ferroelectric field-effect transistor (FFET) device structure [196–199], in which the BFO layer is used as the FE gate to modulated the charge state at the interface with LSMO channel. The thin film heterostructure of LSMO and BFO was heteroepitaxially grown by pulsed-laser deposition on a $SrTiO_3$ (STO) (001) substrate, as discussed in great details in Chapter 2. For this study, since in the conventional exchange-bias system, the exchange-bias

field is inversely proportional to the thickness of FM layer [96], the LSMO layer was chosen to be $\sim$ 3 nm thick, in order to enhance the interface magnetic coupling effect (exchange-bias effect) while still remaining conducting. Figure 6.2 illustrates a schematic layout of the FFET device used in the study. In order to prevent the gate leakage due to the possible pinhole or any other leakage path in a precautionary manner, the BFO layer used in the study was chosen to be $\sim$ 600 nm thick.

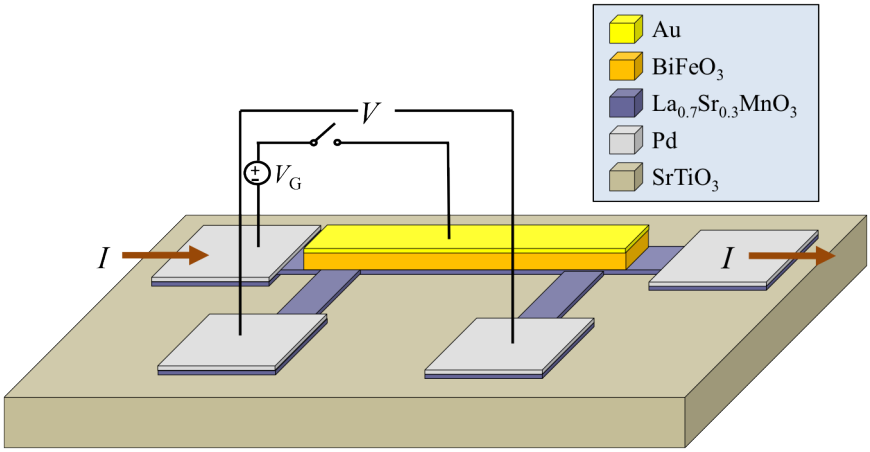

Figure 6.2: Schematic of the ferroelectric field-effect transistor made with BFO and LSMO layers. To change the BFO ferroelectric polarization, a pulsed voltage V_G is applied between the gate (Au) and the bottom contact (LSMO channel). The resistance of the LSMO channel is measured as a function of both the applied magnetic field, which is applied parallel to the current direction (in the device plane), and the gate voltage, which is applied perpendicular to the current direction across the gate structure.

Before the device fabrication, as-grown films have been measured with SQUID magnetometer. The measurements were carried out along [100] axis of the samples. Prior to the measurement, 1 T magnetic field is applied while cooling the sample from 350 K to 10 K for magnetic hysteresis measurements and to desired temperatures for temperature dependence measurements. Cooling the sample in positive magnetic field results in a negative shift of the hysteresis loop ($\sim$225 Oe) and vice versa, as shown in Figure 6.3a. Furthermore, from the temperature dependent measurements, the blocking temperature of this system was determined to be $\sim$100-120K, which nevertheless is consistent with our previous measurements shown in Chapters 4 and 5. This temperature sets an upper limit for the temperature where the device can be operated. After the fabrication, the ferroelectric polarization hysteresis loop was measured, which shows a clear electric polarization of BFO layer (Figure 6.3b).

With the initial characterization of both FE and exchange-bias coupling, we will go one step further to explore how we can combine these two aspects together to achieve the magnetoelectric coupling. In another word, whether we could use the electric-field control the magnetic state or the exchange-bias state in the current case? For the

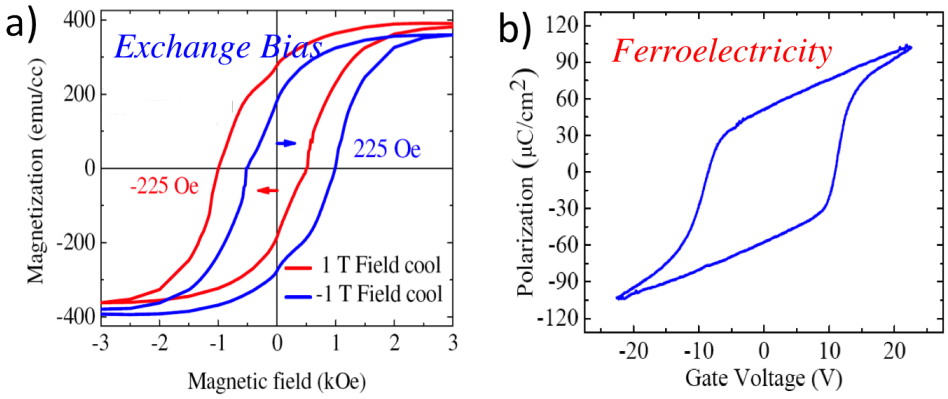

Figure 6.3: Ferroelectric and magnetic performances of the ferroelectric field-effect transistor. (a) Magnetic hysteresis curves of the BFO/LSMO/STO sample before device fabrication obtained from SQUID measurements made at 7 K. Curves are shown for measurements after field cooling process from 300 K to 7 K with +1 T (red) and -1 T (blue) magnetic field. (a) Ferroelectric hysteresis loop of the same sample after the device fabrication. Measurements were carried out with the external voltage bias applied between the gate contact (Au) and the conducting LSMO layer.

typical FFET device structure as shown in this study, the first order effect one would expect is the influence of the ferroelectric polarization on the sheet resistance of the conducting LSMO layer. [196–199]

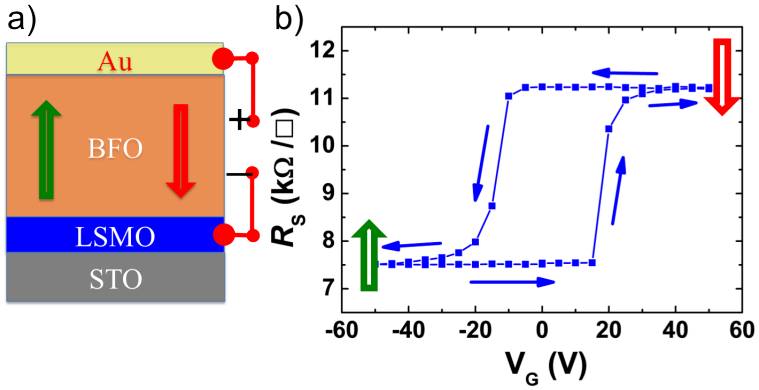

Figure 6.4: Hysteresis of the channel resistance in LSMO layer with respect to the gate voltage. (a) Schematic of the BFO/LSMO field-effect device. (b) The resistance of the LSMO channel as a function of the gate voltage, which is applied perpendicular to the current direction across the gate structure. The data were obtained at 5.5 K. The arrows show the direction of the pulse sequence.

The resistance of the LSMO channel was further measured as a function of applied gate voltage, which forms a nice square hysteresis loop, as shown in Figure 6.4. The

arrow on the curve shows the direction of the pulse sequence. Two distinct resistant states are formed depending on the polarization directions. For V_G pulses greater than 17 V, the sheet resistance obtains an upper saturation value of 11.2 kΩ/□ and for V_G less than -17 V, it exhibits a lower saturation value of 7.5 kΩ/□. Moreover, the switching voltages of (+/- 17 V) are consistent with the electric coercive field obtained from the ferroelectric hysteresis loop measurements, suggesting the fact that the electronic state of the conducting channel LSMO layer is indeed tunable with the applied electric field through the ferroelectric polarization.

6.3 Electric-field control of magnetic coupling across BFO/LSMO heterointerfaces

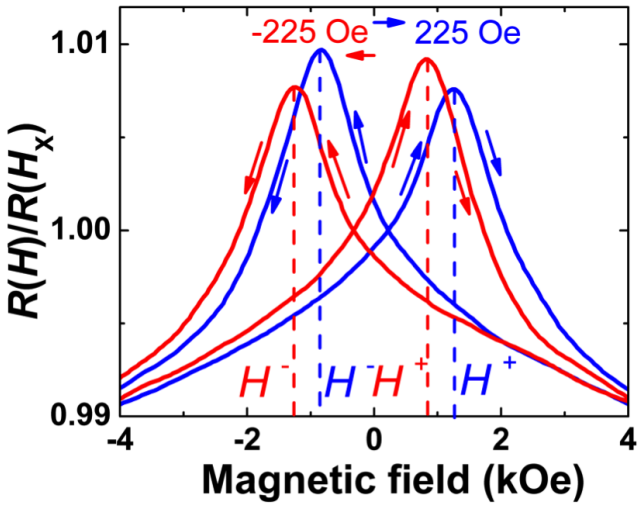

Figure 6.5: Typical magnetoresistance curves of the BFO/LSMO heterostructure after field cooling. The magnetotransport measurements were carried out after field cooling from 185 K in +1T (red) and -1T (blue). Resistance is normalized to the value of the resistance at the point where the hysteretic MR curve crosses. The double peaks of the MR curves are corresponding to the coercive fields obtained from SQUID measurements. An exchange-bias field of ±225 Oe is observed at the measurement temperature of 7 K.

With the initial characterization of the device completed, we then studied the effect of BFO polarization on the magnetic coupling through the heterointerface. To do this, magnetic hysteresis loops were obtained using the magnetotransport, which were measured for the voltage-pulse sequence at 7 K. This temperature was chosen to be well below the blocking temperature to maximize the magnitude of exchange-bias field. The sample was mounted in a low-temperature vacuum probe with the ability to apply variable magnetic field parallel to the sample plane. For comparison

of the magnetic transport to the magnetometry measurements, magnetoresistance (MR) was measured by sweeping the magnetic field between ±10 kOe parallel to the direction of the electric current, as shown in Figure 6.5.

The data exhibit hysteresis when measured along the [100] axis of the LSMO layer. In this set of data, the location of the positive (negative) peak corresponds to the positive (negative) coercive field, H_+ (H_-). Thus, the coercive field (H_C) could be defined as $H_C = (H_+ - H_-)/2$, which is the half distance between the two peaks. Similarly, the exchange-bias field (H_{EB}) is defined as the magnitude of the shift of the peak from zero, $H_{EB} = (H_+ + H_-)/2$. For positive and negative field cooling, we have obtained essentially identical values of both the coercive and exchange-bias fields to those measured with a SQUID magnetometer, as shown in Figure 6.3a.

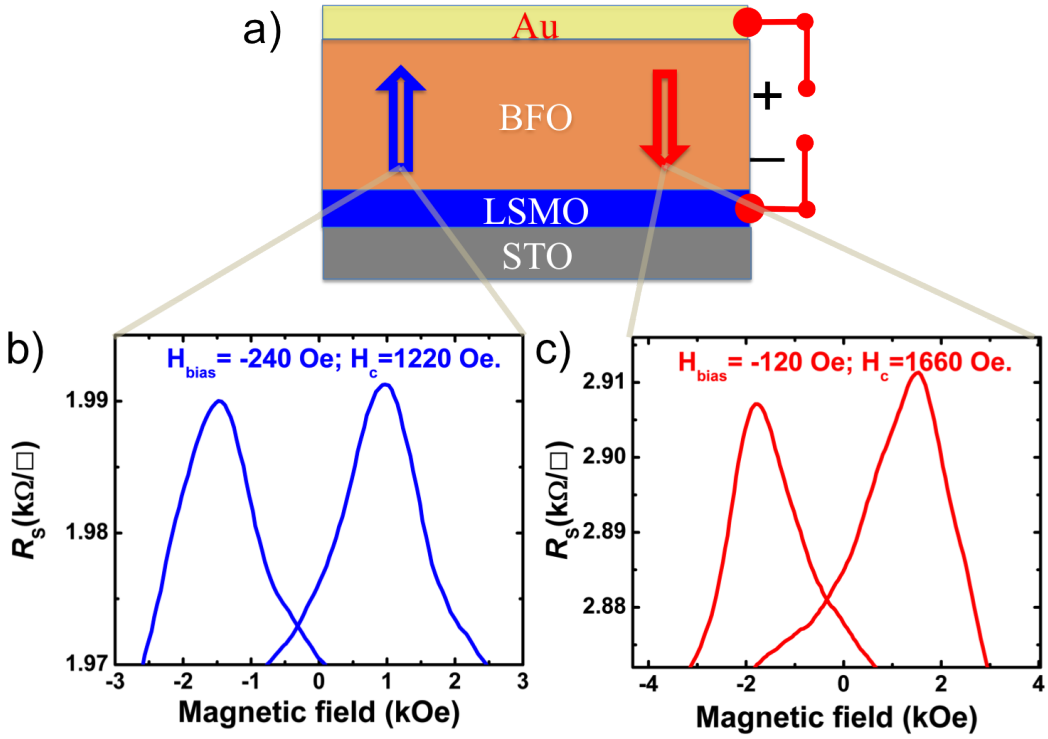

Figure 6.6: Ferroelectric polarization modulation of the magnetic coupling between BFO/LSMO heterointerface. (a) Schematic of ferroelectric switch in the FFET and corresponding magnetoresistance curves (b,c) measured with upward (b, blue) and downward (c, red) ferroelectric polarization states. The measurements were carried out at 5.5 K.

To study how the ferroelectric polarization could be used to manipulate the magnetic coupling across the heterointerface and the corresponding magnetoelectric effect, ± 60 V (V_G) external pulse voltages (with 10 ms pulse widths, which are large enough to fully saturate the BFO ferroelectric polarization) are employed to switch the ferroelectric polarization between two opposite directions. We note that during

the ferroelectric switch, the magnetic field is set to zero. To obtain the information about the coercive field and the exchange-bias field of the heterostructure, we have measured the magneto-transport across the LSMO layer for polarization upward and downward states respectively, shown in Figure 6.6. For polarization upward state, the coercive and exchange-bias fields are measured to be around 1220 Oe and 240 Oe, respectively. On the other hand, very different magnetic anisotropy was obtained for the polarization downward case: with the enhancement of coercive field (1660 Oe) and suppression of exchange-bias field (120 Oe).

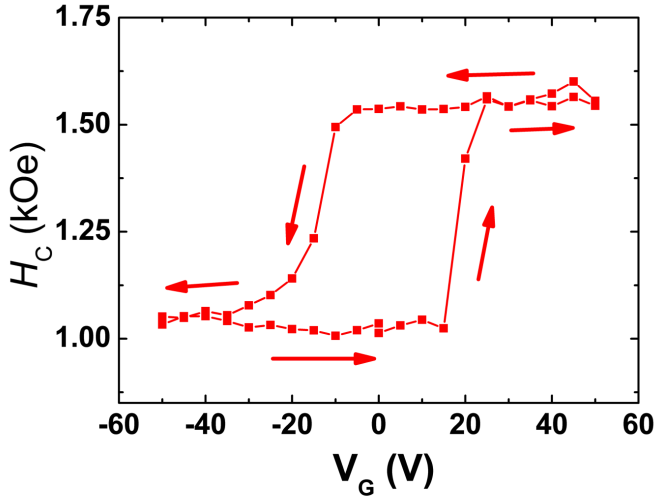

Figure 6.7: Hysteresis of the coercive field of the LSMO layer measured with magneto-transport with respect to the gate voltage. The measurements were carried out at 5.5 K.

To study the correlation between the change of magnetic anisotropy (coercive field and exchange-bias field) and the ferroelectric polarizations, we have also studied the magnetic coercive field of the LSMO layer as a function of external voltage applied through the BFO gate. Like the R_S-V_G curve, a distinct hysteresis loop was obtained from the measurement, showing the saturation values at 17 V and -17 V of 1550 Oe and 1000 Oe, respectively. The similarity between the magnetic coercive field and the ferroelectric polarization strongly indicates the causal relationship between the ferroelectric polarization and the magnetic anisotropy of the LSMO layer.

Furthermore, a pulse sequence, which alternates between the two ferroelectric polarization states after every five pulses, is employed to demonstrate the dynamics and reversible nature of this control, as shown in Figure 6.8a. The results of the electric-field control of the magnetic anisotropy (for both remnant magnetization polarities) are presented in Figures 6.8b and c, in which H_{EB} was normalized to the coercive field (H_{EB} /H_C) to eliminate complications that could arise from concurrent changes in the coercive field. Clearly, two very interesting aspects were observed

from this study. The first one is that H_{EB}/H_C can be modulated significantly by the application of an electric field, between high and low states that correspond to low and high resistances respectively. We would emphasis that this change is reversible with the application of electric field, requires no field cooling or any applied magnetic field during voltage pulses. The maximum exchange-bias modulation was $\sim$0.15 H_C, which corresponds to an exchange-bias field of $\sim$125 Oe. Secondly, we have observed in this system that the polarity of the exchange-bias field is always opposite to the remnant magnetization MR in LSMO layer before the gate pulse is applied. This remnant magnetization arises from the magnetoresistance sweep and can be set into either a negative or positive state, depending on the direction that the swept magnetic field approaches zero.

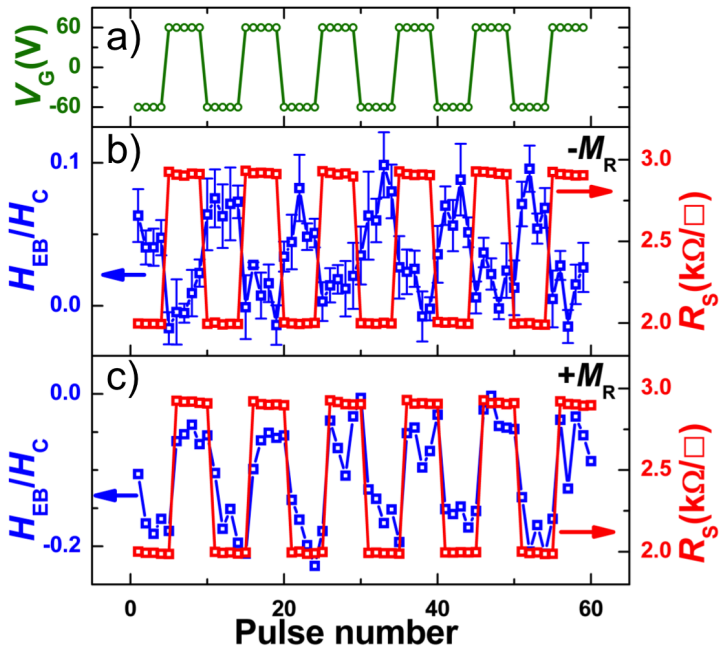

Figure 6.8: Dynamics reversible electric-field control of exchange-bias coupling. (a) The gate-voltage-pulse sequence used for the measurements. (b,c) Measurements of normalized exchange-bias field and channel resistance for the gate-pulsed sequence shown in (a). Each point is determined from an MR sweep at 5.5 K after pulsing the gate with gate voltage V_G (60 V). The exchange-bias coupling modulates with the ferroelectric polarization and also the initial magnetic state before the switch. The data shown for (b) were obtained with a negative remnant magnetization in the LSMO channel whereas the data shown in (c) obtained with a positive remnant magnetization. Error analysis was done on (b) by taking multiple MR sweeps. Standard deviations of the individual peak locations were obtained and the error was calculated for each point using standard error propagation techniques. Both measurements were taken without field cooling process.

Finally, at the end of this chapter, we would speculate on the possible mechanisms

for the electric field induced modulation of the magnetic coupling. Clearly, two steps are required for this understanding: the first is the origin of exchange-bias coupling in the BFO/LSMO heterostructure; the second is the consequent modulation of the magnetic state with an electric field.

Let us recall that in the previous chapter, using the x-ray magnetic circular dichroism, the formation of a novel interface ferromagnetic state was observed in the BFO layer at the interface. Temperature dependent measurements of this interface magnetism shows that it disappears by ∼100-120 K consistent with the blocking temperature of the exchange-bias field, measured with a SQUID magnetometry. This finding establishes a causal relationship between the induced interface magnetism and the exchange-bias coupling that results.

Armed with this insight, one can then look into the possible origin of the magnetoelectric coupling. Here we attempt to lay out and then comment some possible scenarios for the mechanism behind. The first possibility is the strain imposed on the LSMO layer due to the switching of the FE polarization through a magnetostrictive effect involving the BFO and LSMO interface. However, the strain is an equal polarity, thus the polarization upward and downward states should be degenerate. Moreover, two unit cells of non-magnetic STO inserted between the LSMO and BFO completely quenched the exchange-bias coupling despite the fact that the LSMO layer is still strained. The second possibility is the charge modulation imposed by the ferroelectric switch. The charge state at the interface can be modulated by the ferroelectric depolarization field with the the carriers (holes) in the LSMO moving closer or further from the interface, much like in two dimensional semiconductor systems. However, this argument is not sufficient to explain the effect observed here, because electric-field modulations of the exchange-bias field and coercive field are not observed in similar field effect devices made from $PbZr_{0.2}Ti_{0.8}O_3$/LSMO heterostructures. [88,89]

Thus, one would expected a more delicate model, which would invoke the atomic scale information across the interface, for example, the electronic state, chemical bond length, orbital occupation state, etc, which would be the focus of Chapter 7 in this dissertation.

6.4 Summary and implications of this work

In summary, using a field effect device employing multiferroic (FE/AFM) BFO as the dielectric and FM LSMO as the conducting channel, we have demonstrated a novel strategy of electrical control of the magnetism. We have shown that the magnetic coupling across the heterointerface can be reversibly switched between two distinct exchange-bias states by switching the FE polarization of BFO. This finding is an important step towards controlling magnetization with electric fields, which may enable a new class of electrically controllable spintronic devices and provide a new basis for producing electrically controllable spin polarized currents. Clearly, due to

the multiplicity of physical phenomena that are likely to be involved, further studies, especially the combination between the experimental results and theoretical models, are required to fully understand the phenomenon at hand. Furthermore, similar material systems need to be thoroughly investigated in order to find higher blocking temperatures to enable room temperature operation.

Chapter 7

Mechanism of magnetoelectric coupling

In the previous chapter, using magnetotransport, we have demonstrated the magnetoelectric coupling at the $BiFeO_3/La_{0.7}Sr_{0.3}MnO_3$ (BFO/LSMO) heterostructure, i.e. the magnetic state in the LSMO layer can indeed be controlled with ferroelectric polarization of the BFO layer. Here we demonstrate macroscopically the electric-field control of magnetic coupling across heterointerfaces of multiferroic BFO and ferromagnetic LSMO and unveil that both the lattice and charge degrees of freedom are strongly coupled with the interface spin interaction, thus providing the intriguing magnetoelectric coupling at the heterostructure. Moreover, by combining first-principle calculations and phenomenological model, we propose a microscopic model that explains the unique magnetoelectric coupling in the current system, in which, charge, spin, orbital and lattice degrees of freedom are all involved and interplay together to induced the exotic magnetoelectric coupling.

7.1 Ferroelectric polarization on the magnetic coupling

Figure 7.1 shows two possible atomic stacking sequences of BFO/LSMO heterointerfaces. Depending on the type of atoms sitting in between these two transition metal oxide layers (MnO_2 and FeO_2), two different interfaces could be formed and labeled as BiO and $La_{0.7}Sr_{0.3}O$ (LSO) interfaces. As discussed in chapter 3, high qualify heterointerfaces between BFO and LSMO could be engineered perfectly to atomic scale sharpness as designed by using reflection high-energy electron diffraction (RHEED) assisted pulsed-laser deposition (PLD). Moreover, the polarization order of BFO brings in another freedom and leads to totally four configurations, which we will explore individually in this chapter.

As stated in Chapter 4, exchange-bias coupling strengths are quite different be-

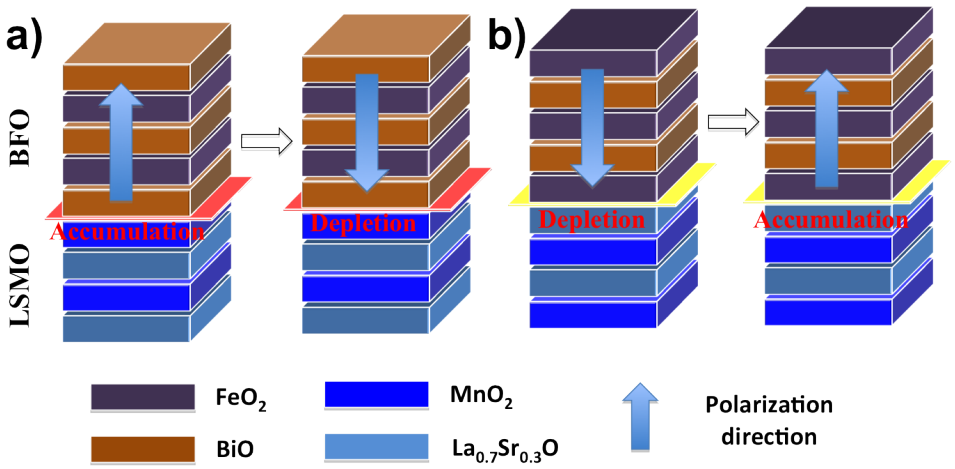

Figure 7.1: Atomic stacking sequence of the perovskite BFO/LSMO heterointerface for the magnetoelectric study. The fact that both LSMO and BFO are perovskite structures leads to two possible interface configurations, MnO_2-BiO-FeO_2 (BiO) interface (a) and MnO_2-$La_{0.7}Sr_{0.3}O$-FeO_2 (LSO) interface (b). The difference between these two interfaces is the termination of the LSMO layer during the growth, which is controlled by switching the termination of the STO substrates. This together with the polar nature of ferroelectric BFO leads to in total four possible configurations. The arrows indicate the ferroelectric polarization in BFO.

tween these two interfaces with as-grown ferroelectric polarization states. Thus, it will be very interesting to study the influence of ferroelectric polarization on the magnetic coupling, i.e. the magnetoelectric coupling, for both these two heterointerfaces. To do this, we have developed a technique, which can macroscopically switch the ferroelectric state of the thin films, with a schematic of the experimental setup shown in Figure 7.2. A metal probe with a dimensional of 50 μm diameter spherical tip is used, which leads to a tip-sample contact area of about tens of μm^2 and makes the macroscopic switch possible. During the switch process, a tip-relative-to-sample DC voltage of -/+ 5 V was applied, and the tip was scanned over the sample controlled by an x-y step motor stage with spatial resolution of 0.5 μm. The scanning was along the x-axis with 5 μm spacing per line, and the scanning speed is 40 μm/s. To prevent sample damage, the tip was kept soft contact with the BFO film through the whole process by using a balance sample stage. Due to the round-tip geometry, the poled region has a high coverage of the sample area, which is also confirmed by the randomly selective PFM testing with micrometer scales. Figure 7.3 shows out-of-plane PFM images of both MnO_2-BiO-FeO_2 (BiO) interface (a) and MnO_2-$La_{0.7}Sr_{0.3}O$-FeO_2 (LSO) interface (b) with as-grown states and the corresponding results after the macroscopic switch (c,d). The contrast of out-of-plane PFM images is correlated with the orientation of the ferroelectric polarization, with black (white) indicating upward (downward) ferroelectric polarization. Clearly, the as-grown ferroelectric polarization states are exactly oppo-

site, which is due to the induced interface electrostatic potential step, as we have discussed in details in Chapter 3. [127] As we expected, the contrasts of the PFM images after the macroscopic switch were reversed, with a ratio of the switching area is bigger than 96%, which validates the high efficiency of the macroscopic switch and makes subsequent measurements possible.

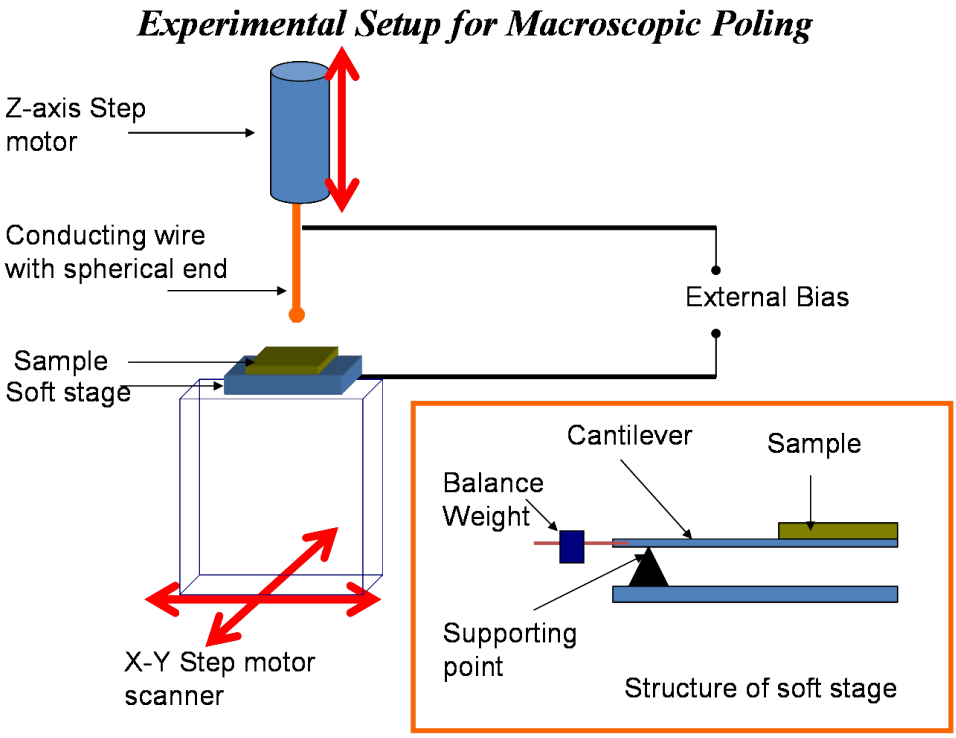

Figure 7.2: A schematic of the microscopic scanning metal-probe setup. The metal probe has a dimensional of 50 μm diameter spherical tip, which leads to a tip-sample contact area of about tens of μm^2 and makes the macroscopic switch possible.

Thus, instead of using in-situ microscopic switch and probing indirectly the magnetism using magneto-optic Kerr effect [88,89,97], photoemission electron microscopy [74], or magnetic transport [195], we can measure directly the macroscopic magnetism of the samples using a state-of-art magnetometer, MPMS SQUID. For identical samples, we compared the magnetic hysteresis loops measured before and after the ferroelectric polarization switch. Figure 7.4a shows typical results for the heterostructure with BiO interface. Clearly, three aspects could be observed from the measurement when the polarization state was switched from upward to downward: 1) enhancement of the saturation magnetization from 470 emu/cc to 530 emu/cc, which is further confirmed by temperature dependence measurements (Fig. 7.4b); 2) suppression of the exchange-bias field from 50 Oe to 20 Oe; 3) increase of in-plane spin anisotropy energy with the enhancement of coercive field from 200 Oe to 300 Oe. On the other

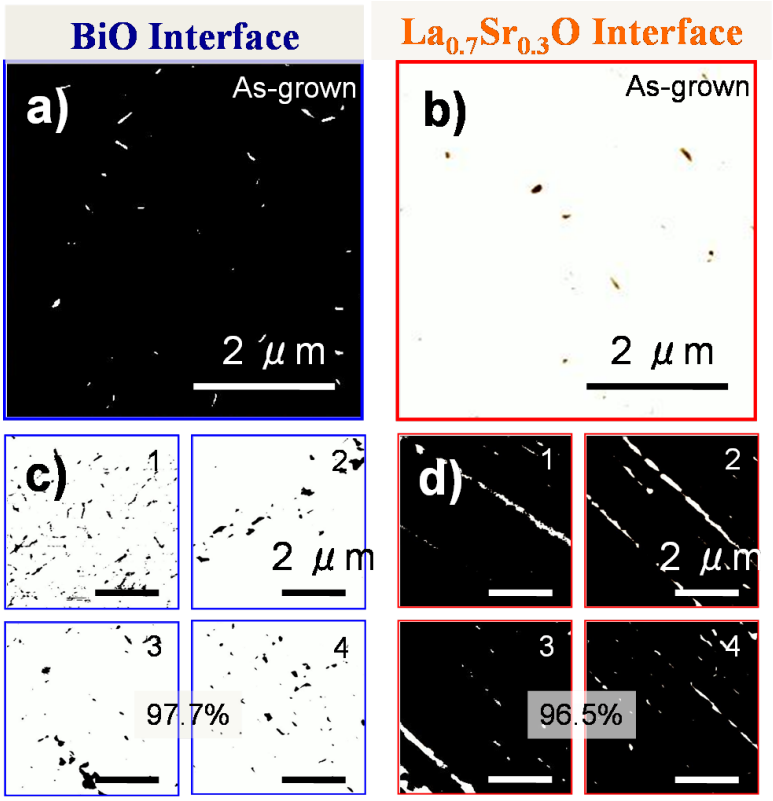

Figure 7.3: Macroscopic switch of the ferroelectric polarization. Out-of-plane PFM images of the as-grown states of MnO_2-BiO-FeO_2 (BiO) interface (a) and MnO_2-$La_{0.7}Sr_{0.3}O$-FeO_2 (LSO) interface (b), and the corresponding results after the macroscopic switch (c,d).

hand, exactly the same measurements on the LSO interface (Fig. 7.4c, 7.4d) reveal that polarization switch has an insignificant influence on any of these three aspects. The very different magnetoelectric couplings for the structures with different stacking sequence, again strongly suggest the importance of the local structure and electronic information. Finally, we note that the ferroelectric polarization switch of $PbZr_{0.2}Ti_{0.8}O_3$/LSMO heterostructure results in only the change of magnetization, but has insignificant influence on either exchange-bias or coercive field.

7.2 Mechanism of magnetoelectric coupling

Previous XMCD studies of LSMO/BFO heterostructures have shown an important role of interface orbital and spin structures to the exchange-bias coupling observed. Thus, to reveal the mechanism of the magnetoelectric coupling, the knowledge about the lattice as well as electronic structures across the interface will be necessary. We note that first-principle calculations have successfully predicted/explained the spin structures of the heterostructures of manganites with both ferroelectric

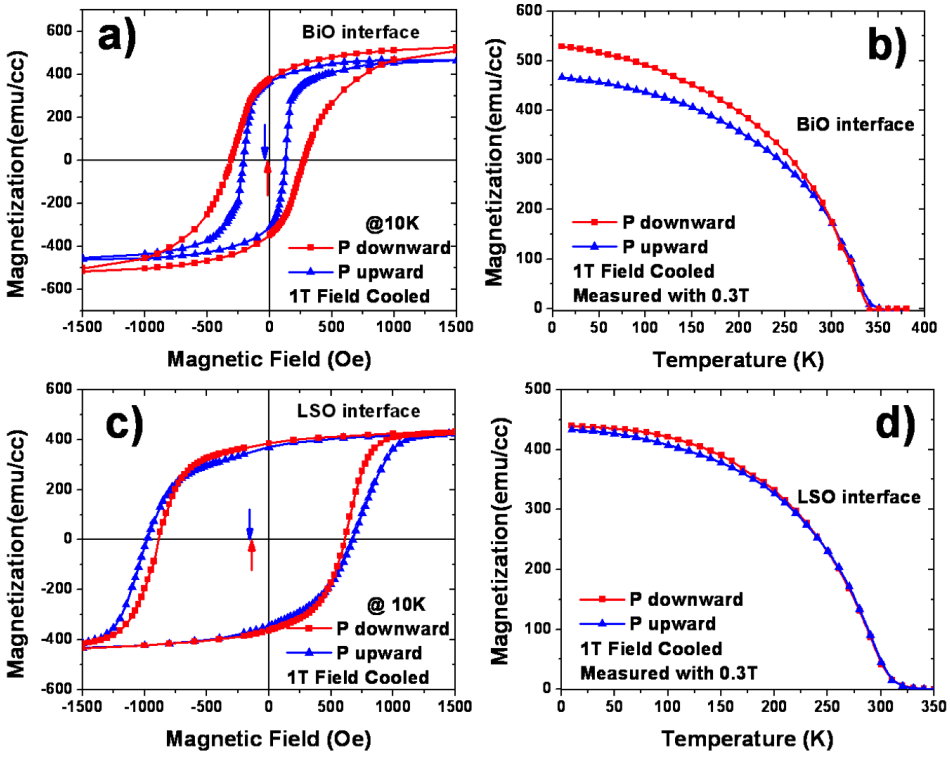

Figure 7.4: Magnetoelectric coupling across the BFO/LSMO heterointerfaces. The comparison of the exchange-biased hysteresis loops (a,c) and temperature dependence of magnetizations (b, d) with opposite ferroelectric polarizations for the heterostructures with BiO (a,b) and LSO (c,d) interfaces. The arrows label the center of the biased hysteresis loops. Dramatically changes of magnetization, exchange-bias field and coercive field were observed for the BiO interface with the ferroelectric switch. By contrast, for the LSO interface case, the polarization switch has an insignificant influence on the magnetic coupling. Such striking difference suggests again the important role of the local atomic structure for the magnetic coupling.

$BaTiO_3$ [87] and high temperature superconductor $YBa_2Cu_3O_{7-\delta}$ [200]. However, the complexity of the current BFO/LSMO heterostructure, in which, charge, spin, orbital and lattice degrees of freedom interplay strongly together, has prevented direct modeling of spin structures across such interface. Instead, a two-step approach is developed. First, we used first-principle calculations to obtain the atomic lattice and electronic structures across the interface. Then based on the result, a phenomenological model was employed to reveal the mechanism of the magnetoelectric coupling.

First-principle calculations were carried out for all four possible BFO/LSMO heterointerfaces (shown in Fig. 7.1), with the focus on the interface lattice (d, the lattice spacing between Mn and Fe ions across the interface) and electronic (valence state of interface Mn atomic layer) structures. We carried out first-principles density-

functional total-energy calculations using the projector augmented-wave method as implemented in the VASP code. The calculations were performed using the spin-polarized generalized-gradient approximation for the exchange-correlation potential. Super-cells were used consisting of an eight-unit-cell layer of BFO and an eight-unit-cell layer of LSMO. The interfacial atomic plane between FeO_2 and MnO_2 planes was chosen to be either BiO or $La_{0.7}Sr_{0.3}O$, to simulate the corresponding interfacial chemical compositions of the samples. The in-plane lattice constant was fixed to the STO lattice constant of 0.3905 nm, to simulate the epitaxial growth of BFO and LSMO on an STO substrate. The interface lattice spacing and valence states of Mn ions were obtained from the optimized atomic positions (Table 7.1).

Interface type	Polarization state	Interfacial Mn valence state	Mn-O-Fe spacing (nm)
LSO interface	Up	3.59	0.390
	Down	3.44	0.391
BiO interface	Up	3.53	0.393
	Down	3.18	0.405

Table 7.1: Lattice and electronic structures of the LSMO/BFO heterointerfaces from first-principle calculation.

For the BiO heterointerface, the lattice spacing changes by about 3% as the ferroelectric polarization switched from upward (pointing from LSMO layer) to downward (pointing toward the LSMO layer). In contrast, the lattice spacing at the LSO heterointerface is insensitive to the ferroelectric switching, which is, however, understandable by taking into account the fundamental important role of bismuth lone-pairs on the ferroelectricity in BFO. [125] For the LSO interface, the atoms between Fe and Mn are $La_{0.7}Sr_{0.3}O$, which is polar inactive compared with the BiO layer. As a result, the ferroelectricity at the interface will be quenched and form a so-called ferroelectric "dead layer", which is relatively insensitive to the polarization switch. Furthermore, the valence state of the interface Mn was obtained from valence bond theory. [201] As expected, for BiO interface, the valence state of the interface can be tuned between +3.18 (polarization downward) and +3.53 (polarization upward) due to the ferroelectric charge screening effect at the interface. By contrast, only a slight change of the valence state is observed for LSO interface. Such an insensitive response of both interface lattice and electronic structures to the ferroelectric switching strongly correlates with the insignificant magnetoelectric response at LSO interface.

Armed with the knowledge of both the atomic lattice and electronic structures across the interface, we propose the mechanism of the emergent magnetoelectric coupling observed in BiO heterointerface with phenomenological models illustrated in Figures 7.5 and 7.6. By taking into account the orbital nature at the interface, all of the three aspects of the magnetoelectric measurement can be qualitatively explained.

1) Total moment: For the polarization upward state, the valence state of interface Mn (+3.53) is near quarter filling, which intrinsically favors the planar orbital order. In addition, the suppression of the interfacial Mn-Fe spacing further stabilizes the $d_{x^2-y^2}$ orbital ordering at the interface to minimize the electron hopping to the neighboring Mn layer. As a consequence, the AFM superexchange (SE) interaction (Fig. 7.5a) between the nearest neighbor t_{2g} orbitals takes over the FM double-exchange (DE) interaction. [192] On the contrary, FM coupling (Fig. 7.5b) would persist for the polarization downward state since the valence states of the interface Mn ions are still in the FM range. The change of the adjacent Mn spins at the interface from parallel to antiparallel configurations could induce a change of total moment by $\sim$ 2/13=15%, which is profoundly consistent with our experimental results.

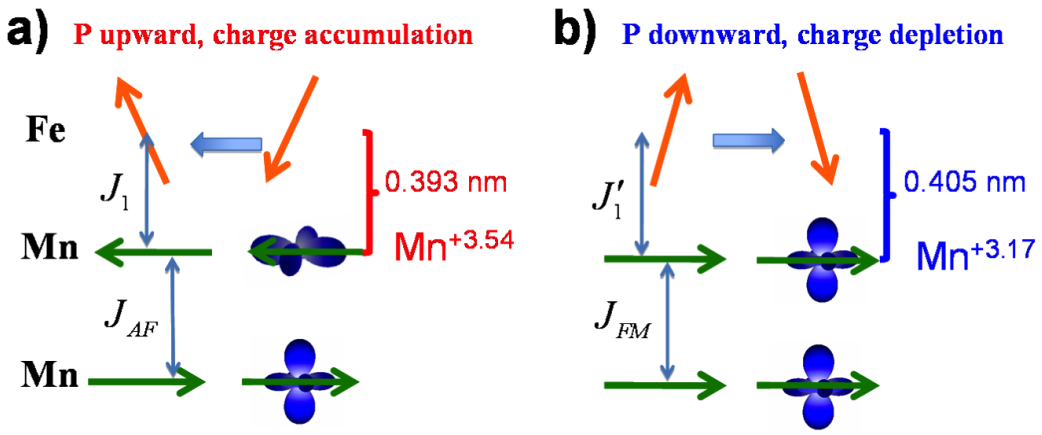

Figure 7.5: Schematic illustrations of the spin and orbital reconstructions across the BiO heterointerface. The lattice and electronic structures around the interface drives the orbital and spin reconstructions of interfacial Mn cations for polarization upward (a) and downward (b). The arrows indicate the spin orientation in the Mn (green) and Fe (yellow) cations.

2) Exchange-bias field: In the heterostructure of BFO/LSMO, the exchange-bias coupling is mediated through the FM SE coupling between Mn and Fe ions across the interface and the AFM SE (polarization upward) or the FM DE (polarization downward) between the interfacial Mn layer and adjacent Mn layer. For the polarization upward state with $d_{x^2-y^2}$ orbital order, the AFM SE interaction is the smallest interaction and, therefore, the dominant factor of the exchange-bias coupling observed. For the polarization downward state, the increased lattice spacing (d) between Mn and Fe ions is expected to suppress the SE coupling dramatically [114], while the coupling between Mn layers now became the strong FM DE. Thus the former (FM SE) dominates the exchange-bias field, and the amplitude of which is much reduced compared with that in the polarization upward state because the Fe-Mn hybridiza-

tion is suppressed and Mn $d_{3z^2-r^2}$ orbitals are partially occupied. As a consequence, the exchange-bias coupling for polarization downward case is smaller than that of polarization upward case.

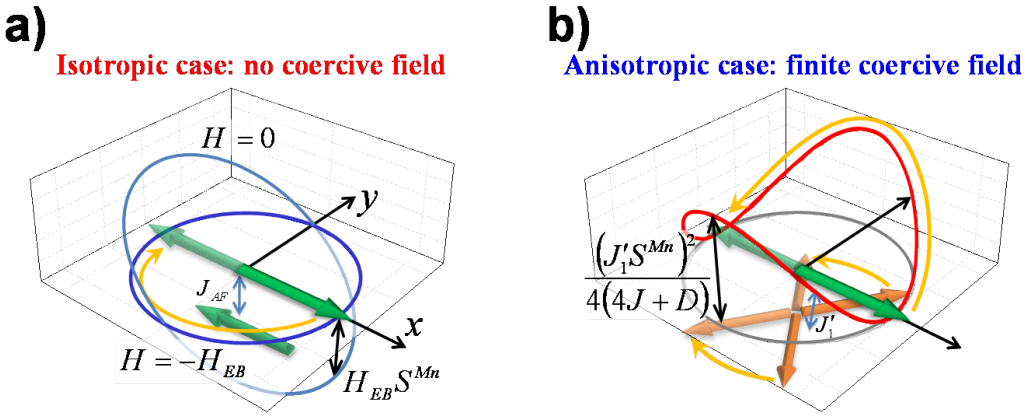

Figure 7.6: Contour plots of spin anisotropy energy at the MnO_2-BiO-FeO_2 (BiO) heterointerface. The profiles of spin anisotropy energy at the heterostructure interface for charge accumulation (a) and depletion (b) cases. For the charge accumulation case, the spin anisotropy energy is isotropic due to the collinear spin configuration. Thus, the spins could rotate coherently when the external field cancels the exchange-bias field and form square-like hysteresis loop with small coercive field. By contrast, the perpendicular spin configurations will result in a spin flop coupling and induces an anisotropic energy barrier for the spin rotation. As a consequence, relatively larger coercive field is brought about, and the hysteresis loop is less square-like.

3) Coercive field: The changing of in-plane anisotropy energy (coercive field) could also be attributed to the orbital reconstruction at the interface. We note that for polarization upward state, AFM SE interaction at the interfacial Mn layers is the dominated factor for the exchange-bias coupling. In this case, a collinear spin configuration is realized between the interfacial Mn and the adjacent Mn layer. The spin anisotropy energy is expected to be small (Fig. 7.6a) because the rotation of Mn moment does not accompany the additional motion of the interfacial collinear Mn spins, which are strongly coupled with the non-collinear Fe spins. On the other hand, for the polarization downward state, the SE coupling between the Mn and Fe across the interface becomes the dominant factor for the exchange-bias coupling. In such a perpendicular spin configuration, the rotation of the Mn moment accompanies the "flop" of the Fe spins. We consider a simple model in which a two-dimensional antiferromagnet (spin S^{Fe}, coupling constant J and uniaxial anisotropy D) is coupled with a two-dimensional ferromagnet with spin S^{Mn} with coupling constant J_{FM} via

weak ferromagnetic interactionJ_1'. Thus the Hamiltonian is given as:

$$H = \sum_{<i,j>\in x,y} (J\vec{S}_i^{Fe}\cdot\vec{S}_j^{Fe} - J_{FM}\vec{S}_i^{Fe}\cdot\vec{S}_j^{Fe}) - D\sum_{<i>\in x,y}(\vec{S}_i^{Fe})^2 - J_1'\sum_{i\in x,y}\vec{S}_i^{Fe}\cdot\vec{S}_j^{Mn}. \quad (7.1)$$

Here we assumed that the system is cooled under an applied field along the x direction, thus the spins in the antiferromagnet alternate with the local moment points along the $+y$ or $-y$ direction with the finite canted moment along the x direction in parallel with the ferromagnetic moment. Assuming that theJ_1' is much smaller than J, J_{FM} and D, and all spins are confined in the x, y plane due to the shape anisotropy, thus the mean field energy per site is given by:

$$\begin{aligned} E(\theta,\theta_1,\theta_2) = E_0 + J(S^{Fe})^2(\theta_1+\theta_2)^2 + \frac{1}{2}D(S^{Fe})^2(\theta_1^2+\theta_2^2) \\ +\frac{1}{2}J_1'S^{Fe}S^{Mn}[\frac{1}{2}\sin\theta(\theta_1^2-\theta_2^2) - \cos\theta(\theta_1+\theta_2)], \end{aligned} \quad (7.2)$$

with $E_0 = -(2J+D)(S^{Fe})^2$. $\theta_{1(2)}$ is the small deviation of spins from the $+(-)y$ direction in the antiferromagnet, and θ is the deviation of the ferromagnetic moment from the x direction. By minimizing the energy with respect toθ_1 andθ_2, one obtains the mean field energy as a function of the direction of the ferromagnetic moment as:

$$E(\theta) = E_0 - \frac{(J_1'S^{Mn})^2}{4(4J+D)}\cos^2\theta. \quad (7.3)$$

Clearly, the system will gain energy by introducing a finite canting in the antiferromagnet layer. As long as the antiferromagnetic ordering persists during the rotation cycle of the ferromagnetic moment, this coupling acts as a potential barrier and results in a finite coercive field as sketched in Figure 7.6(b). We also expect that the hysteresis loop will be deformed from an ideal square shape because of the domain formation and incoherent spin flop at the interface.

7.3 Conclusions

In summary, we have studied the magnetoelectric coupling in the model system of multiferroic BFO and FM LSMO, and demonstrated in which the electric-field control of magnetization, in-plane magnetic anisotropy and exchange-bias anisotropy. Using a combination of first-principles calculations and phenomenological models, we conclude that the magnetoelectric coupling arise from the strong interplay and reconstruction between charge, spin, orbital and lattice degrees of freedom driven by a ferroelectric switching. Moreover, the change of ground state of the interface magnetic coupling may provide a novel approach to deterministic and permanent control of the magnetism with electric field, which illustrates one possible pathway to achieve new spintronics based memory, logic and sensing devices.

Chapter 8

Conclusions and future prospects

Novel phenomena and functionalities at epitaxial complex oxide heterostructures have been attracting much scientific attention from fundamental physics as well as technological applications. Essentially, the charge and spin reconstructions at the interface could lead to exotic, totally unexpected state of matters at the interface, such as conductive interface between insulating materials and interfacial ferromagnetism at the proximity of antiferromagnet. In this dissertation, we present a systematic study of the electronic (charge) and magnetic (spin) interactions in an all-oxide model heterostructure system consisting of multiferroic (ferroelectric (FE) and antiferromagnetic (AFM)) $BiFeO_3$(BFO) and ferromagnet (FM) $La_{0.7}Sr_{0.3}MnO_3$ (LSMO). High-quality BFO/LSMO heterostructures were synthesized using reflection high-energy electron diffraction (RHEED) assisted pulsed-laser deposition (PLD). Various characterizations have shown that an atomically smooth and well-controlled epitaxial interface indeed can be fabricated, thus providing a solid platform for the subsequent investigation of reconstruction and interplay between charge and spin degrees of freedom at the interface.

We first investigate the electronic interaction at BFO/LSMO heterointerfaces. We note that an interface dipole state is formed at the interface, as a consequence of the valence mismatch between these two materials, and the sign of which depends on the interfacial atomic stacking sequence. Using piezoresponse force microscopy (PFM), we measured the ferroelectric polarization states in the BFO layer, which demonstrates a novel consequence of the interface valence mismatch, namely that the ferroelectric polarization direction in the BFO layer is strongly correlated with the interface stacking sequence. In addition, subsequent piezoresponse hysteresis loops measurements reveal that an electrostatic potential step is formed at the interface, and responsible for this macroscopic ferroelectric control. It is worth noting that the tuning and manipulating of the interface electronic structure as presented in this dissertation is of fundamental importance for the applications of ferroelectric device, such as field-effect transistors, ferroelectric tunnel junctions and photon diode, since those effects are strongly correlated with the interface electronic structures.

Another interesting aspect of the study is related to the magnetic coupling and spin reconstruction across the interface. At the interface of BFO/LSMO heterostructures, we demonstrate the existence of a strong magnetic coupling, manifested in the form of an enhanced coercive field as well as an exchange-bias field. Systematic temperature dependence study indicates that this magnetic coupling is likely due to spin frustrations at the interface. This speculation is supported by x-ray magnetic circular dichroism on a reversed LSMO/BFO heterostructure, which reveals a novel ferromagnetic state formed in the antiferromagnetic BFO sublattice at the interface with LSMO due to the spin frustration. Moreover, our results demonstrate that the magnetic state is directly related with an electronic orbital reconstruction at the interface, which is supported by the polarization-dependence of x-ray absorption measurement at oxygen $K-$edge. Inspired by this finding, we achieved successfully the electrical control of the magnetic coupling using a field effect device, using multiferroic BFO as the ferroelectric gate and ferromagnet LSMO as the conducting channel. Magnetotransport measurements clearly demonstrated a reversible switch/control of exchange-bias coupling between two distinct states correlated with the FE polarization of BFO. With both first-principle calculations and phenomenological models, we propose that this interesting magnetoelectric coupling is correlated with an electric-field control of both the orbital degree of freedom at LSMO layer and atomic structure across BFO/LSMO interface.

In summary, BFO/LSMO heterointerfaces present an intriguing model system to study the interaction of charge and spin degrees of freedom at heterointerfaces. In additional, the ferroelectric nature of multiferroic BFO provides a pathway to manipulate these couplings with electric field as a perturbation, so as to obtain the magnetoelectric coupling. Clearly, such coupling is not limited to only these two degrees of freedom. The coupling and reconstruction of other degrees of freedom, e.g. orbital and lattice, and their implication to the magnetic and electronic properties of heterostructures will definitely bring in amazing physical concepts to this developing field of complex oxide heterointerfaces. Furthermore, other external perturbations, such as light, magnetic field and strain could also be employed to manipulate interface phenomena to achieve novel functionalities.

Bibliography

[1] Kroemer, H. Nobel Lecture: Quasielectric fields and band offsets: teaching electrons new tricks. *Rev. Mod. Phys.* **73**, 783 (2001).

[2] Bednorz, J. G. & Muller, K. A. Possible high-T_c superconductivity in the Ba-La-Cu-O system. *Zeitschrift Fur Physik B-Condensed Matter* **64**, 189 (1986).

[3] Imada, M., Fujimori, A. & Tokura, Y. Metal-insulator transitions. *Rev. Mod. Phys.* **70**, 1039 (1998).

[4] Jin, S. *et al.* Thousandfold change in resistivity in magnetoresistive La-Ca-Mn-O Films. *Science* **264**, 413 (1994).

[5] Ramirez, A. P. Colossal magnetoresistance. *J. Phys.-Condes. Matter* **9**, 8171 (1997).

[6] Ohtomo, A., Muller, D. A., Grazul, J. L. & Hwang, H. Y. Artificial charge-modulation in atomic-scale perovskite titanate superlattices. *Nature* **419**, 378 (2002).

[7] Ohtomo, A. & Hwang, H. Y. A high mobility electron gas at the $LaAlO_3/SrTiO_3$ heterointerface. *Nature* **427**, 423 (2004).

[8] Lee, H. N., Christen, H. M., Chisholm, M. F., Rouleau, C. M. & Lowndes, D. H. Strong polarization enhancement in asymmetric three-component ferroelectric superlattices. *Nature* **433**, 395 (2005).

[9] Rijnders, G. & Blank, D. H. A. Materials science - Build your own superlattice. *Nature* **433**, 369 (2005).

[10] Tsukazaki, A. *et al.* Quantum Hall effect in polar oxide heterostructures. *Science* **315**, 1388 (2007).

[11] Ramirez, A. P. Oxide electronics emerge. *Science* **315**, 1377 (2007).

[12] Dagotto, E. Physics - When oxides meet face to face. *Science* **318**, 1076 (2007).

[13] Heber, J. Materials science: Enter the oxides. *Nature* **459**, 28 (2009).

[14] Zubko, P., Gariglio, S., Gabay, M., Ghosez, P. & Triscone, J. M. Interface physics in complex oxide heterostructures. *Annu. Rev. Condens. Matter Phys.* **2**, 141 (2011).

[15] Ueda, K., Tabata, H. & Kawai, T. Ferromagnetism in $LaFeO_3$-$LaCrO_3$ superlattices. *Science* **280**, 1064 (1998).

[16] Chakhalian, J. *et al.* Magnetism at the interface between ferromagnetic and superconducting oxides. *Nat. Phys.* **2**, 244 (2006).

[17] Ramesh, R. & Spaldin, N. A. Multiferroics: progress and prospects in thin films. *Nat. Mater.* **6**, 21 (2007).

[18] Spaldin, N. A., Cheong, S. W. & Ramesh, R. Multiferroics: past, present, and future. *Phys. Today* **63**, 38 (2010).

[19] Ramanathan, S. *Thin film metal-oxides* (Springer, 2010).

[20] Medarde, M. L. Structural, magnetic and electronic properties of $RNiO_3$ perovskites (R equals rare earth). *J. Phys.-Condes. Matter* **9**, 1679 (1997).

[21] Asai, K. *et al.* Neutron-scattering study of the spin-state transition and magnetic correlations in $La_{1-x}Sr_xCoO_3$ (x=0 and 0.08). *Phys. Rev. B* **50**, 3025 (1994).

[22] Yamaguchi, S., Okimoto, Y., Taniguchi, H. & Tokura, Y. Spin-state transition and high-spin polarons in $LaCoO_3$. *Phys. Rev. B* **53**, R2926 (1996).

[23] Kramers, H. A. Interaction of magnetogenic atoms in paramagnetic crystals. *Physica* **1**, 182 (1934).

[24] Anderson, P. W. Antiferromagnetism-theory of superexchange interaction. *Phys. Rev.* **79**, 350 (1950).

[25] Goodenough, J. B. Theory of the role of covalence in the perovskite-type manganites [La,M(II)]MnO_3. *Phys. Rev.* **100**, 564 (1955).

[26] Goodenough, J. B. An interpretation of the magnetic properties of the perovskite-type mixed crystals $La_{1-x}Sr_xCoO_{3-Lambda}$. *J. Phys. Chem. Solids* **6**, 287 (1958).

[27] Kanamori, J. Superexchange interaction and symmetry properties of electron orbitals. *J. Phys. Chem. Solids* **10**, 87 (1959).

[28] Zener, C. Interaction between the D-shells in the transtion metals. II. Ferromagnetic compounds of manganese with perovskite structure. *Phys. Rev.* **82**, 403 (1951).

[29] Dzyaloshinskii, I. A thermodynamical, theory of "weak" ferromagnetism in antiferromagnetics. *Sov. Phys. JETP* **5**, 1259 (1957).

[30] Dzyaloshinskii, I. The probelm of piezomagnetism. *Sov. Phys. JETP* **6**, 621 (1958).

[31] Moriya, T. Anisotropic superexchange interaction and weak ferromagnetism. *Phys. Rev.* **120**, 91 (1960).

[32] Kane, C. L. & Mele, E. J. Quantum spin Hall effect in graphene. *Phys. Rev. Lett.* **95**, 226801 (2005).

[33] Lanzara, A. *et al.* Evidence for ubiquitous strong electron-phonon coupling in high-temperature superconductors. *Nature* **412**, 510 (2001).

[34] Sergienko, I. A. & Dagotto, E. Role of the Dzyaloshinskii-Moriya interaction in multiferroic perovskites. *Phys. Rev. B* **73**, 094434 (2006).

[35] Nakagawa, N., Hwang, H. Y. & Muller, D. A. Why some interfaces cannot be sharp. *Nat. Mater.* **5**, 204 (2006).

[36] Harrison, W. A., Kraut, E. A., Waldrop, J. R. & Grant, R. W. Polar Heterojunction in inerfaces. *Phys. Rev. B* **18**, 4402 (1978).

[37] Huijben, M. *et al.* Structure-Property Relation of $SrTiO_3/LaAlO_3$ Interfaces. *Adv. Mater.* **21**, 1665–1677 (2009).

[38] Rijnders, G. & Blank, D. H. A. Perovskite oxides - An atomic force pencil and eraser. *Nat. Mater.* **7**, 270 (2008).

[39] Basletic, M. *et al.* Mapping the spatial distribution of charge carriers in $LaAlO_3/SrTiO_3$ heterostructures. *Nat. Mater.* **7**, 621 (2008).

[40] Brinkman, A. *et al.* Magnetic effects at the interface between non-magnetic oxides. *Nat. Mater.* **6**, 493 (2007).

[41] Reyren, N. *et al.* Superconducting interfaces between insulating oxides. *Science* **317**, 1196 (2007).

[42] Goss Levi, B. Interface between nonmagnetic insulators may be ferromagnetic and conducting. *Phys. Today* **60**, 23 (2007).

[43] Schooley, J. F., Hosler, W. R. & Cohen, M. L. Superconductivity in semiconducting $SrTiO_3$. *Phys. Rev. Lett.* **12**, 474 (1964).

[44] Caviglia, A. D. *et al.* Electric field control of the $LaAlO_3/SrTiO_3$ interface ground state. *Nature* **456**, 624 (2008).

[45] Chen, H., Kolpak, A. M. & Ismail-Beigi, S. Electronic and Magnetic Properties of $SrTiO_3/LaAlO_3$ Interfaces from First Principles. *Adv. Mater.* **22**, 2881 (2010).

[46] Cen, C., Thiel, S., Mannhart, J. & Levy, J. Oxide nanoelectronics on demand. *Science* **323**, 1026 (2009).

[47] Irvin, P. *et al.* Rewritable nanoscale oxide photodetector. *Nat. Photonics* **4**, 849 (2010).

[48] Yajima, T., Hikita, Y. & Hwang, H. Y. A heteroepitaxial perovskite metal-base transistor. *Nat. Mater.* **10**, 198 (2011).

[49] Meijer, G. I. Ferromagnetic superlattices. *Science* **281**, 1571 (1998).

[50] Gray, B., Lee, H. N., Liu, J., Chakhalian, J. & Freeland, J. W. Local electronic and magnetic studies of an artificial La_2FeCrO_6 double perovskite. *Appl. Phys. Lett.* **97**, 013105 (2010).

[51] Baettig, P., Ederer, C. & Spaldin, N. A. First principles study of the multiferroics $BiFeO_3$, Bi_2FeCrO_6, and $BiCrO_3$: Structure, polarization, and magnetic ordering temperature. *Phys. Rev. B* **72**, 214105 (2005).

[52] Ichikawa, N. *et al.* Multiferroism at room temperature in $BiFeO_3/BiCrO_3(111)$ artificial superlattices. *Appl. Phys. Express* **1**, 101302 (2008).

[53] Chakhalian, J. *et al.* Orbital reconstruction and covalent bonding at an oxide interface. *Science* **318**, 1114 (2007).

[54] Arenholz, E. *et al.* Magnetic structure of $La_{0.7}Sr_{0.3}MnO_3/La_{0.7}Sr_{0.3}FeO_3$ superlattices. *Appl. Phys. Lett.* **94**, 072503 (2009).

[55] Ueda, K., Tabata, H. & Kawai, T. Control of magnetic properties in $LaCrO_3$-$LaFeO_3$ artificial superlattices. *J. Appl. Phys.* **89**, 2847 (2001).

[56] Yamada, H. *et al.* Engineered interface of magnetic oxides. *Science* **305**, 646 (2004).

[57] Fiebig, M. Revival of the magnetoelectric effect. *J. Phys. D-Appl. Phys.* **38**, R123 (2005).

[58] Khomskii, D. I. Multiferroics: Different ways to combine magnetism and ferroelectricity. *J. Magn. Magn. Mater.* **306**, 1 (2006).

[59] Eerenstein, W., Mathur, N. D. & Scott, J. F. Multiferroic and magnetoelectric materials. *Nature* **442**, 759 (2006).

[60] Cheong, S. W. & Mostovoy, M. Multiferroics: a magnetic twist for ferroelectricity. *Nat. Mater.* **6**, 13 (2007).

[61] Martin, L. W. *et al.* Multiferroics and magnetoelectrics: thin films and nanostructures. *J. Phys.-Condes. Matter* **20**, 434220 (2008).

[62] Bea, H., Gajek, M., Bibes, M. & Barthelemy, A. Spintronics with multiferroics. *J. Phys.-Condes. Matter* **20**, 434221 (2008).

[63] Khomskii, D. Classifying multiferroics: Mechanisms and effects. *Physics* **2**, 20 (2009).

[64] Wang, K. F., Liu, J. M. & Ren, Z. F. Multiferroicity: the coupling between magnetic and polarization orders. *Adv. Phys.* **58**, 321 (2009).

[65] Tokura, Y. & Seki, S. Multiferroics with spiral spin orders. *Adv. Mater.* **22**, 1554 (2010).

[66] Hill, N. A. Why are there so few magnetic ferroelectrics? *J. Phys. Chem. B* **104**, 6694 (2000).

[67] Seshadri, R. & Hill, N. A. Visualizing the role of Bi 6s "Lone pairs" in the off-center distortion in ferromagnetic $BiMnO_3$. *Chem. Mat.* **13**, 2892 (2001).

[68] Kimura, T. *et al.* Magnetocapacitance effect in multiferroic $BiMnO_3$. *Phys. Rev. B* **67**, 180401 (2003).

[69] Son, J. Y., Kim, B. G., Kim, C. H. & Cho, J. H. Writing polarization bits on the multiferroic $BiMnO_3$ thin film using Kelvin probe force microscope. *Appl. Phys. Lett.* **84**, 4971 (2004).

[70] Yang, C. H. *et al.* Resonant x-ray scattering study on multiferroic $BiMnO_3$. *Phys. Rev. B* **73**, 224112 (2006).

[71] Gajek, M. *et al.* Tunnel junctions with multiferroic barriers. *Nat. Mater.* **6**, 296 (2007).

[72] Zhao, T. *et al.* Electrical control of antiferromagnetic domains in multiferroic $BiFeO_3$ films at room temperature. *Nat. Mater.* **5**, 823 (2006).

[73] Lebeugle, D. *et al.* Electric-field-induced spin flop in $BiFeO_3$ single crystals at room temperature. *Phys. Rev. Lett.* **100**, 227602 (2008).

[74] Chu, Y. H. *et al.* Electric-field control of local ferromagnetism using a magnetoelectric multiferroic. *Nat. Mater.* **7**, 478–482 (2008).

[75] Katsufuji, T. *et al.* Dielectric and magnetic anomalies and spin frustration in hexagonal $RMnO_3$ (R=Y, Yb, and Lu). *Phys. Rev. B* **64**, 104419 (2001).

[76] Van Aken, B. B., Palstra, T. T. M., Filippetti, A. & Spaldin, N. A. The origin of ferroelectricity in magnetoelectric $YMnO_3$. *Nat. Mater.* **3**, 164 (2004).

[77] Fennie, C. J. & Rabe, K. M. Ferroelectric transition in $YMnO_3$ from first principles. *Phys. Rev. B* **72**, 100103 (2005).

[78] Efremov, D. V., Van den Brink, J. & Khomskii, D. I. Bond-versus site-centred ordering and possible ferroelectricity in manganites. *Nat. Mater.* **3**, 853 (2004).

[79] Tokunaga, Y. *et al.* Rotation of orbital stripes and the consequent charge-polarized state in bilayer manganites. *Nat. Mater.* **5**, 937 (2006).

[80] Ikeda, N. *et al.* Ferroelectricity from iron valence ordering in the charge-frustrated system $LuFe_2O_4$. *Nature* **436**, 1136 (2005).

[81] Kimura, T. *et al.* Magnetic control of ferroelectric polarization. *Nature* **426**, 55 (2003).

[82] Hur, N. *et al.* Electric polarization reversal and memory in a multiferroic material induced by magnetic fields. *Nature* **429**, 392 (2004).

[83] Fennie, C. J. & Rabe, K. M. Magnetic and electric phase control in epitaxial $EuTiO_3$ from first principles. *Phys. Rev. Lett.* **97**, 267602 (2006).

[84] Lee, J. H. *et al.* A strong ferroelectric ferromagnet created by means of spin-lattice coupling. *Nature* **466**, 954 (2010).

[85] Bibes, M. & Barthelemy, A. Multiferroics: Towards a magnetoelectric memory. *Nat. Mater.* **7**, 425 (2008).

[86] Rondinelli, J. M., Stengel, M. & Spaldin, N. A. Carrier-mediated magnetoelectricity in complex oxide heterostructures. *Nat. Nanotechnol.* **3**, 46 (2008).

[87] Burton, J. D. & Tsymbal, E. Y. Prediction of electrically induced magnetic reconstruction at the manganite/ferroelectric interface. *Phys. Rev. B* **80**, 174406 (2009).

[88] Molegraaf, H. J. A. *et al.* Magnetoelectric Effects in Complex Oxides with Competing Ground States. *Adv. Mater.* **21**, 3470 (2009).

[89] Vaz, C. A. F. *et al.* Origin of the magnetoelectric coupling effect in $PbZr_{0.2}Ti_{0.8}O_3/La_{0.8}Sr_{0.2}MnO_3$ multiferroic heterostructures. *Phys. Rev. Lett.* **104**, 127202 (2010).

[90] Garcia, V. *et al.* Ferroelectric Control of Spin Polarization. *Science* **327**, 1106 (2010).

[91] Eerenstein, W., Wiora, M., Prieto, J. L., Scott, J. F. & Mathur, N. D. Giant sharp and persistent converse magnetoelectric effects in multiferroic epitaxial heterostructures. *Nat. Mater.* **6**, 348 (2007).

[92] Wang, J. *et al.* Large electric-field modulation of magnetic properties in Fe films on $BiScO_3$-$PbTiO_3$ ceramics. *J. Nanomater.* **2010**, 142750 (2010).

[93] Ma, J., Hu, J., Li, Z. & Nan, C. W. Recent progress in multiferroic magnetoelectric composites: from bulk to thin films. *Adv. Mater.* **23**, 1062 (2011).

[94] Laukhin, V. *et al.* Electric-field control of exchange bias in multiferroic epitaxial heterostructures. *Phys. Rev. Lett.* **97**, 227201 (2006).

[95] Borisov, P., Hochstrat, A., Chen, X., Kleemann, W. & Binek, C. Magnetoelectric switching of exchange bias. *Phys. Rev. Lett.* **94**, 117203 (2005).

[96] Nogues, J. & Schuller, I. K. Exchange bias. *J. Magn. Magn. Mater.* **192**, 203 (1999).

[97] He, X. *et al.* Robust isothermal electric control of exchange bias at room temperature. *Nat. Mater.* **9**, 579 (2010).

[98] Royen, P. & Swars, K. Das System Wismutoxyd-Eisenoxyd Im Bereich Von 0 Bis 55 Mol-Percent Eisenoxyd. *Angew. Chem.-Int. Edit.* **69**, 779 (1957).

[99] Michel, C., Moreau, J. M., Achenbac, G. D., Gerson, R. & James, W. J. Atomic structure of $BiFeO_3$. *Solid State Commun.* **7**, 701 (1969).

[100] Fischer, P., Polomska, M., Sosnowsa, I. & Szymanski, M. Temperature-dependence of the crystal and magnetic-structures of $BiFeO_3$. *J. Phys. D-Solid State Phys.* **13**, 1931 (1980).

[101] Sosnowsa, I., Peterlinneumaier, T. & Steichele, E. Spiral magnetic-ordering in Bismuth Ferrite. *J. Phys. C-Solid Stat. Phys.* **15**, 4835 (1982).

[102] Teague, J. R., Gerson, R. & James, W. J. Dielectric hysteresis in single crystal $BiFeO_3$. *Solid State Commun.* **8**, 1073 (1970).

[103] Tabares-Munoz, C., Rivera, J.-P., Bezinges, A., Monnier, A. & Schmid, H. Measurement of the quadratic magnetoelectric effect on single crystalline $BiFeO_3$. In *Jap. J. Appl. Phys. Suppl.*, vol. 24, 1051 (Japan, 1985).

[104] Wang, J. *et al.* Epitaxial $BiFeO_3$ multiferroic thin film heterostructures. *Science* **299**, 1719 (2003).

[105] Lebeugle, D. *et al.* Room-temperature coexistence of large electric polarization and magnetic order in $BiFeO_3$ single crystals. *Phys. Rev. B* **76**, 24116 (2007).

[106] Lebeugle, D., Colson, D., Forget, A. & Viret, M. Very large spontaneous electric polarization in $BiFeO_3$ single crystals at room temperature and its evolution under cycling fields. *Appl. Phys. Lett.* **91**, 022907 (2007).

[107] Eerenstein, W. *et al.* Comment on "Epitaxial $BiFeO_3$ multiferroic thin film heterostructures". *Science* **307**, 1203 (2005).

[108] Wang, J. *et al.* Response to comment on "Epitaxial $BiFeO_3$ multiferroic thin film heterostructures". *Science* **307**, 1203 (2005).

[109] Choi, T., Lee, S., Choi, Y. J., Kiryukhin, V. & Cheong, S. W. Switchable ferroelectric diode and photovoltaic effect in $BiFeO_3$. *Science* **324**, 63 (2009).

[110] Yang, S. Y. *et al.* Above-bandgap voltages from ferroelectric photovoltaic devices. *Nat. Nanotechnol.* **5**, 143 (2010).

[111] Zeches, R. J. *et al.* A strain-driven morphotropic phase boundary in $BiFeO_3$. *Science* **326**, 977 (2009).

[112] Kundys, B., Viret, M., Colson, D. & Kundys, D. O. Light- induced size changes in $BiFeO_3$ crystals. *Nat. Mater.* **9**, 803 (2010).

[113] Jonker, G. H. & VanSanten, J. H. Ferromagnetic compounds of manganese with perovskite structure. *Physica* **16**, 337 (1950).

[114] Dagotto, E. *Nanoscale Phase Separation and Colossal Magnetoresistance* (Springer, 2003).

[115] Fujishiro, H., Fukase, T. & Ikebe, M. Charge ordering and sound velocity anomaly in $La_{1-x}Sr_xMnO_3$ ($X \geq 0.5$). *J. Phys. Soc. Jpn.* **67**, 2582 (1998).

[116] Douglas, B. C. & Graham, K. H. (eds.) *Pulsed laser deposition of thin films* (John Wiley and Sons, 1994).

[117] Ohring, M. *Materials science of thin films: depostion and structure* (Academic Press: San Francisco, 2002).

[118] Ichimiya, A. & Cohen, P. I. (eds.) *Reflection high energy electron diffraction* (Cambridge University Press, 2004).

[119] Kawasaki, M. *et al.* Atomic control of the $SrTiO_3$ crystal-surface. *Science* **266**, 1540 (1994).

[120] Kim, D. H., Lee, H. N., Biegalski, M. D. & Christen, H. M. Effect of epitaxial strain on ferroelectric polarization in multiferroic $BiFeO_3$ films. *Appl. Phys. Lett.* **92**, 012911 (2008).

[121] Huijben, M. *et al.* Critical thickness and orbital ordering in ultrathin $La_{0.7}Sr_{0.3}MnO_3$ films. *Phys. Rev. B* **78**, 094413 (2008).

[122] Sun, J. Z., Abraham, D. W., Rao, R. A. & Eom, C. B. Thickness-dependent magnetotransport in ultrathin manganite films. *Appl. Phys. Lett.* **74**, 3017 (1999).

[123] Zavaliche, F. *et al.* Multiferroic $BiFeO_3$ films: domain structure and polarization dynamics. *Phase Transit.* **79**, 991 (2006).

[124] Chu, Y.-H. *et al.* Domain control in mulfiferroic $BiFeO_3$ through substrate vicinality. *Adv. Mater.* **19**, 2662 (2007).

[125] Neaton, J. B., Ederer, C., Waghmare, U. V., Spaldin, N. A. & Rabe, K. M. First-principles study of spontaneous polarization in multiferroic $BiFeO_3$. *Phys. Rev. B* **71**, 014113 (2005).

[126] Pabst, G. W., Martin, L. W., Chu, Y. H. & Ramesh, R. Leakage mechanisms in $BiFeO_3$ thin films. *Appl. Phys. Lett.* **90**, 072902 (2007).

[127] Yu, P. *et al.* Interface control of bulk ferroelectric polarization. *Submitted* (2010).

[128] Mannhart, J. & Schlom, D. G. Oxide Interfaces-An opportunity for electronics. *Science* **327**, 1607 (2010).

[129] Okamoto, S. & Millis, A. J. Electronic reconstruction at an interface between a Mott insulator and a band insulator. *Nature* **428**, 630 (2004).

[130] Benckiser, E. *et al.* Orbital reflectometry of oxide heterostructures. *Nat. Mater.* **10**, 189 (2011).

[131] Rijnders, G., Blank, D. H. A., Choi, J. & Eom, C. B. Enhanced surface diffusion through termination conversion during epitaxial $SrRuO_3$ growth. *Appl. Phys. Lett.* **84**, 505 (2004).

[132] Rabalais, J. W. *Principles and applications of ion scattering spectroscopy* (John Wiley and Sons, 2003).

[133] Kleibeuker, J. E. *et al.* Atomically defined rare-earth scandate crystal surfaces. *Adv. Funct. Mater.* **20**, 3490 (2010).

[134] Biswas, A. *et al.* Universal Ti-rich termination of atomically flat $SrTiO_3$ (001), (110), and (111) surfaces. *Appl. Phys. Lett.* **98**, 051904 (2011).

[135] Erni, R., Rossell, M. D., Kisielowski, C. & Dahmen, U. Atomic-resolution imaging with a Sub-50-pm electron probe. *Phys. Rev. Lett.* **102**, 096101 (2009).

[136] Kresse, G. & Furthmuller, J. Efficient iterative schemes for ab initio total-energy calculations using a plane-wave basis set. *Phys. Rev. B* **54**, 11169 (1996).

[137] Peressi, M., Binggeli, N. & Baldereschi, A. Band engineering at interfaces: theory and numerical experiments. *J. Phys. D-Appl. Phys.* **31**, 1273 (1998).

[138] Hikita, Y., Nishikawa, M., Yajima, T. & Hwang, H. Y. Termination control of the interface dipole in $La_{0.7}Sr_{0.3}MnO_3$/Nb:$SrTiO_3$ (001) Schottky junctions. *Phys. Rev. B* **79**, 073101 (2009).

[139] Burton, J. D. & Tsymbal, E. Y. Evolution of the band alignment at polar oxide interfaces. *Phys. Rev. B* **82**, 161407 (2010).

[140] Scott, J. F. *Ferroelectric memories* (Springer, 2000).

[141] Zheng, B. & Binggeli, N. Influence of the interface atomic structure on the magnetic and electronic properties of $La_{2/3}Sr_{1/3}MnO_3$/$SrTiO_3$ (001) heterojunctions. *Phys. Rev. B* **82**, 245311 (2010).

[142] Chisholm, M. F., Luo, W. D., Oxley, M. P., Pantelides, S. T. & Lee, H. N. Atomic-Scale Compensation Phenomena at Polar Interfaces. *Phys. Rev. Lett.* **105**, 197602 (2010).

[143] Wang, L. M., Liu, C. C., Yang, H. C. & Horng, H. E. Room-temperature tunneling magnetoresistance in $La_{0.7}Sr_{0.3}MnO_3$ step-edge junctions. *J. Appl. Phys.* **95**, 4928 (2004).

[144] Glinchuk, M. D., Zaulychny, V. Y. & Stephanovich, V. A. Effect of electrodes on the properties of a thin ferroelectric film. *Phys. Solid State* **50**, 472 (2008).

[145] Okamoto, J. *et al.* Correlation effects in the electronic structure of $SrRuO_3$. *Phys. Rev. B* **60**, 2281 (1999).

[146] Siemons, W. *et al.* Dependence of the electronic structure of $SrRuO_3$ and its degree of correlation on cation off-stoichiometry. *Phys. Rev. B* **76**, 075126 (2007).

[147] Li, H. C., Si, W. D., West, A. D. & Xi, X. X. Thickness dependence of dielectric loss in $SrTiO_3$ thin films. *Appl. Phys. Lett.* **73**, 464 (1998).

[148] Qiu, J., Lu, H. B., Jin, K. J., He, M. & Xing, J. Manganite-layer thickness-dependent photovoltaic effect of $La_{0.9}Sr_{0.1}MnO_3//SrNb_{0.01}Ti_{0.99}O_3$ i p-n heterojunction. *Physica B* **400**, 66 (2007).

[149] Ohta, S., Nomura, T., Ohta, H. & Koumoto, K. High-temperature carrier transport and thermoelectric properties of heavily La- or Nb-doped $SrTiO_3$ single crystals. *J. Appl. Phys.* **97**, 034106 (2005).

[150] Meiklejohn, W. H. & Bean, C. P. New magnetic anisotropy. *Phys. Rev.* **102**, 1413 (1956).

[151] Berkowitz, A. E. & Takano, K. Exchange anisotropy - a review. *J. Magn. Magn. Mater.* **200**, 552 (1999).

[152] Kiwi, M. Exchange bias theory. *J. Magn. Magn. Mater.* **234**, 584 (2001).

[153] Nogues, J. *et al.* Exchange bias in nanostructures. *Phys. Rep.-Rev. Sec. Phys. Lett.* **422**, 65 (2005).

[154] Kools, J. C. S. Exchange-biased spin-valves for magnetic storage. *IEEE Trans. Magn.* **32**, 3165 (1996).

[155] Parkin, S. S. P. *et al.* Exchange-biased magnetic tunnel junctions and application to nonvolatile magnetic random access memory (invited). *J. Appl. Phys.* **85**, 5828 (1999).

[156] Martin, L. W., Chu, Y.-H. & Ramesh, R. Advances in the growth and characterization of magnetic, ferroelectric, and multiferroic oxide thin films. *Mater. Sci. Eng. R-Rep.* **68**, III (2010).

[157] Meiklejohn, W. H. & Bean, C. P. New magnetic anisotropy. *Phys. Rev.* **105**, 904 (1957).

[158] Meiklejohn, W. H. Exchange anisotropy - a review. *J. Appl. Phys.* **33**, 1328 (1962).

[159] Kurti, N. (ed.) *Selected works of Louis Neel* (Gordon Breach, New York, 1988).

[160] Malozemoff, A. P. Random-field model of exchange anisotropy at rough ferromagnetic-antiferromagnetic interfaces. *Phys. Rev. B* **35**, 3679 (1987).

[161] Malozemoff, A. P. Heisenberg-to-Ising crossover in a random-field model with uniaxial anisotropy. *Phys. Rev. B* **37**, 7673 (1988).

[162] Malozemoff, A. P. Mechanisms of exchange-anisotropy. *J. Appl. Phys.* **63**, 3874 (1988).

[163] Mauri, D., Siegmann, H. C., Bagus, P. S. & Kay, E. Simple-model for thin ferromagnetic-films exchange coupled to an antiferromagnetic substrate. *J. Appl. Phys.* **62**, 3047 (1987).

[164] Ohldag, H. *et al.* Correlation between exchange bias and pinned interfacial spins. *Phys. Rev. Lett.* **91**, 017203 (2003).

[165] Roy, S. *et al.* Depth profile of uncompensated spins in an exchange bias system. *Phys. Rev. Lett.* **95**, 047201 (2005).

[166] Bruck, S., Schu uml tz, G., Goering, E., Ji, X. S. & Krishnan, K. Uncompensated moments in the MnPd/Fe exchange bias system. *Phys. Rev. Lett.* **101**, 126402 (2008).

[167] Wu, J. *et al.* Direct measurement of rotatable and frozen CoO spins in exchange bias system of CoO/Fe/Ag(001). *Phys. Rev. Lett.* **104**, 217204 (2010).

[168] Koon, N. C. Calculations of exchange bias in thin films with ferromagnetic/antiferromagnetic interfaces. *Phys. Rev. Lett.* **78**, 4865 (1997).

[169] Schulthess, T. C. & Butler, W. H. Consequences of spin-flop coupling in exchange biased films. *Phys. Rev. Lett.* **81**, 4516 (1998).

[170] Schulthess, T. C. & Butler, W. H. Coupling mechanisms in exchange biased films (invited). *J. Appl. Phys.* **85**, 5510 (1999).

[171] Dimitrov, D. V., Zhang, S. F., Xiao, J. Q., Hadjipanayis, G. C. & Prados, C. Effect of exchange interactions at antiferromagnetic/ferromagnetic interfaces on exchange bias and coercivity. *Phys. Rev. B* **58**, 12090 (1998).

[172] Korenivski, V. *et al.* Interlayer exchange coupling in amorphous/crystalline $NiFe_2O_4$ thin-film bilayers. *J. Appl. Phys.* **79**, 5926 (1996).

[173] Fiorani, D., Del Bianco, L., Testa, A. M. & Trohidou, K. N. Exchange bias in disordered granular systems. *J. Phys.-Condes. Matter* **19**, 225007 (2007).

[174] Ambrose, T. & Chien, C. L. Dependence of exchange coupling on antiferromagnetic layer thickness in NiFe/CoO bilayers. *J. Appl. Phys.* **83**, 6822 (1998).

[175] Bea, H. *et al.* Mechanisms of exchange bias with multiferroic $BiFeO_3$ epitaxial thin films. *Phys. Rev. Lett.* **100**, 017204 (2008).

[176] Martin, L. W. *et al.* Nanoscale control of exchange bias with $BiFeO_3$ thin films. *Nano Lett.* **8**, 2050 (2008).

[177] Yu, P. *et al.* Interface ferromagnetism and orbital reconstruction in $BiFeO_3$-$La_{0.7}Sr_{0.3}MnO_3$ heterostructures. *Phys. Rev. Lett.* **105**, 027201 (2010).

[178] Ohldag, H. *et al.* Spectroscopic identification and direct imaging of interfacial magnetic spins. *Phys. Rev. Lett.* **87**, 247201 (2001).

[179] Stohr, J. Exploring the microscopic origin of magnetic anisotropies with X-ray magnetic circular dichroism (XMCD) spectroscopy. *J. Magn. Magn. Mater.* **200**, 470 (1999).

[180] Yang, C. H. *et al.* Electric modulation of conduction in multiferroic Ca-doped $BiFeO_3$ films. *Nat. Mater.* **8**, 485 (2009).

[181] Kavich, J. J. *et al.* Nanoscale suppression of magnetization at atomically assembled manganite interfaces: XMCD and XRMS measurements. *Phys. Rev. B* **76**, 14410 (2007).

[182] Ederer, C. & Spaldin, N. A. Weak ferromagnetism and magnetoelectric coupling in bismuth ferrite. *Phys. Rev. B* **71**, 60401 (2005).

[183] Bea, H. *et al.* Investigation on the origin of the magnetic moment of $BiFeO_3$ thin films by advanced X-ray characterizations. *Phys. Rev. B* **74**, 020101 (2006).

[184] Kim, J. Y., Koo, T. Y. & Park, J. H. Orbital and bonding anisotropy in a half-filled $GaFeO_3$ magnetoelectric ferrimagnet. *Phys. Rev. Lett.* **96**, 047205 (2006).

[185] Miltenyi, P. *et al.* Diluted antiferromagnets in exchange bias: Proof of the domain state model. *Phys. Rev. Lett.* **84**, 4224 (2000).

[186] Chen, C. T. *et al.* Experimental confirmation of the x-ray magnetic circular-dichroism sum rules for Iron and Cobalt. *Phys. Rev. Lett.* **75**, 152 (1995).

[187] Nakajima, R., Stohr, J. & Idzerda, Y. Electron-yield saturation effects in L-edge x-ray magnetic circular dichroism spectra of Fe, Co, and Ni. *Phys. Rev. B* **59**, 6421 (1999).

[188] Park, J. H. *et al.* Magnetic properties at surface boundary of a half-metallic ferromagnet $La_{0.7}Sr_{0.3}MnO_3$. *Phys. Rev. Lett.* **81**, 1953 (1998).

[189] Gota, S., Gautier-Soyer, M. & Sacchi, M. Fe 2p absorption in magnetic oxides: Quantifying angular-dependent saturation effects. *Phys. Rev. B* **62**, 4187 (2000).

[190] van der Laan, G., Arenholz, E., Chopdekar, R. & Suzuki, Y. Influence of crystal field on anisotropic x-ray magnetic linear dichroism at the Co^{2+} $L_{2,3}$ edges. *Phys. Rev. B* **77**, 064407 (2008).

[191] Haverkort, M. W. *et al.* Magnetic versus crystal-field linear dichroism in NiO thin films. *Phys. Rev. B* **69**, 020408 (2004).

[192] Tokura, Y. & Nagaosa, N. Orbital physics in transition-metal oxides. *Science* **288**, 462 (2000).

[193] Kawano-Furukawa, H. *et al.* Orbital order and a canted phase in the paramagnetic and ferromagnetic states of 50% hole-doped colossal magnetoresistance manganites. *Phys. Rev. B* **67**, 174422 (2003).

[194] Tokunaga, Y. *et al.* Composite domain walls in a multiferroic perovskite ferrite. *Nat. Mater.* **8**, 558 (2009).

[195] Wu, S. M. *et al.* Reversible electric control of exchange bias in a multiferroic field-effect device. *Nat. Mater.* **9**, 756 (2010).

[196] Ahn, C. H. *et al.* Ferroelectric field effect in ultrathin $SrRuO_3$ films. *Appl. Phys. Lett.* **70**, 206 (1997).

[197] Mathews, S., Ramesh, R., Venkatesan, T. & Benedetto, J. Ferroelectric field effect transistor based on epitaxial perovskite heterostructures. *Science* **276**, 238 (1997).

[198] Ahn, C. H. *et al.* Electrostatic modulation of superconductivity in ultrathin $GdBa_2Cu_3O_{7-x}$ films. *Science* **284**, 1152 (1999).

[199] Ahn, C. H. *et al.* Electrostatic modification of novel materials. *Rev. Mod. Phys.* **78**, 1185 (2006).

[200] Luo, W., Pennycook, S. J. & Pantelides, S. T. Magnetic "dead" layer at a complex oxide interface. *Phys. Rev. Lett.* **101**, 247204 (2008).

[201] Shaik, S. S. & Phillipe, C. H. *A chemist's guide to valence bond theory* (Wiley-Interscience, New Jersey, 2008).